Fatigue Fracture Mechanism and Damage Evaluation of Friction Stir Spot Welded AISI 1012 Cold Rolled-steel under Service Loading

(実働荷重下における AISI 1012冷間圧延鋼摩擦攪拌スポット継手の疲労破壊機構と損傷評価)

SEPTEMBER 2015

JOY-A-KA SUTEP
Department of Mechanical Science and Engineering,
Graduate School of Engineering,
Hiroshima University, JAPAN

ABSTRACT

The successful application of friction stir spot welding (FSSW) technology has attracted considerable attention from the automotive industry with energy consumption and operational cost are significantly lower than other welding methods. Previous research of FSSW has focused on mechanical properties, microstructure analysis, and how to produce a joint that optimizes the corresponding parameter sets. However, some stress concentration parts remain at the area welded by FSSW: a hollow called a keyhole caused by the tool shape, a discontinuity in shape called a lip, and a slit between the upper and lower sheet. Furthermore, the area welded by FSSW has several microstructures: the heat-affected zone, thermo-mechanically affected zone, and stir zone. It is highly advantageous to identify the relationship between the shape of the welded area unique to FSSW, the microstructure, and the fatigue crack behavior; however, details are not definitively known. Moreover, automobile loads randomly vary in service and very little is known about fatigue properties under random force amplitude conditions, which are assumed to occur in actual force situations.

Herein, fatigue tests were performed under constant force amplitudes to investigate the fatigue properties and fracture mechanism of FSSW-joined AISI 1012 cold rolled-steel sheet. Welded components are often subjected to variable force amplitudes, which call for fatigue life prediction methods that consider fatigue damage accumulation. Therefore, this study proposes and demonstrates the effectiveness of a method for evaluating cumulative fatigue damage under variable force amplitude conditions which are including repeat two-step and random force amplitude.

Fatigue tests were performed under constant force amplitude condition to investigate the fundamental fatigue properties and elucidation of fatigue fracture mechanism. The specimen used for this study had a fatigue limit of 0.1 kN. This value is very low compared with the maximum tensile force of the base metal and FSSW joint itself. The crack initiation occurred as a boundary between the welding interface zone and non-interface zone or slit tip regardless of amplitude level. In addition, the slit tip is located in the heat affected zones. The fatigue crack was found on the upper sheet at the distal slit through to the surface of sheet up to the concave zone. The fracture morphology is the mixed mode fracture. Therefore, fatigue fracture modes were independent on force amplitude level. Base on the 3-dimensional observation, the macroscopic fracture modes were independent on the force amplitude. The fatigue initiation life was dependent on the force amplitude. In other words, the fatigue crack initiation life under low force amplitude accounted for a comparatively large proportion of the entire fatigue life; whereas the fatigue cracks initiation life occurred in a relatively early stage under high force amplitude

An approach of fatigue damage evaluation method under repeated two-step force amplitudes was investigated based on the results under constant force amplitude. The FSSW joints used in this study show a deformation behavior specific to the thin plate structure. Therefore, the deformation behavior around the welded zone with the constant applied force amplitude was observed prior to the repeated two-step fatigue tests. The plastic deformation near the welded zone occurred under a force of 0.4–0.5 kN. Therefore, two cases were considered: in the first, macroscopic plastic deformation near the welded zone did not occur, and in the second, significant plastic deformation occurred. In fatigue tests with repeated two-step force amplitude, the fatigue limit of the welded joint disappeared. However, the fatigue damage evaluation using the modified Miner’s rule erred too much on the side of safety, as the modified Miner’s rule tends to overestimate the damage by applied forces below the fatigue limit. Thus, it was determined that, within the testing conditions used in this study, the fatigue damage evaluation using Haibach’s method yielded an accurate evaluation. In the case where significant plastic deformation caused by the applied force occurred near the welded zone, the cumulative fatigue damage value based on Miner’s rule was often larger than unity. Therefore, it is important to consider a cumulative damage estimation that takes into account the effect of pre-strain from the high force amplitude.

Also an approach of fatigue damage evaluation method under random force amplitudes was investigated based on the results under constant force amplitude. Two kinds of difference bandwidth force amplitude history generated using the stationary Gaussian random process, having narrow band and broad band frequency content. The various force ratios have no mean stress effect on the fatigue life of the welded joints. Therefore, it was possible to consider the cumulative damage by the rainflow counting method. The fatigue damage evaluation with the modified Miner’s rule tends to underestimate the damage by applied random wave form which was include the force below fatigue limit, which yields an evaluation approaching on the dangerous side. However, the modification of fatigue damage using Corten-Dolan’s method has been the results are satisfactory and the frequency ratio affects the evaluation of damage, and the frequency ratio to the suitable for consideration the fatigue damage is a few number of cycles below fatigue limit in a block of random force amplitude. By considering the cumulative fatigue damage evaluation base on Corten-Dolan’s method, it was possible to evaluate the fatigue life of the FSSW joints under random force amplitude conditions, which appropriated the strength designed range to considerable attention in the automotive industry.

TABLE OF CONTENTS

CHAPTER 1 Introduction

CHAPTER 2 Literature reviews

CHAPTER 3 Experimental methods

CHAPTER 4 3-Dimensional observation of the interior fatigue fracture mechanism on friction stir spot welded cross-tension specimen

CHAPTER 5 Fatigue damage evaluation of friction stir spot welded cross-tension joints under repeated two-step force amplitudes

CHAPTER 6 Fatigue damage evaluation of friction stir spot welded cross-tension joints under random force amplitude

LIST OF FIGURES

LIST OF TABLES

CHAPTER 1

Introduction

1.1 Introduction

In the 21st century and beyond, world-wide experts have agreed that propitiation of climate change is humanity's greatest threat and challenge. Coal, natural gas and oil fuel is about 86% of the world energy consumption in 2012 as showed in Fig. 1-1 [1]. With the global economy set to quadruple by mid-century, energy related carbon dioxide emission would be according to current trends, more than double putting the world into a potentially catastrophic trajectory that lead to temperature more than 5^{o}C warmer than in preindustrial time. Greenhouse gas emission and pollution progressive particularly from power plants generators are identified as the main cause global warming [2]–[5] .

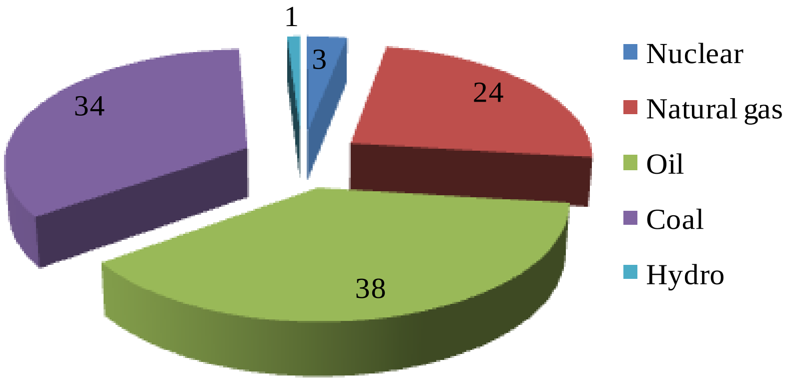

Fig. 1-1 World primary energy consumption (%) in 2012.

Nowadays, manufacturing need an energy-efficient, reliable welding program that not only produces quality welds processes but also saves on operating and electricity costs. One approach to reduce the energy is the new production technology which is a new welding method. This chapter will introduce new welding method, which is the friction stir welding technology including its application. It also proposes the method to study for confirmed the implementation in the industrials. However, this chapter also informs the fatigue damage which is the cause of failure in the structural.

1.2 Principle of friction stir welding and its application

1.2.1 Welding and joining process

Welding is not new. The earliest known form of welding called forge welding dates back to the year 2000 BC. Forge welding is a primitive process of joining metals by heating and hammering until the metals are fused together [6], [7]. Welding is widely used by metalworkers in the fabrication, maintenance and repair of parts and structures. While there are many methods for joining metals, welding is one of the most convenient and rapid methods available. The term welding refers to the process of joining metals by heating them to their melting temperature and causing the molten metal to flow together. Their application ranges from simple steel brackets to nuclear reactors.

Currently, many products are made by construction and manufacturing which is required some type of joining process be used in production of those products. There are three main kinds of material joining processes as shown in Fig. 1-2.

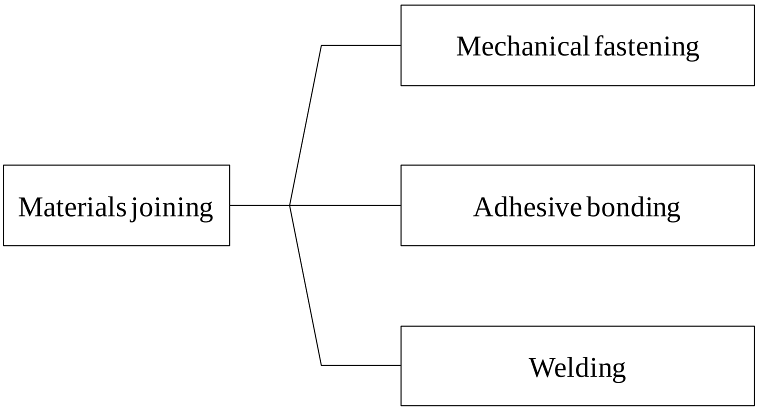

Fig. 1-2 Materials joining process.

The welding is a joining process that produces coalescence of materials intelligible heating them to the welding temperature with or without the application of pressure or by application of pressure alone and with or without the use of filler metal [8]–[11]. Nowadays, there are as many as 94 difference types of welding processes available. Fig.1-3 provides a list of processes used in modern metal fabrication and repair. This list published by the American welding society shows the official abbreviations for each process, such as, RSW stands for resistance spot welding. Shielded metal arc welding (SMAW) is an arc welding process that melts metal by heating with an electric arc created between a covered metal electrode and the metals being joined of the welding processes listed in Fig.1-3, shielded metal arc welding is the most common welding process. The primary differences between the various welding processes are the methods by which heat is generated to melt the metal. Once one understands the theory of welding one can apply it to most welding processes.

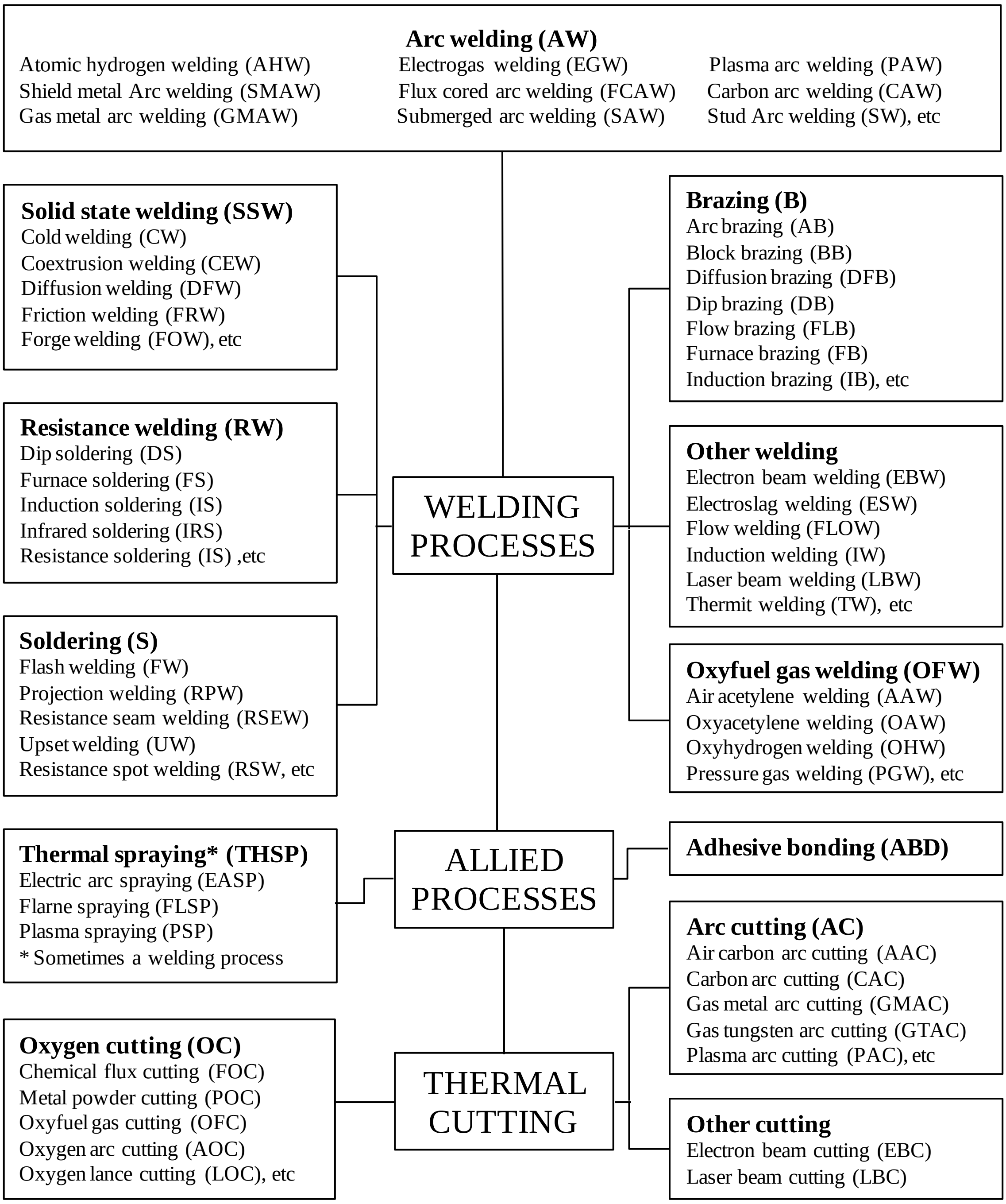

Fig. 1-3 Welding processes.

1.2.2 Friction stir welding

Friction stir welding as FSW, which is a solid-state joining technique, was invented at The Welding Institute (TWI) of the United Kingdom in 1991 in an attempt to aluminum and aluminum alloys [12]–[16]. This relatively new solid-state joining process is energy efficient, environment friendly, and versatile [17]–[19]. Friction stir welding is a continuous hot shear process relating to a non-consumable rotating tool with a specially designed pin and shoulder is inserted into the abutting edges of sheets or plates to be joined and subsequently traversed along the joint line [20], [21]. Figure 1-4 illustrates process definitions for the tool and work-piece. Most definitions are self-explanatory, but advancing and retreating side definitions require a brief explanation. Advancing and retreating side orientations require knowledge of the tool rotation and travel directions. According to Fig.1-4, the friction stir welding tool rotates in the counterclockwise direction and travels into the page (or left to right). The advancing side is on the right, where the tool rotation direction is the same as the tool travel direction (opposite the direction of metal flow), and the retreating side is on the left where the tool rotation is opposite the tool travel direction (parallel to the direction of metal flow). An indigenously designed friction stir welding machine is shown in Fig. 1-5. The machine can rotate the tool pin at up to 3000 rpm, by applying an axial load of up to 30 kN and the transverse speed can be 500 mm/min. And an example of friction stir processing of 1080 carbon steel plate is shown in Fig. 1-6.

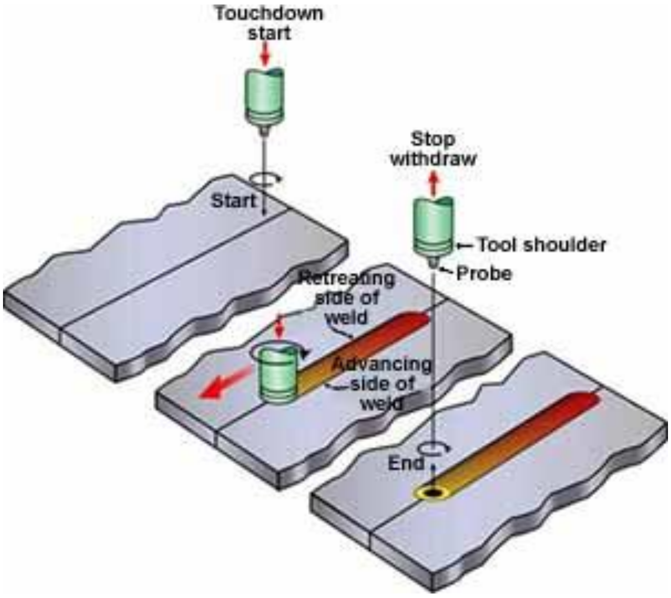

Fig. 1-4 Schematic illustrations of friction stir welding process [22].

Fig. 1-5 Friction stir welding/friction stir spot welding machine [16].

Fig. 1-6 Friction stir processing with the argon gas shield [21].

As a results of the tool action and influence on the work-piece, when performed properly, a solid state joint is produced, that is no melting [23], [24]. Because of various geometrical features on the tool material movement around the pin can be complex, with gradients in strain, temperature, and strain rate. Accordingly the resulting nugget zone microstructure reflects these different thermomechanical histories and is not homogeneous. In spite of the local microstructural inhomogeneous one of the significant benefits of this solid state welding technique is the fully recrystallized, equiaxed, and fine grain microstructure created in the nugget by the intense plastic deformation at elevated temperature. The fine grain microstructure produces excellent mechanical properties, fatigue properties enhanced formability, and exceptional super-plasticity. Figure 1-7 identifies the different microstructural zones existing after friction stir welding, and a brief description of the different zones is presented. The system divides the weld zone into distinct 4 regions as follows:

1. Unaffected material or base metal: this is material remote from the weld that has not been deformed and that, although it may have experienced a thermal cycle from the

weld is not affected by the heat in terms of microstructure or mechanical properties.

2. Heat-affected zone (HAZ): in this region which lies closer to the weld center the material has experienced the thermal cycle that has modified the microstructure and/or the mechanical properties. However, there is no plastic deformation occurring in this area.

3. Thermomechanically affected zone (TMAZ): in this region, the friction stir welding tool has plastically deformed the material and the heat from the process will also have exerted some influence on the material. In the case of aluminum, it is possible to obtain significant plastic strain without recystallization and there is generally a distinct boundary between the recrystallized zone (weld nugget) and the deformed zones of the TMAZ.

4. Weld nugget: the fully recrystallized area, which is called the stir zone, refers to the zone previously occupied by the tool pin. The term stir zone is commonly used in friction stir processing, where large volumes of material are processed.

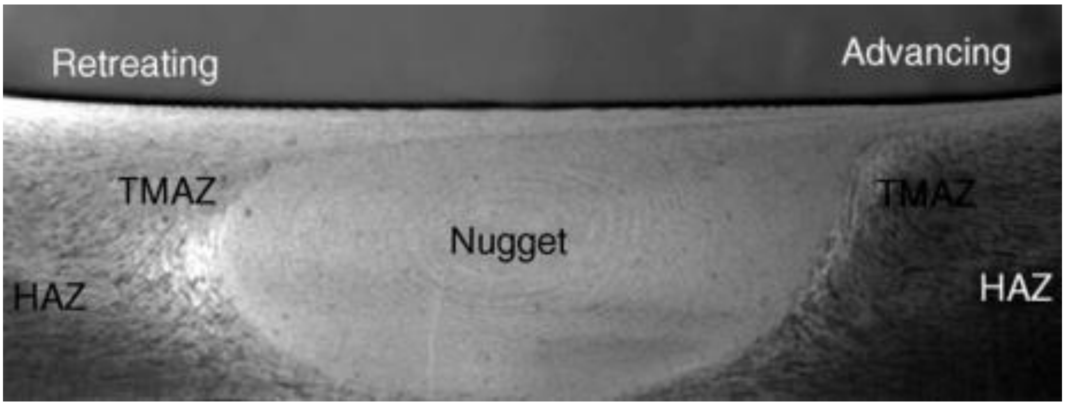

Fig. 1-7 Various microstructural regions in the transverse cross section of a friction stir welded material FSP 7075Al-T651 (standard threaded pin, 400 rpm, and 51 mm/min) [25].

The friction stir tool (shoulder and pin) was manufactured with a different function. Therefore, the best friction stir tool design may consist of the shoulder and pin constructed with different materials [26]–[31], such as the example of tool pin in Fig. 1-8 which is the truncated cone pin and convex shoulder friction stir welding tool. The factor parameter to consider when selecting the friction stir welding tool pin designs are work-piece, materials, joint configuration, welding parameter including to user’s experiences.

Tool shoulders are designed to produce heat through friction and material deformation to the surface and subsurface regions of the work-piece. The tool shoulder produces a majority of the deformational and frictional heating in thin sheet while the pin produces a majority of the heating in thick work-pieces. Also the shoulder produces the downward forging action necessary for weld consolidation. Friction stirring pins produce deformational and frictional heating to the joint surfaces. The pin is designed to disrupt the laying or contacting surfaces of the work piece, shear material in front of the tool and move material behind the tool. In addition, the depth of deformation and tool travel speed are governed by the pin design.

Fig. 1-8 Truncated cone pin and convex shoulder friction stir welding tool [32].

Friction stir welding is considered to be the most significant development in metal joining, and in addition, is a green technology. As compared to the conventional welding methods, friction stir welding consumes considerably less energy, no consumables such as a cover gas or flux are used and no harmful emissions are created during welding thereby making the process environmentally friendly. Furthermore, friction stir welding does not involve the use of filler metal and because there is no melting, any aluminum alloy can be joined without concern for compatibility of composition or solidification cracking issues associated with fusion welding. Also dissimilar aluminum alloys and composites can be joined with equal ease. Additional advantages of friction stir welding compared to fusion welding are summarized in 3 parts as below [15], [33]–[38];

1. Metallurgical advantage
   - Low distortion
   - Solid phase process
   - Good dimension stability and repeatability
   - Excellence of mechanical characteristics in the welded zone
   - Virtually defect-free welding
   - Join dissimilar materials

2. Energy advantage [39]–[41]
   - Only 2.5% of the energy needed for a laser weld
   - Decreased fuel consumption in lightweight aircraft, automotive and ship applications

3. Environmental advantage
   - No shielding gas required
   - Low energy input and lack of fumes, gases, etc., resulting from the process, makes-

FSW friendly to our environment

- Eliminate grinding wastes

1.2.3 Friction stir spot welding

Friction stir spot welding (FSSW) [42]–[48] is a new relatively recent trend for joining materials which is a new application of friction stir welding technique. Friction stir spot welding has been developed as superior alternative to resistant spot and riveting for fabricating automobile and railway body components[35], [38], [49]–[51]. This technique was invented at Kawasaki Heavy Industries Ltd. in 2000 as a variant of a linear friction stir welding method [37], [52]–[54]. Further, in 2003, friction stir spot welding was first used to fabricate in rear door panel of Mazda RX8 [48], [55], [56]. Mazda proved to have reduced the energy consumption by 99% of the used by the conventional welding process [57].

The friction stir spot welding method was evaluated an alternative welding technique used for lightweight materials assembly is one of key technology leaded to enhance weight reduction in the automobile industries which was important in the automobile industries in the order to improve fuel economy [33], [43], [58]. Those materials such as aluminium, titanium and magnesium, can be used to replace equivalent steel assemblies with approximately half the weight after appropriately designed. Figure 1-9 illustrates the friction stir spot welding process. The process is applied to a lap joint consisting of upper and lower sheets. A rotating tool with a probe is plunged into the material from the top surface for a certain time to generate frictional heat. At the same time, a backing plate contacts the lower sheet from the bottom side to support the downward force. Heated and softened material adjacent to the tool causes a plastic flow. In addition, the tool shoulder gives a strong compressive force to the material. After the tool is drawn away from the material, a solid phase bond is made between the upper and the lower sheets. Figure 1-10 shows the friction stir spot welded joints and the cross-sectional area configuration of the welded joints. The upper surface of the weld looks like a button with a hole, and the bottom surface is kept almost flat. In the cross-section, there is a hole that is made by the tool pin which is the shoulder and probe, and reaches into the lower sheet.

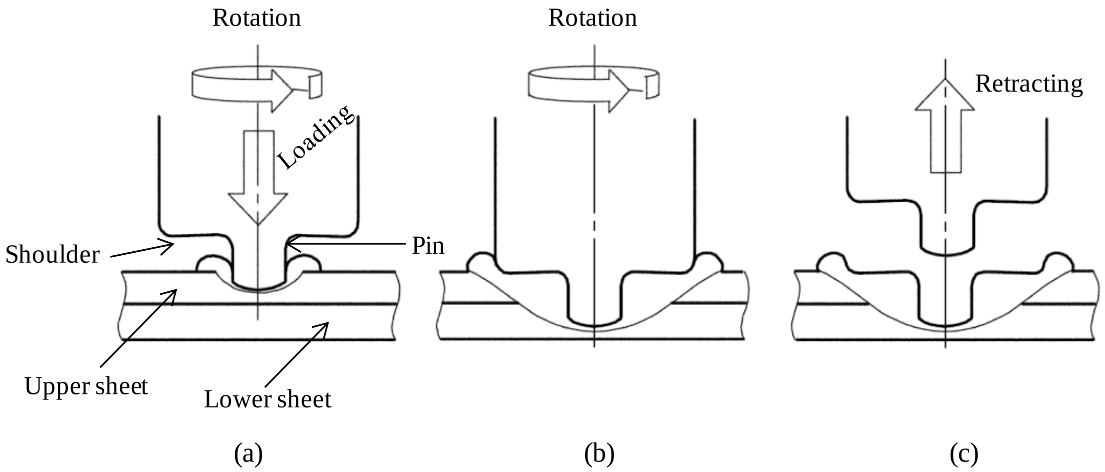

Fig. 1-9 Schematic illustration of FSSW: (a) Plunging, (b) Rotating, (c) Drawing out.

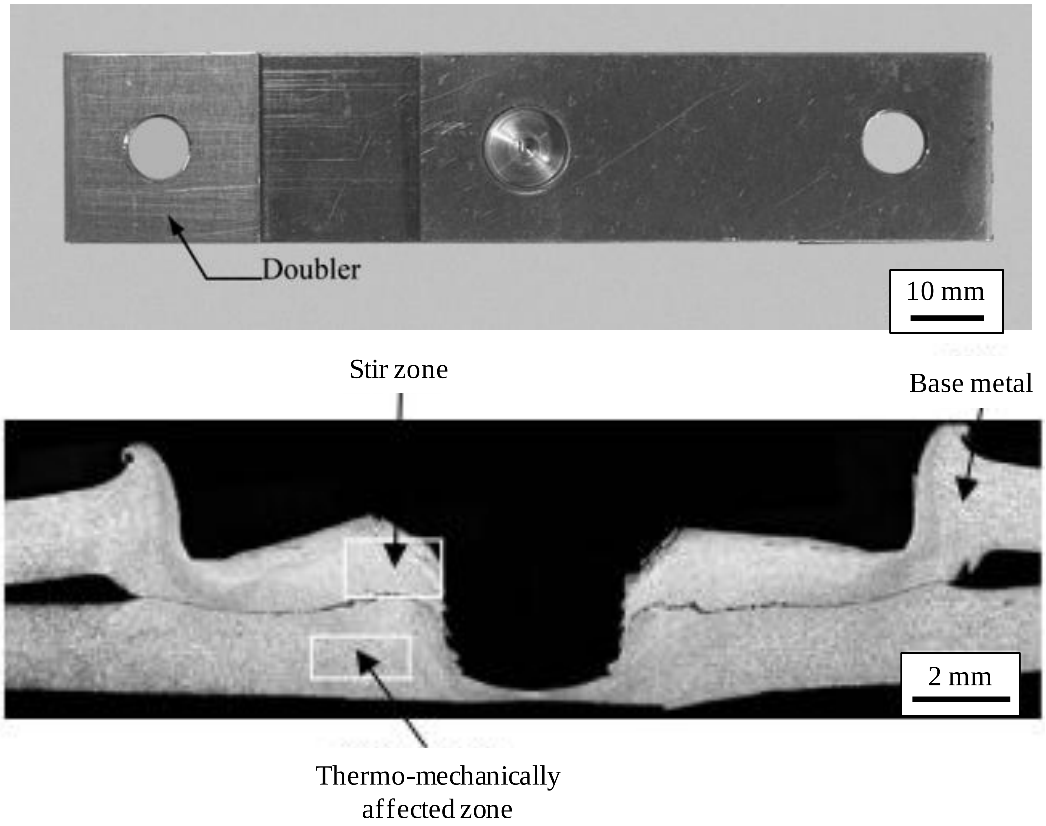

Fig. 1-10 The friction stir spot welded joints and the cross-section area [54], [59].

1.3 Fatigue

Fatigue a mainly cause of failure, especially in weld structure considering the physically poor fatigue performance of the weld joints [60]. Fatigue damage has been important aspect of designing automobile parts to perform a specific function for their safety and reliability. Fatigue life is one of the most important properties when designed the automotive components. Most engineering components contain discontinuities geometric, such as holes, shoulders, keyways grooves, and notches. When the component is loaded, local stress and strain concentrations are generated in their areas. The stress often exceeds the yield limit point of the small area around the concentration point, equal to relatively low nominal elastic stresses. The cyclic inelastic strain in the concentration area of stress and strain may cause by formation of crack and grow lead to the component failure, when the concentration areas is subject to cyclic loading. The crack occurred from a shallow of the stress concentrations areas. The fatigue behavior has a commanding influence by crack initiation. The cracks that initiate from the shape of component often nucleate quickly due to the hold up local stresses, and crack growth often dominates the fatigue behavior. Schijve et al. [61] has used the picture shown in Fig. 1-11 to survey prediction problems associated with fatigue properties of structures. The prediction is the output of a number of procedures and presents the scenario of the various aspects involved. The input problems occur in three categories; design work, basic information used for the predictions and fatigue load spectrum to which the structure is subjected. Each of the categories contains a number of separate problems, which again can be subdivided into specific aspects, such as a joint, cover welded joints and adhesively bonded joints. Figure 1-11 illustrates that the full problem can be very complex depending on the structural design, type of material, production variables, load spectrum and environment. The prediction of the fatigue performance of a structure is the result of many steps of the procedures adopted and in general a number of plausible assumptions are involved. It implies that the accuracy of the final result can be limited, the more so if statistical variables also have to be considered. The reliability of the prediction should be carefully evaluated, which requires a profound judgment, experience and intuition.

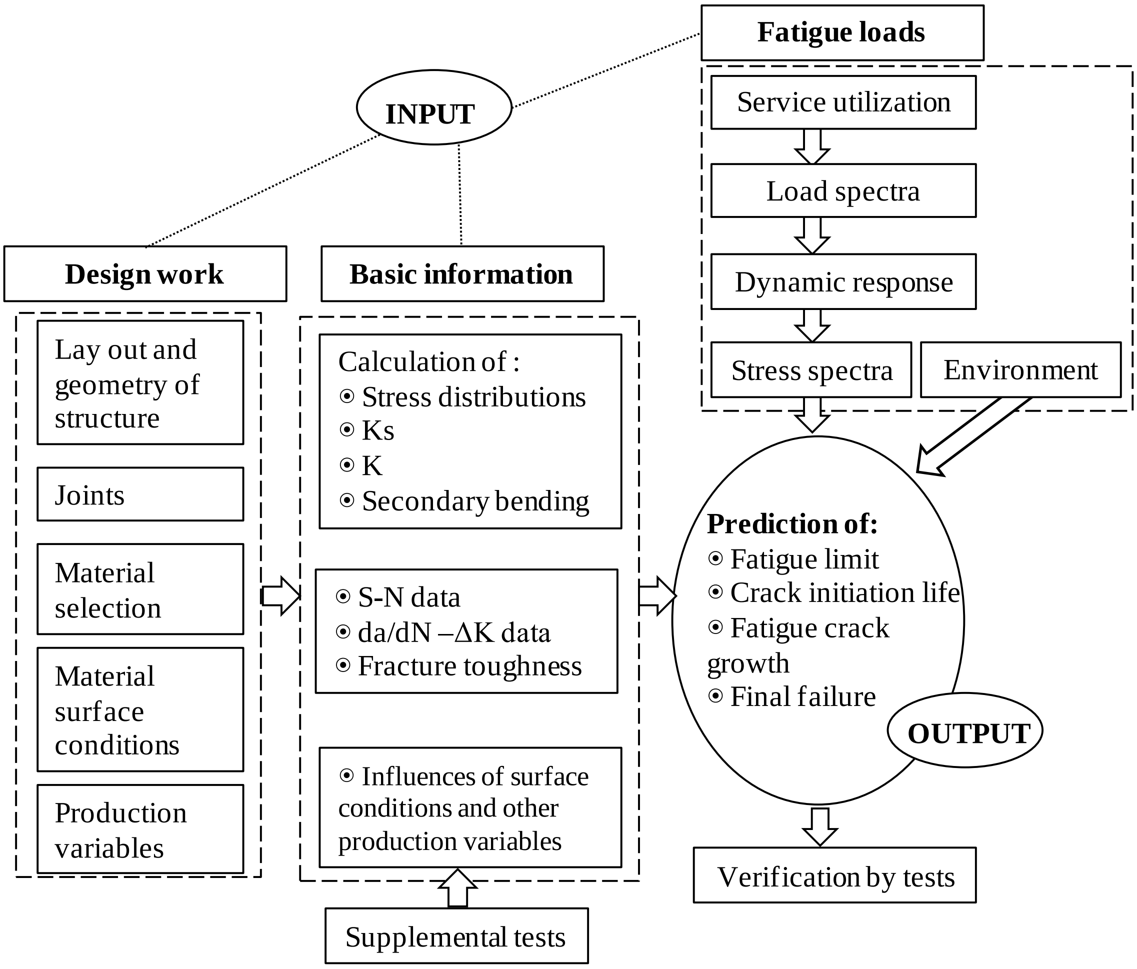

Fig. 1-11 Survey of the various aspects of fatigue of structures.

1.4 Objective and scope of present research

With FSSW, energy consumption and operational cost are significantly lower than other welding methods such as arc, laser, and gas welding techniques. And, the successful application of FSSW technology has attracted considerable attention from the automotive industry. Previous research of FSSW has focused on microstructure analysis, mechanical properties, and how to produce a joint that optimizes the corresponding parameter sets. However, to this end, most previous studies of mechanical properties have employed only static tensile and hardness tests [33], [62]–[64]. Few authors have performed fatigue tests on alloy series to analyze the strain behavior [65], [66] or determine fatigue life, failure modes, and microstructure of the failed specimens[35], [53], [67]. Some studies have reported on the FSSW of carbon steels [68]–[70]. However, few reports exist on the fatigue fracture mechanism and fatigue crack propagation behavior in FSSW-joined carbon steel, particularly for cross-tension FSSW specimens [58]. Moreover, some stress concentration parts remain at the area welded by FSSW: a hollow called a keyhole caused by the tool shape, a discontinuity in shape called a lip, and a slit between the upper and lower sheet. Furthermore, the area welded by FSSW has several microstructures: the heat-affected zone (HAZ), thermo-mechanically affected zone (TMAZ), and stir zone (SZ). It is highly advantageous to identify the relationship between the shape of the welded area unique to FSSW, the microstructure, and the fatigue crack behavior; however, details are not definitively known. Moreover, most studies on the fatigue properties of FSSW joints were conducted under constant force amplitude conditions; although some studies have reported the fatigue properties under variable force amplitude conditions [19], [71]. However, automobile loads randomly vary in service and very little is known about fatigue properties under random force amplitude conditions, which are assumed to occur in actual force situations.

Herein, fatigue tests were performed under constant force amplitudes to investigate the fatigue properties and fatigue fracture mechanism of FSSW-joined AISI 1012 cold-rolled steel sheet. Welded components are often subjected to variable force amplitudes, which call for fatigue life prediction methods that consider fatigue damage accumulation. Therefore, this study proposes and demonstrates the effectiveness of a method for evaluating cumulative fatigue damage under variable force amplitude conditions which are including repeat two-step and random force amplitude.

1.5 Organization of the thesis

The general of the thesis is divided into 7 chapters excluding the first chapter is the introduction which cover the literature reviews and the conclusion as a last chapter. The thesis is outlined as follows:

Chapter 1; Discusses the background of the research as well as the introduction of welding processes particularly friction stir welding and friction stir spot welding objective scope of the research and organization of the thesis.

Chapter 2; Reviews the theoretical background and the present researches on friction stir welding and friction stir spot welding and related research that lead to make the optimum joints. The fatigue mechanisms of welded joint under constant amplitude loading are discussed. The cumulative fatigue damage under variable amplitude loading is detailed to clearly understand the cracking phenomena and the systematic approach of prediction the fatigue life. This includes fatigue as a material phenomenon prediction models for fatigue properties of structures, and load spectrum.

Chapter 3; The base material, shape and type of specimen, and experimental methods for all the experiments conducted in the present work are explained in this chapter. Experimental procedures of the hardness test, the static tensile test, the fatigue test under service loading, and strain measurement are also described.

Chapter 4; This chapter cover the fatigue test under constant force amplitude conditions. This study have investigate the fatigue properties and crack growth behavior of friction stir spot welded AISI 1012 cold rolled-low carbon steel sheets used as the general automobile steels. Furthermore, fatigue crack initiation and fatigue crack propagation were observed by using the three-dimensional observation.

Chapter 5; The fatigue tests were performed under repeated two-step force amplitudes to investigate the fatigue properties of FSSW-joined AISI 1012 cold-rolled steel sheet by using the results of fatigue tests under constant force amplitude from the chapter 4. Welded components are often subjected to repeated two-step force amplitudes, which call for fatigue life prediction methods that consider fatigue damage accumulation using Miner’s rule and modified Miner’s rule. Two cases of repeated two-step fatigue test were considered: in the first, macroscopic plastic deformation near the welded zone did not occur. Within the testing conditions, the fatigue damage evaluation using Haibach’s method. And in the second, significant plastic deformation occurred. This case is important to consider a cumulative damage estimation that takes into account the effect of pre-strain from the high force amplitude.

Chapter 6; This chapter was evaluating fatigue damage of cross-tension specimen by using friction stir spot welding technique, under random force amplitude conditions. The damage evaluation was conducted using the power regression equation was obtained from *P*-*N* curve. The difference bandwidth of the random force amplitude signal was obtained by digital simulation which simulated using the stationary Gaussian random process. The capabilities of rainflow cycle counting method and Miner’s linear damage rule are used. Finally, the modification method was used. The modification method by Corten-Dolan’s method was proposed using the fatigue test under repeated two-step force amplitude was investigated for the effect of frequency ratio base on the results under constant force amplitude from previous study.

Chapter 7; In this chapter, the thesis is concluded making clear the experimental results.

CHAPTER 2

Literature reviews

2.1 Introduction

This chapter discusses the theory background and previous researches on friction stir welding and friction stir spot welding. Also, those researches are related to the welding parameter due to the optimum of welded joints and the successful of the welded joints on several kinds of material. Moreover, reviews the properties on dynamic and static test such as tension, fatigue and failure. The literatures review also provided a thought background and theory on the fatigue damage with the aim of well understanding of the research on prediction and fatigue damage based on the similarity of conditions and damage accumulation.

2.2 The previous studies on of friction stir welding and friction stir spot welding

Several previous researches of friction stir welding and friction stir spot welding studies the corresponding parameters used to make the joint that leads to better parameter sets. The applications of friction stir welding to materials have been limited due to the absence of suitable parameters such as tool pin, tool rotational speed and tool travel speed [72]–[82]. Sun et al. [13] studied microstructure and mechanical properties dependent on the welding parameter of friction stir welded joints of pure copper under variant welding parameters included rotational speed of 200-1200 rpm, welding speed of 200-800 mm/min and applied load 1000-1200 kgf. However, the welded properties were made to associate the change with the variations in the welding parameters such as the increases of applied load have an effect on microstructure refinement, increasing the hardness value and ultimate tensile strength. Ghosh et al. [36] evaluated the influence of process parameters of friction stir welded joints ultra high strength steel on the strain rate and stress. The faster travel tool speed responded in higher strain rate and lower peak temperatures. And it would mainly cause for controlling the dynamically recrystallizion of austenitic grain size and the variation of recrystallized austenitic grain size as shown in Fig. 2-1, which can obtained by power law relationship with the Zener-Hollomon parameter.

Badarinarayan et al. [47] studied the effect of tool geometry of friction stir spot welded aluminum alloy with a cylindrical pin and a triangle pin. This study found that the tool pin geometry has significant effects on the hook formation, grain size, and material deformation. In addition, the tensile strength of welded joint made with the cylindrical pin is a half that of welded joint made with triangle pin. Rajakumar et al. [83] have reported the effect of tool geometry and varying process parameters on microstructure and hardness value of friction stir welded AA7075-T6 joints. The optimum joints process was success with the parameter of tool rotational speed of 1400 rpm, welding speed of 60 mm/min and applied force 8.0 kN with tool parameter of 15.0 mm of tool shoulder diameter, 4.0 mm of pin diameter and 45 HRC of tool hardness that detect free fine grain microstructure of the weld nugget and the joints yielded higher strength compared to the other joints.

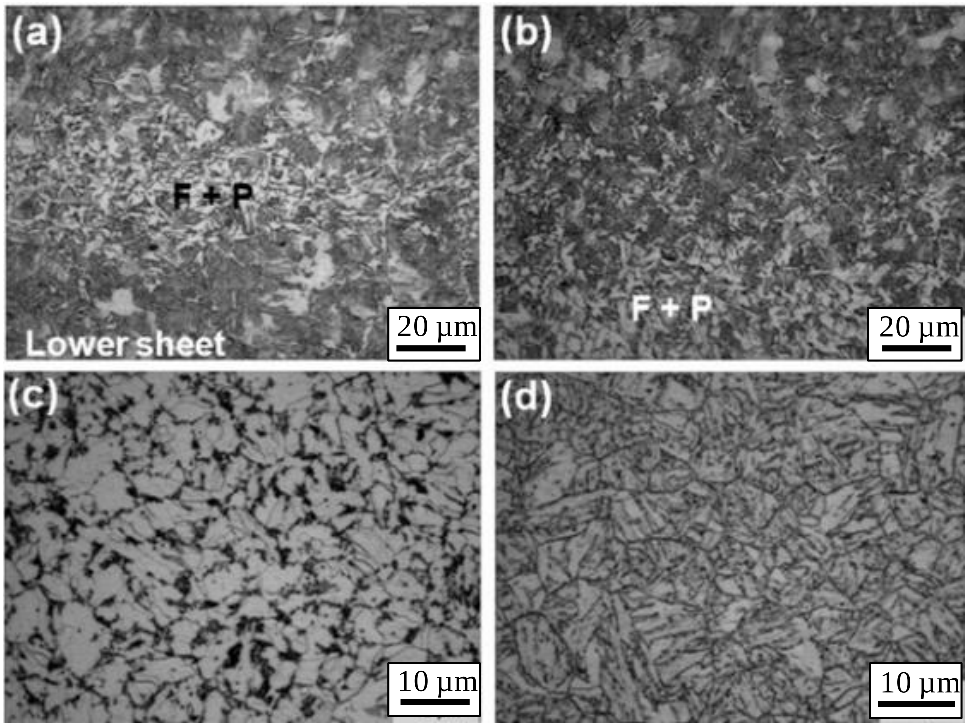

Fig. 2-1 Microstructure of sample 2: (a) ferrite+pearlite at the faying surface, (b) ferrite+pearlite at the bottom of second sheet, (c) HAZ-1, (d) HAZ-2 [36].

Yang et al. [42] described the material flow during friction stir spot welding of AZ31 Mg sheet by using three different tools that material flow of each zones were difference such as on flow transition zone, material flow was induced by shoulder and pin. An incorporation of upper and lower sheet materials takes place and intermixed materials flow towards the pin. The materials flow expanded the material outside the stir zone, flow towards the pin direction following farthest point and be force directly the stir zone. In addition, in the torsion zone, the material beneath the pin moves downward in the swirling motion. Nandan et al. [84] calculated three dimensional heat and material flow during friction stir welding on experimentally and theoretically. The computation method was used non-Newtonian viscosity with the computed value of strain rate, material properties and temperature. The predicted temperature versus time plot, and torque value was good agreement with experimental results. Moreover, the significant plastic flow occurred near the tool especially on the retreating side. Su et al. [85] investigated the material flow during friction stir spot welding of dissimilar Al5754/Al6111. This paper described that upper sheet material was moved downwards into the lower sheet on an inner flow zone nearly to pin. And, the lower sheet material was displaced upwards and outwards in a spiral movement on an outer flow zone. As shown in Fig. 2-2, the results correspond with some indicate found during numerical modeling of material flow, that there was a rotational flow around the pin. In Fig. 2-2(a), incorporation of tracer during spot welding, showing material displacement upwards and outwards and tool rotates in anticlockwise direction that the particle tracer is sequence as shown in Fig. 2-2(b).

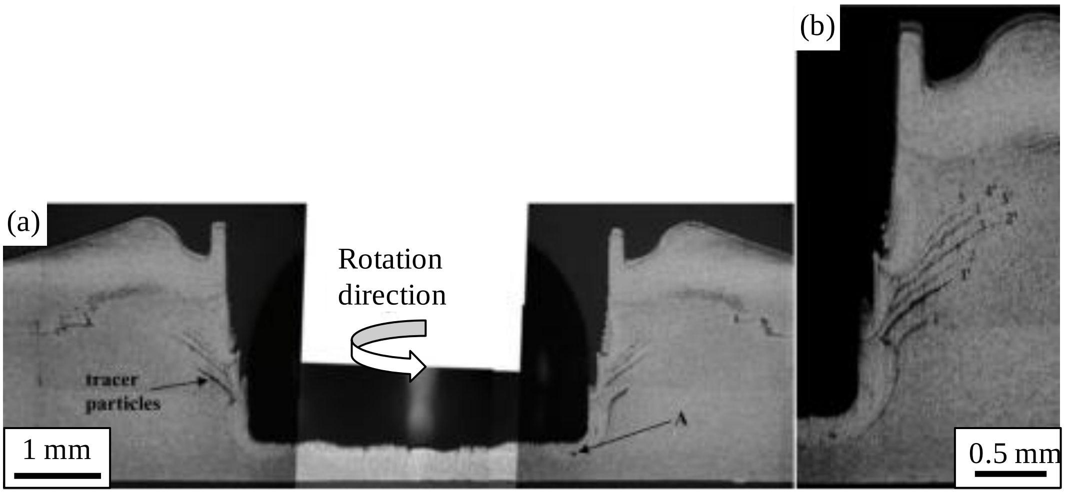

Fig. 2-2 Displacement of Al_2O_3 tracer material during spot welding of Al 6061–T6 [85].

Krishnan [86] explained the formation of onion rings in friction stir welding due to the process of friction heating as the rotating tool and movement extrudes the material around the retreating side. The appearance of the onion rings was found to be geometric effect that cylindrical sheet are extruded during rotation of the tool.

However, friction stir welding is solid-state joining method and has been widely used and investigated for low melting materials such as Aluminium [87]–[92], Boron [43], Magnesium [93]–[95], Copper alloys [96]. Recently, many reports have research on several types of steel sheets, such as plain carbon steels [97]–[101], stainless steel [102]–[106] and high strength steel [107], [108]. In addition, these steels were successfully welded and their microstructures and mechanical properties were studied. For example, Fujii et al. [109] determined the effect of carbon content and transformation on mechanical and microstructure of friction stir welded three types of carbon steel with difference carbon content and various welding condition. The low temperature of welding process of carbon steel was successful around 650 ^{o}C without any transformation as shown in Fig. 2-3. S12C joints were increases tensile strength with the increasing welding speed. The welded joints are performed in ferrite-austenite dual phase that the microstructure was refined grain and highest strength was achieved. Although several demonstration of friction stir welding and friction stir spot welding materials such as Chung et al. [68], [110] successfully produced friction stir spot welds in high carbon steel in 0.72%C and 0.85%C steels at variant welding parameter without martensite transformation that the joints of high carbon steel performed peak temperature as shown in Fig. 2-4. In Fig.2-4 (F-H) consisted fine ferrite with globular cementite, similar to microstructure in Fig.2-4 (A and E) which was locate in base metal. Therefore, below A_1 condition has been successful achieved, since without transformation and no martensite forms. These results indicated that the joints have good mechanicals properties and toughness.

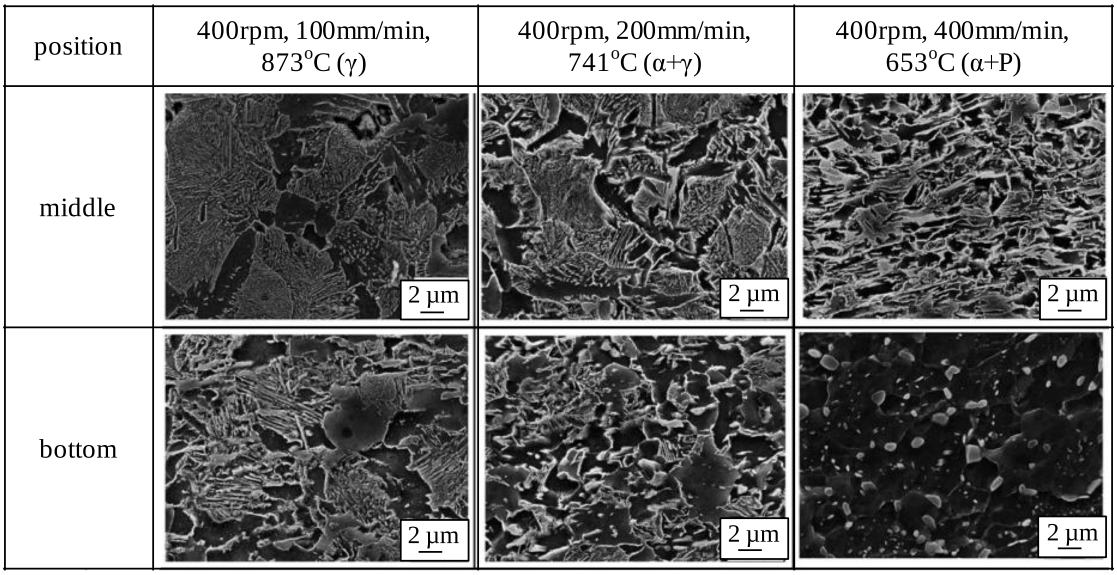

Fig. 2-3 SEM microstructures of the stir zone in S35C FSW joints [109].

Choi et al. [111] successfully welded high carbon steel by friction stir welding with without a gas torch. Aldajah et al. [21] experimentally studied effect of tribological performance of friction stir welded 1080 high carbon steel. Moreover, high carbon steel, S70C with carbon content 0.72% was successfully welded friction stir process without any heat treatment. This process is developed by Cui et al. [70], the results indicated that martensite transformation is uncertain only in the friction stir welding process of high carbon steel. The matensite formation is related with the post-treatment cooling rate and the temperature cycles during the friction stir welding process showed that the cooling occurred after the tool pin passed.

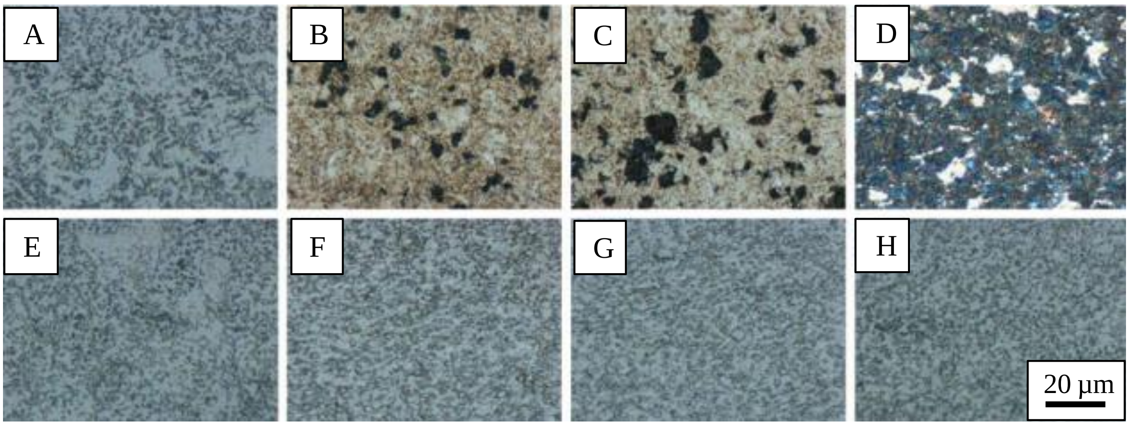

Fig. 2-4 The specimen for the optical microscopy observations was cut perpendicular to the welding direction: microstructure of the base metal (A and E), the joint formed above A_1 (B–D), the joint formed below A_1 (F–H) [68].

The friction stir welding and its application allow for the possibility of joining high strength steel with the low welding temperature such as API grade, DP600 and M190 [36], [56], [112]–[115]. Nowadays, this steel is still the mainly material for body structures of high-volume mass-produced cars by all major car makers. The great emphasis on safety and vehicle weight reduction to improve fuel efficiency has been driving the increased use of AHSS in automobile body construction. Thus, this steel should be joined with a low heat input and high welding speed, and friction stir welding has attracted attention as an alternative welding process in the manufacture of a pipeline. For example, Cho et al. [112] studied evolution of microstructure during friction stir welded API X100 pipeline steel with a complex process. This paper reports that during friction stir welding process, the various grain structures developed including dynamic recrystallization in the thermomechaniclly affected zone and acicular-shape bainite ferrite phase transformation in stir zones. Regarding to the researches on mild steel, aluminum and its alloy, there are many studies are reported the friction sir welding and its application [17], [43], [51]. Many researches is gaining popularity for joining light-weight materials like aluminum, copper, magnesium as used in automotive body. Lee et al. [51] used friction stir welding process for joining of copper 4 mm thick with general tool steel. The paper founded that friction stir welding process can be successfully applied to join copper which defect free weld zone with insert speed 61 mm/min and tool rotational speed 1250 rpm. Friction stir processed AZ91/SiC composite joint was proposed by Asadi et al. [116] by improved the effect of process parameter such as traverse speeds, tool penetration depth, formation of crack, and sticking of matrix material. This paper founded that SiC particle is used as reinforcement and grain size of surface composite layer of AZ91/SiC is refined. Increasing in the rotational speed and increasing in the traverse speed leads to a decrease in the grain size as explain in Table 2-1.

Table 2-1 Effect of rotational and traverse speed on grain size and microhardness [116].

Rotation speed (rpm)	Transverse speed (mm/min)	Grain size (mm)	Microhardness (HV)
900	12.5	16.74	75
	25	10.94	79
	40	9.79	84
	50	8.77	88
	63	7.16	94
1,400	12.5	25.76	69
	25	20.85	71
	40	16.94	75
	50	14.08	78
	63	12.96	83
	80	9.90	89

Aluminum and its alloys are strong and offer significant light weight materials. Hence, applications stretch from automotive industries by replacing heavy steel. A rapid development of applications of lightweight materials in the automotive industry is reflecting in the increasing use of aluminum. Nowadays, many works of friction stir welding and friction stir spot welding have been carried out concerning of several difference aluminum alloys such as AA7075-T6 [83][117][118], AA6061-T6 [119], [120], AA5083 [121], AA5754 [122] and AA2014-T4 and T6 [55]. Babu et al. [55] has been studied in aluminum alloy AA2014-T4 by using friction stir spot welding with microstructural analysis and mechanical properties. The optimum welded joints can be achieving satisfactory with good correlative between process parameter, joint formation and joint strength. There is considerable interest in the aerospace industry as well, as the use of FSSW in place of riveting in aluminum structures can potentially result in considerable weight savings as well as reduced assembly times and costs. Other than that, some researchers are studied on titanium alloy. For example, Zhou et al. and Pilchak et al. [123], [124] were investigated friction stir welding on T1-6Al-4V titanium alloy. Zhou et al. concluded that the welding rotational speeds have a significant effect on the microstructure and mechanical properties of the joints. A full lamellar microstructure could be developed in heat affected zone and not influenced by rotational speed. Moreover, the tensile strength of the joints was lower than that in the base metal, and the tensile strength was decreased tensile strength with increasing rotational speed as shown in Fig. 2-5.

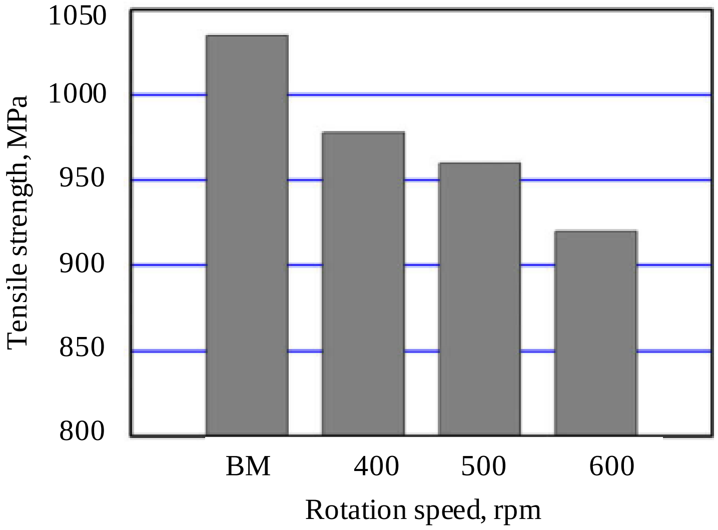

Fig. 2-5 Effect of rotation speed on transverse tensile properties [123].

Once the friction stir welding and its application were successfully then achieved on some materials. The mechanical properties have been studied on the welded joints including to hardness value, static strength, fatigue strength and fracture analyses [125]–[132]. Many previous researches show that the strength of friction stir spot welds mainly depends on the size of the welding region which is closely related to welding conditions and tool rotational profile. Bozzi et al. [48] proposed the influence of the friction stir spot welded tool rotational speed on tensile shear strength on aluminium 5182-O alloy. The results found that the tensile shear strength of the welded joints was found to mainly depend on microstructural features and the probe plunge depth with the friction stir spot welds fail by nugget pullout. The tensile residual stresses were increased with the rotational speed, and then the tensile strength thought concentration effect around the interface tip (Fig. 2-6). Badarinarayan et al. [47] concluded the mechanical performance of friction stir spot welded aluminium alloy on effect of tool geometry. The tool pin geometry significantly affects the hook. The joint strength is determined by the failure mode and the microstructure. Under the same process condition, the tensile strength of the joint made with the triangular pin is 2 times the welded joint made with the cylindrical pin. In particular, an assessment of microstructure, and mechanical properties of friction stir welded ferritic stainless were investigated by Lakshminarayanan et al. [133], proposed that grain size and static strength investigation through the weld. Zadpoor et al. [117] found that the global and local mechanical properties of friction stir welds with dissimilar materials. The fracture mechanism of friction stir welded specimen was found to be mixtures of ductile and brittle fracture as the definition of quasi-cleavage fracture, an example is shown in Fig. 2-7. Moreover, there are also studies fracture mechanisms in several reports[134]–[141]. Jonckheere et al. [35], Borino et al. [142], Pathak et al. [122] and Wang et al. [37] have studied the tensile strength and fracture of friction stir spot welds and its application, for instance Jonckheere et al. found that the fracture initiating at the triangular cavity and locating the thermomechaniclly affected zone by pullout the welded nugget. This fracture type leads to significant plastic deformation and generally large ultimate static strength.

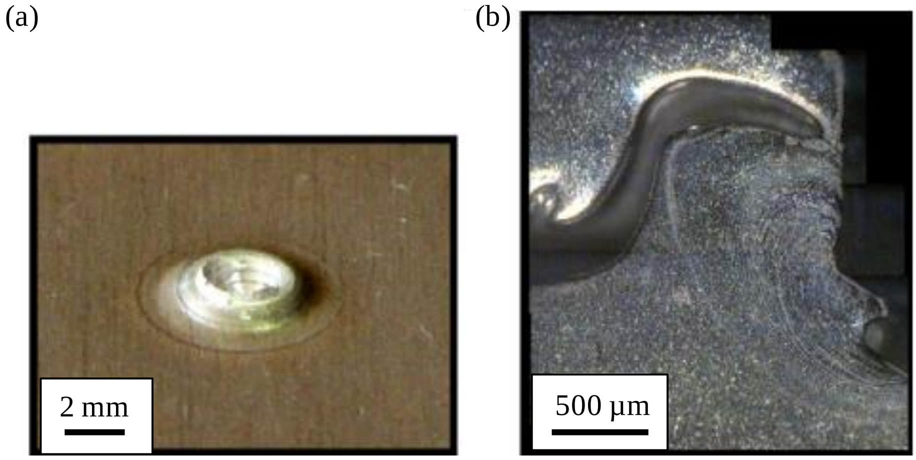

Fig. 2-6 (a) Nugget pullout in a failed lap-shear specimen, (b) cross-section of an interrupted shear loaded specimen showing the crack propagation around the stir zone [48].

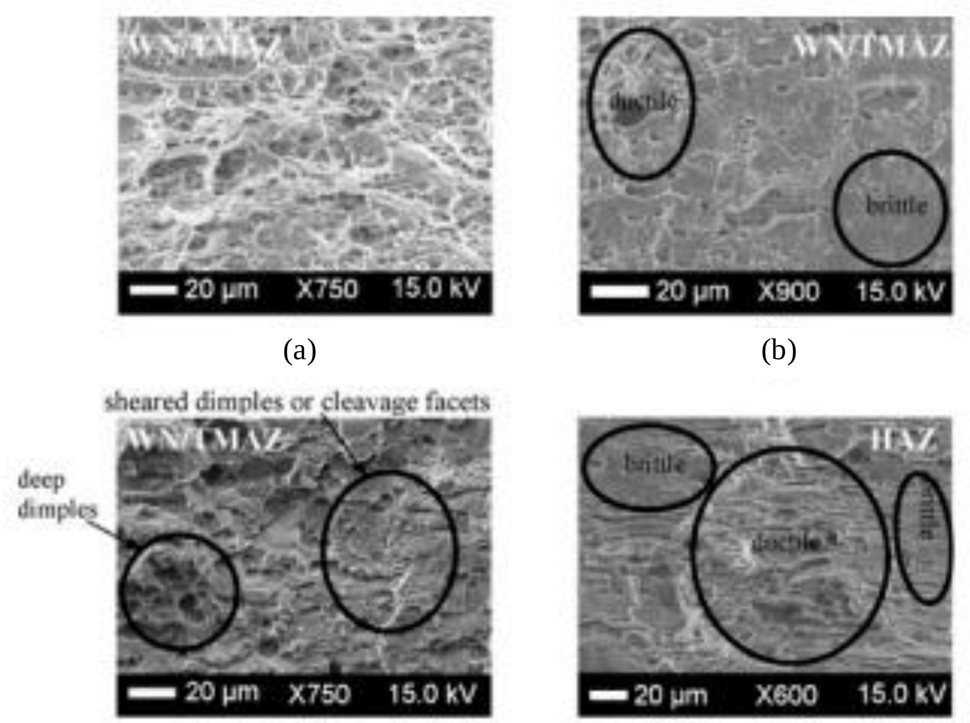

(a) (b)

(c) (d)

Fig. 2-7 Fracture surfaces of sample welds from some configuration [117].

In addition, the fatigue properties have been largely studied by several researchers including to fracture analysis, fatigue strength and failure mode. For example, Bussu et al. [143] and John et al. [15] have studied the effect of residual stress on the fatigue propagation of crack. Jata et al. [144], Lin et al. [53], [54], Malafaia et al. [46], [145], Tran et al. [67], [146], [147], and et al [148], [149] have studied the fatigue properties of welded joints produced by friction stir welding and its application. Bussu et al. [143] concluded that the fatigue crack propagation behavior and crack growth were sensitive to the weld orientation and distance from the crack lines. In addition, residual stress was mechanically relieved and effect on crack propagation as shown in Fig. 2-8. The failure modes and fatigue life estimation of friction stir spot welded joints were reported by Lin et al. [53], [54]. These researches have studied failure mode of spot friction welded lap-shear specimen of aluminium alloy produced by flat tool and concave tool. The results found that the micrographs shown the microstructure, geometry and failure modes of the joints made by the flat tool are slightly different from those of the joints made by the concave tool. The fatigue crack growth model presented in concave tool is adopted to estimate the fatigue life of the joints produced by the flat tool. In addition, the fatigue life estimation base on the crack growth model and experiment result were gave agree well.

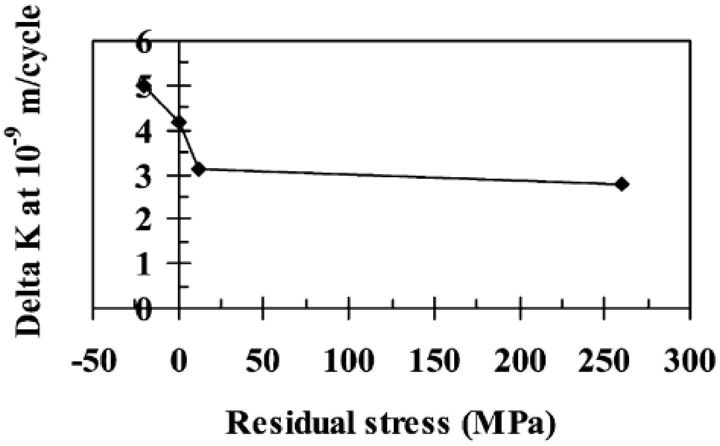

Fig. 2-8 Δ*K* to produce a growth rate of 10^{-9} m cycle^{-1} plotted against the residual stress measured at the starting defect location [143].

Malafaia et al. [46] proposed that this study was compare the fatigue resistance of the welded joints produced by friction stir spot welding and riveted joints. The friction stir spot welded joint exhibited shorter lives in fatigue comparing to rivet joints. The fatigue failure modes were observed to two types. The first mode was presented in the tension shearing mode which occurring for high load level and the second mode, with the transverse cracks which observed in some high-cycle test with load level applied. Tran et al. [67] investigated the fatigue behavior of friction stir spot welded aluminium alloy in lap shear specimen under quasi-static and cyclic loading. Under both of loading conditions, the failure modes of welded joints are slightly different such as under quasi-static, the weld joints mainly fail from the nearly the flat fracture thought the nugget as shown in schematic plot of the cross-section in Fig. 2-9. The weld joints mainly crack from the kinked crack thought the nugget under low-cycle loading, and, the weld joints mainly crack from the kinked crack thought the upper and lower sheet thickness under low-cycle loading. In addition, the kinked crack growth model on stress intensity factor and structure stress model were adapted to estimate the fatigue lives of the welded joints. Moreover, Tran et al.[146], [147] have studied the fatigue failure mode of friction stir welded joint of the dissimilar lap shear specimens. Uematsu et al. [58] have studied the dissimilar friction stir spot welded between aluminium and low carbon steel on the fatigue behavior. This research results found that the fatigue fracture modes of the welded joints were dependent on fatigue load level while shear fracture occurred on the nugget under high load level and grew though the aluminium sheet under low loading levels.

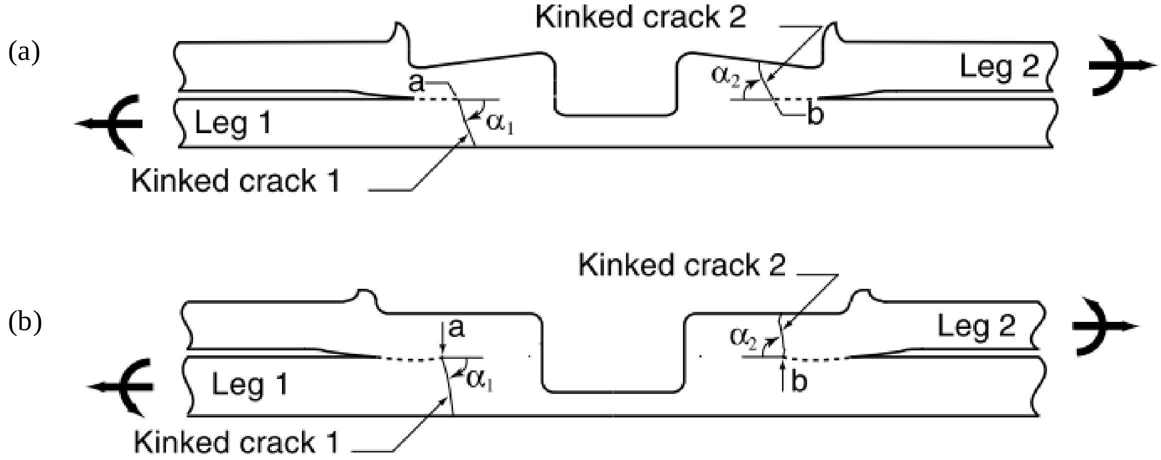

Fig. 2-9 A schematic plot of the cross-section along the symmetry plane of the spot friction weld under a statically equivalent combined tensile and bending load (shown as the bold arrows): (a) Al5754, (b) Al6111 [146].

2.3 The previous studies on prediction and fatigue damage

Fatigue damage has been important aspect of designing automobile parts to perform a specific function for their safety and reliability. The prediction of fatigue properties of the structure and avoiding structural fatigue were recognized an engineering problem. This section will descript the fatigue damage which is divided to 2 parts, the predictions based on the similarity of conditions or constant amplitude loading, and damage accumulative or variable amplitude loading.

2.3.1 Predictions based on the similarity of conditions

The physical of similarity approach is similar condition applied to the similar system, then, it should produce the same consequence. This principle is the basis of many predictions of properties of materials and structures. It can also be applied to fatigue prediction. It should be realized that the physical mechanism of the fatigue characteristics must be understood. For example, the fatigue of notched elements the similarity concept implies that the similar stress cycles applied to an un-notched specimen and to the material at the root of a notch in a notched specimen will give the same crack initiation life. It is not essential to know how the initiation occurs. The requirement of similar systems implies that the un-notched and notched specimen should be of the same material. However, some other aspects which may violate the similarity are easily recognized. A significant aspect is that the stress cycle in the un-notched specimen is present in a large volume of the material with a relatively large area of surface material. In the notched specimen, the stress cycle of the peak stress or nominal stress (K_t) at the notch root is present in a relatively small volume of the material with a relatively small surface area.

2.3.2 Predictions based on the damage accumulation

Disposal of accumulative fatigue damage has received a large amount of attention during the century. Many investigations have been carried out to develop the prediction model for the fatigue life, when it takes a time and strength to construct a stress-fatigue life curve (*S*-*N* curve). The first method has known as a linear damage rule which is proposed by palmgren [150]. The same rule was later independently suggested by Langer [151] and Miner [152]. Langer proposed that the fatigue damage process separated into two stages of the crack initiation and crack propagation. After that, Miner represented first the Palmgren linear damage concept in mathematic form. The applicability of Palmgren and Miner cumulative fatigue damage has been reported which called as Palmgren-Miner rule (P-M rule) is often appropriated for many kind of materials. The Palmgren-Miner rule is given by Eq. (2-1)

$$\sum \frac{n}{N_f} = \frac{n_1}{N_{f1_1}} + \frac{n_2}{N_{f2_1}} + \cdots = 1.0 \tag{2-1}$$

when n_1 is the number of cycles at the stress/strain range level 1, and N_{f1} is the number of cycles to failure at that stress/strain range, etc. The experimental results do not support the postulate. When cyclic loading of high stress/strain range are applied first followed by the lower range until the specimen was broken. In this case the summation of the cyclic ratio is generally less than unity. On the other hand, for the reverse case, the cyclic loading of low stress/strain range are applied first followed by the higher range until the failure takes place, the summation of the cyclic ratio is greater than unity. Coffin et al. [153] expressed the linear damage rule in the term of plastic strain range, which was relate to fatigue life thought the Coffin-Manson relation [154]

Fatemi et al. [155] proposed a comprehensive review of the cumulative fatigue damage theories for the metals and its alloy. Since the introduction of cumulative damage proposed by Palmgren and linear damage rule proposed by Miner, the treatment of cumulative fatigue damage has received increasingly more attention. As the result, more than 50 fatigue models have been proposed. These theories are grouped into six categories: linear damage rules, nonlinear damage curve and two-stage linearization approaches, life curve modification methods, approaches based on crack growth concepts, continuum damage mechanics models, and energy based theories. Though many damage models have been developed, none of them enjoys universal acceptance. Each damage model can only account for one or several phenomenological factors, such as load dependence, multiple damage stages, nonlinear damage evolution, load sequence and interaction effects, overload effects, small amplitude cycles below fatigue limit and mean stress. For example of fatigue damage and cumulative damage, Golos et al. [156] have presented the cumulative damage theory for multilevel cycle loading. This research is included both of the crack initiation and propagation stage, and the effect of the mean stress/strain on the damage accumulation. The results show that a number of earlier proposed models can be derived ad a particular of the present criterion. The predictions of the proposed damage accumulation criterion are compared with the experiment data for 2, 3, 5 and 6 steps cyclic loading as an example shown in Fig. 2-10, the comparison between calculated and experimental data of two stage test with the condition of N_f^H = 1000 and N_f^L = 2000. In addition, the results note that a good agreement between the predicted and experimental results. Tanegashima et al. [157] have studied the fatigue fracture mechanism in spot welded joints under constant, and variable force amplitude which included both of two-step and random force amplitude. In this study, three dimensional observations were made on the propagation behavior of fatigue cracks initiating at the edge of the slit. It was found that the fatigue limit of spot welded joints vanished under repeated two-step loading conditions. An evaluation method of the fatigue life was proposed for random loading conditions. Since the mean load obviously affected the fatigue life of the spot welded joints, the proposed evaluation method was applied to account for this load effect. The proposed evaluation method was satisfying the application range in the automobile industry. The results showed that this proposed method is suitable for practical applications.

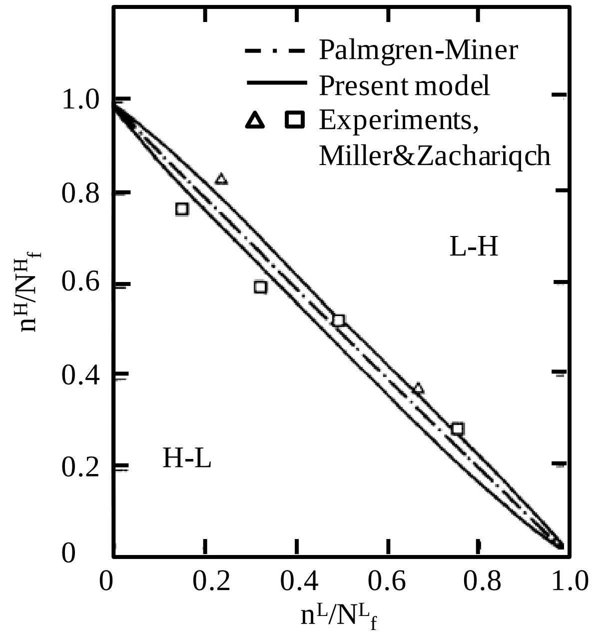

Fig. 2-10 the comparison between calculated and experimental data of two stage test with the condition of N_f^H = 1000 and N_f^L = 2000 [156].

During the last decade, many investigations have been carried out to develop prediction model as mention above. There are at least 50 models for fatigue damage and life prediction. However, none of which approach which has been generally accepted. Therefore, many researchers are still necessary to study the fatigue accumulation process. For example, Zheng et al. [158] have studied the fatigue accumulative processes, and Savadis et al. [159] analysis of an asymmetric circular cylinder with a circumferential notch subject to multi-axial non-propagation fatigue loading with variable amplitude. Moreover, many studies also studied the fatigue behavior under variable force amplitude.

Heuler et al. [160] have discussed a criterion for omission of variable amplitude loading history. This study results show that the crack initiation lives were longer when compares with the fatigue life under the unedited sequence. In addition, for letter two spectra, the crack propagation lives were longer by up to 90% with a detrimental influence of higher loading levels. Total live of notch aluminium is increased by 30-70% using a filter level of 50% of the material's fatigue limit. Stanzl et al. [161] has been investigated as a time and energy saving method for measuring the fatigue life under service loading conditions using ultrasound technique. The experimentally found lifetimes are compared with predictions according to Miner and the Miner-Haibach rule. Good agreement is found for measured and calculated results according to the Miner-Haibach rule. This agreement is especially good for Markov random loading. Predictions according to the original Miner's rule give lifetimes that are too long in the very high cycle range. This result is explained by damaging effects of amplitudes below the fatigue limit. Moreover, Beden et al. [154] proposed his research to assessment the fatigue life under variable amplitude loading. This paper presents a technique to predict the fatigue life of a shell structure of different materials with application of measured variable amplitude loading. The finite element analysis technique was being used for the modeling and simulation.

Fatigue damage has long been an important aspect of designing the component to perform a specific function. Engineers have to accurately predict the service performance of their components. Among others, fatigue life is one of the most important properties when designing such components and structure. The majority of structural components under actual conditions are subjected to random amplitude service loading, during their lives. However, the fatigue strength of alloys and components has conventionally been measured in laboratory, using constant amplitude tests. The fatigue lives for components subjected to variable amplitude loads can be quite below the fatigue life predicted using constant amplitude experiment results. Thus, determining the service life of a component can be quite complex due to variations in component geometry, materials, and load histories. The solution on this realistic problem requires assessment of these variable parameters by performing experiments under actual conditions. In the last decade, many studies [162]–[167] were proposed the fatigue damage of materials components and structures. Lim et al. [162] have discussed the fatigue damage and crack nucleation of polycrystalline copper at intermediate strain. Xiaohua et al. [163] have studies the low cycle fatigue (LCF) damage evolution of the engineering materials is studied by use of continuum damage mechanics (CDM) theory. Based on thermodynamics, on a continuum damage variable and on the effective stress concept, a continuum damage model of isotropic LCF is derived and is used to analyze the strain-controlled LCF damage evolution of steam turbine blade material 2Cr13 steel.

CHAPTER 3

Experimental methods

3.1 Introduction

The base material, shape and type of specimen, and experimental methods for all the experiments conducted in the present work are explained in this chapter. Experimental procedures of the hardness test, the static tensile test, the fatigue test under service loading, and strain measurement are also described.

3.2 Material and specimen

3.2.1 Material

The base material used in this study is AISI 1012 cold rolled-low carbon steel with the carbon content 0.12 wt%(Equivalent material to JIS G 3141 carbon steel in Japan industrial standards). Plate thickness is 0.8-mm. This type of steel is used in general applications, in particular in the manufacturing of automobile parts as roofs, fenders, hoods, quarters, oil pans and spring houses. Chemical composition and mechanical properties of this material were given in Table 3-1 and 3-2, respectively.

Table 3-1 Chemical composition of AISI 1012 (wt%).

C	Mn	P	S	Fe
0.12	0.50	0.04	0.045	Bal.

Table 3-2 Mechanical properties of AISI 1012.

0.2 YS	UTS	Elongation	Hardness
172 MPa	314 MPa	48 %	115 HV

3.2.2 Specimen and welding conditions

This study used the cross-tension specimen type with the welded area in the center of specimen. Figure 3-1(a) shows the shape and dimensions of the FSSW specimens after the steel sheet was machined into rectangular pieces measuring 150 mm in length, 50 mm in width, and 8.1 mm in punch diameter. As shown in Fig. 3-1(b), two rectangular steel plates were used to prepare the cross-tension FSSW specimens at the Joining and Welding Research Institute (JWRI), Osaka University. The two rectangular sheets were placed one on top of the other to form a cross shape and welded in the center of the overlapping square region. The FSSW tools were manufactured from tungsten carbide (WC) with a shoulder diameter of 12.0 mm, probe length of 1.0 mm, and diameter of 4.0 mm as shown in Fig.3-2. The welding conditions were given in Table 3-3. On completion the welding process, the peak temperature of the welded zone (approximately 973 K) could be achieved when welding in air condition with a force of 15.0 kN, rotational speed of 550 rpm, and weld holding time of 2 s. The welded region on the front side of upper sheet and rear side of lower sheet were indicated in Fig. 3-3 (a) and (b), respectively.

Table 3-3 Welding conditions.

Applied force	15 kN
Rotational speed	550 rpm
Tool holding time	2 s

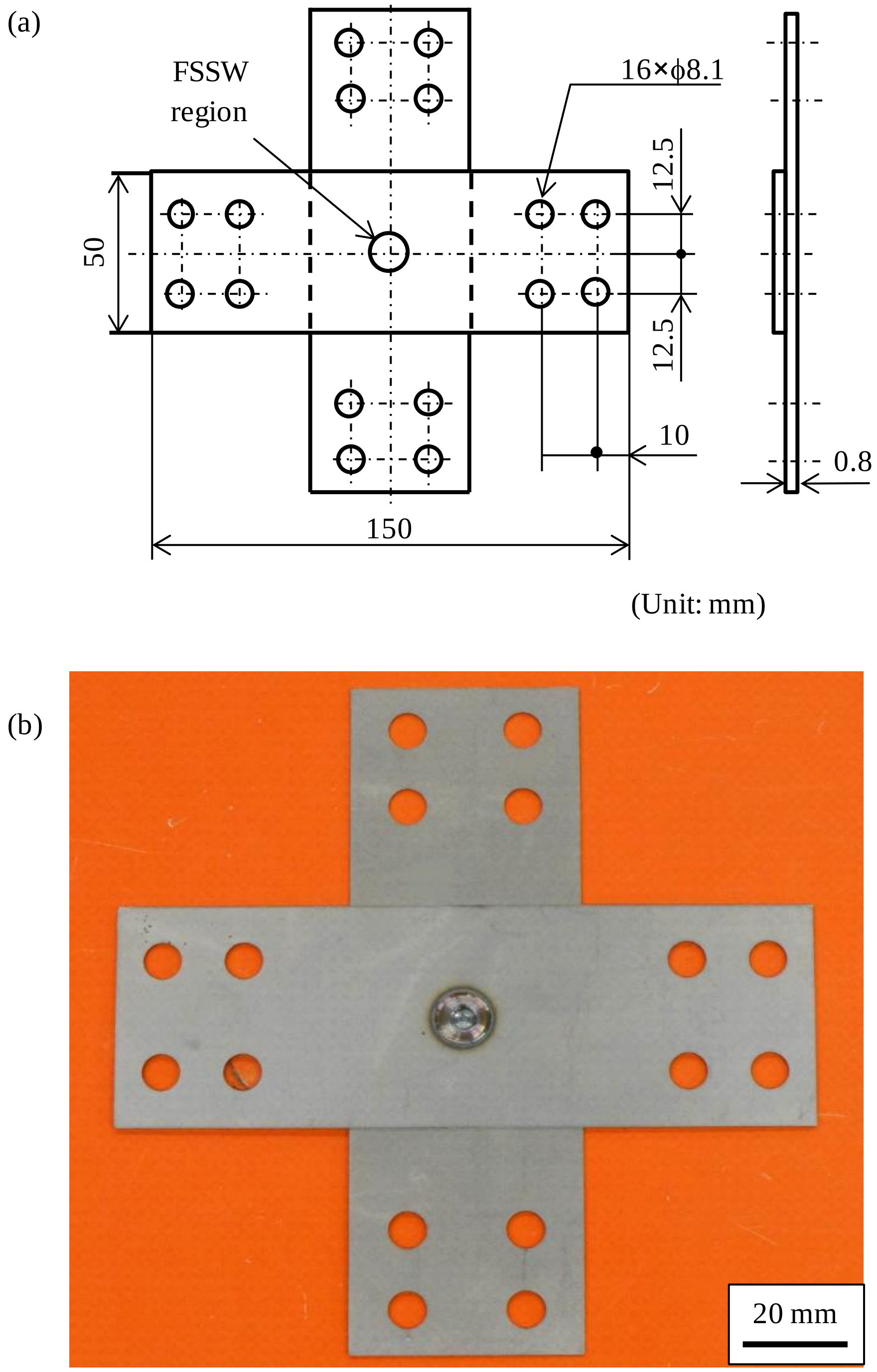

(Unit: mm)

Fig. 3-1 (a) Schematic illustration of shape and dimensions of specimen, (b) FSSW cross-tension specimen.

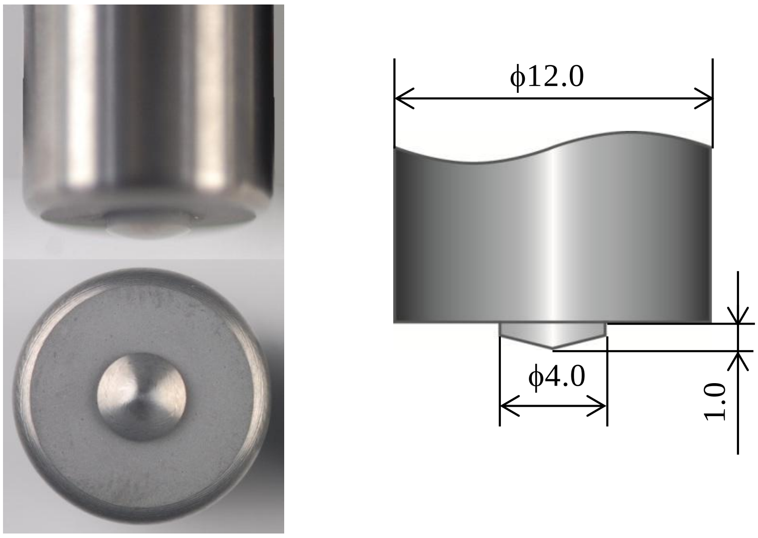

Fig. 3-2 Rotational tool for FSSW.

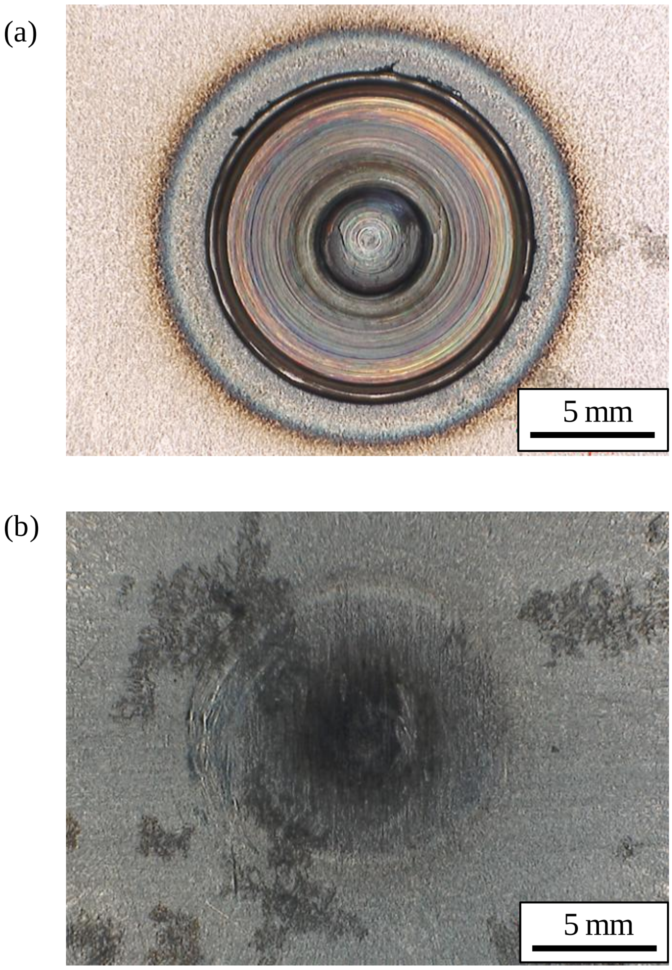

Fig. 3-3 The welded region: (a) The front side of upper sheet, (b) Rear side of lower sheet.

3.3 Experimental methods

3.3.1 Macro and microstructural observation

The metallurgical inspections were performed on a cross-section of the joint after polishing using emery paper and using polishing cloths for fine grinding with alumina powder until 0.1 µm in diameter, finally, the specimen was etched with 2% Nital (99.5% Ethanol mixed with 61% Nitric acid) for holding time 15-20 s. The specimen was investigated the macrostructrue and microstructure using the light microscope ZEISS Axio observer for material as shown in Fig. 3-4.

Fig. 3-4 The light microscope, ZEISS Axio observer for material.

3.3.2 Hardness test

The hardness test was performed on FSSW specimen using BUEHLER Vicker hardness testing machine as shown in Fig. 3-5. The Vickers hardness was measured in the cross-sectional area perpendicular to the FSSW tool direction. A force of 9.8 N was applied for 10 s with a Vickers indenter to examine the hardness distribution based on microstructure classification. The hardness survey location is illustrated in Fig. 3-6.

Fig. 3-5 The BUEHLER Vicker hardness testing machine.

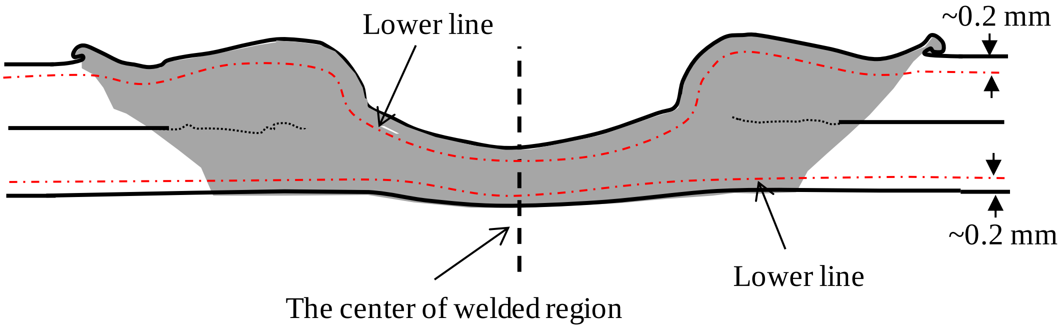

Fig. 3-6 Illustration of hardness survey on FSSW specimen.

3.3.3 Static tensile test and fatigue test

The static tensile test was carried out at room temperature by using the servo-hydraulic testing machine (SHIMADZU EHF-EV050K1-020-0A) at force speed 0.1 kN/s.

Fatigue tests were performed at room temperature with the servopulser testing machine, as shown in Fig. 3-7 (SHIMADZU EHF-FD5KN-4LA) operating at a sinusoidal wave frequency of 5–10 Hz at a force ratio R of approximately 0.01, (force ratio (stress ratio) is the ratio of maximum force (maximum stress) to minimum force (minimum stress) in one cycle loading of fatigue test). The specimen was set up in the machine with the upper and lower sheets clamped with rectangular jigs where the plates do not overlap, as shown in Fig. 3-8. The load was applied to the specimen in the direction perpendicular to the face of the plate. The failure criterion was specified as the point of complete separation of the FSSW joints between the upper and lower sheet. The fracture surface of the specimens after fatigue tests were observed by HITACHI S-3000N scanning electron microscope. The waveform for the constant force amplitude P_a, which mainly performed in Chapter 4, is shown in Fig. 3-9(a). Figure 3-9(b) shows the repeated two-step force amplitude waveform, which is composed of high and low force amplitudes, denoted by P_H and P_L, respectively. This waveform was generally used to investigate the fatigue damage evaluation in Chapter 5. And, Figure 3-9(c) is an example of random force amplitude wave form in Chapter 6, which is simulated using the stationary Gaussian random process.

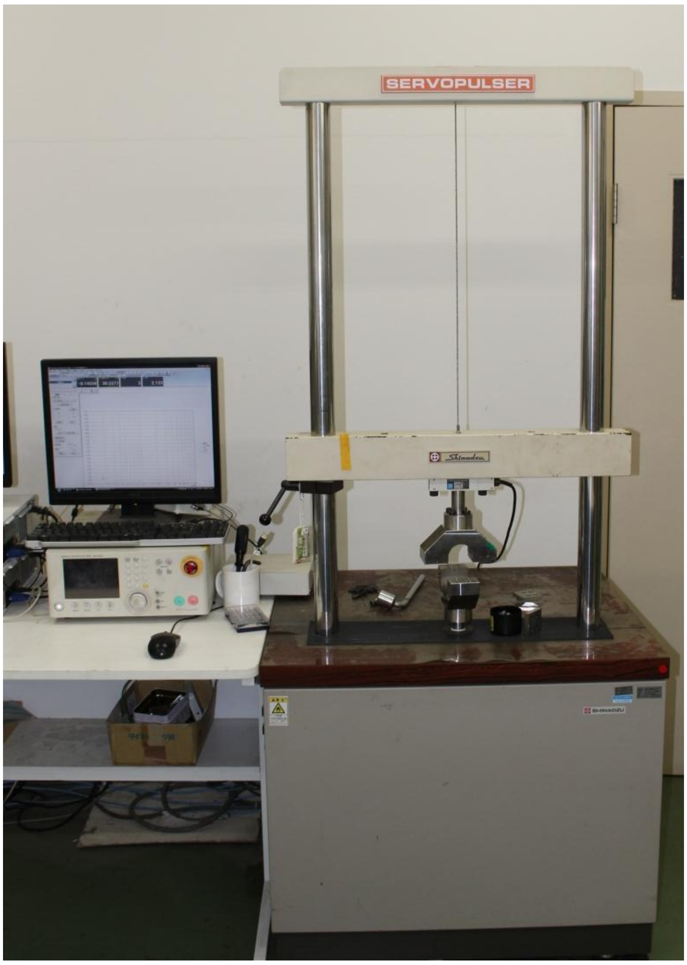

Fig. 3-7 The servopulser testing machine (Max. capacity 5 kN).

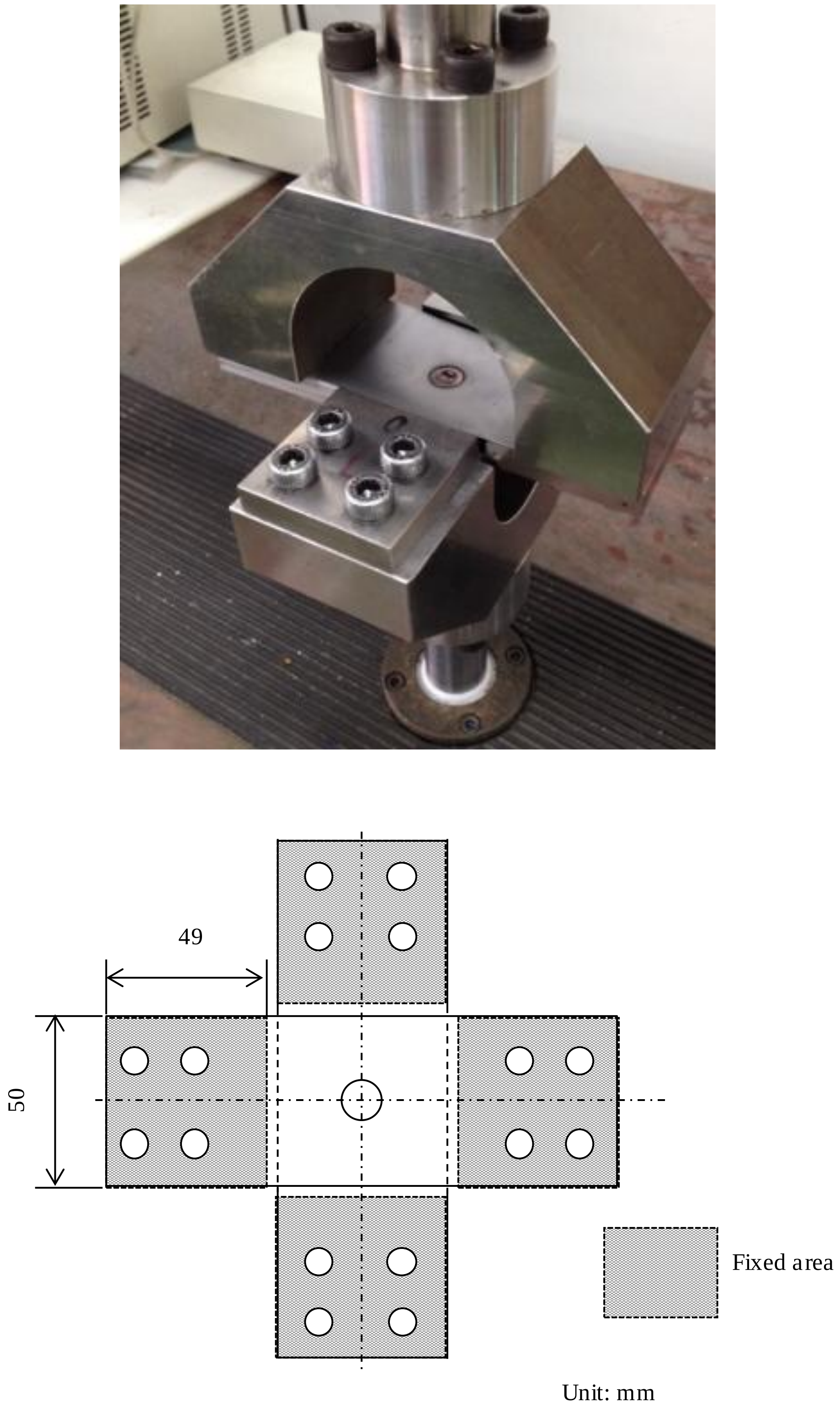

Fig. 3-8 Installed to testing machine.

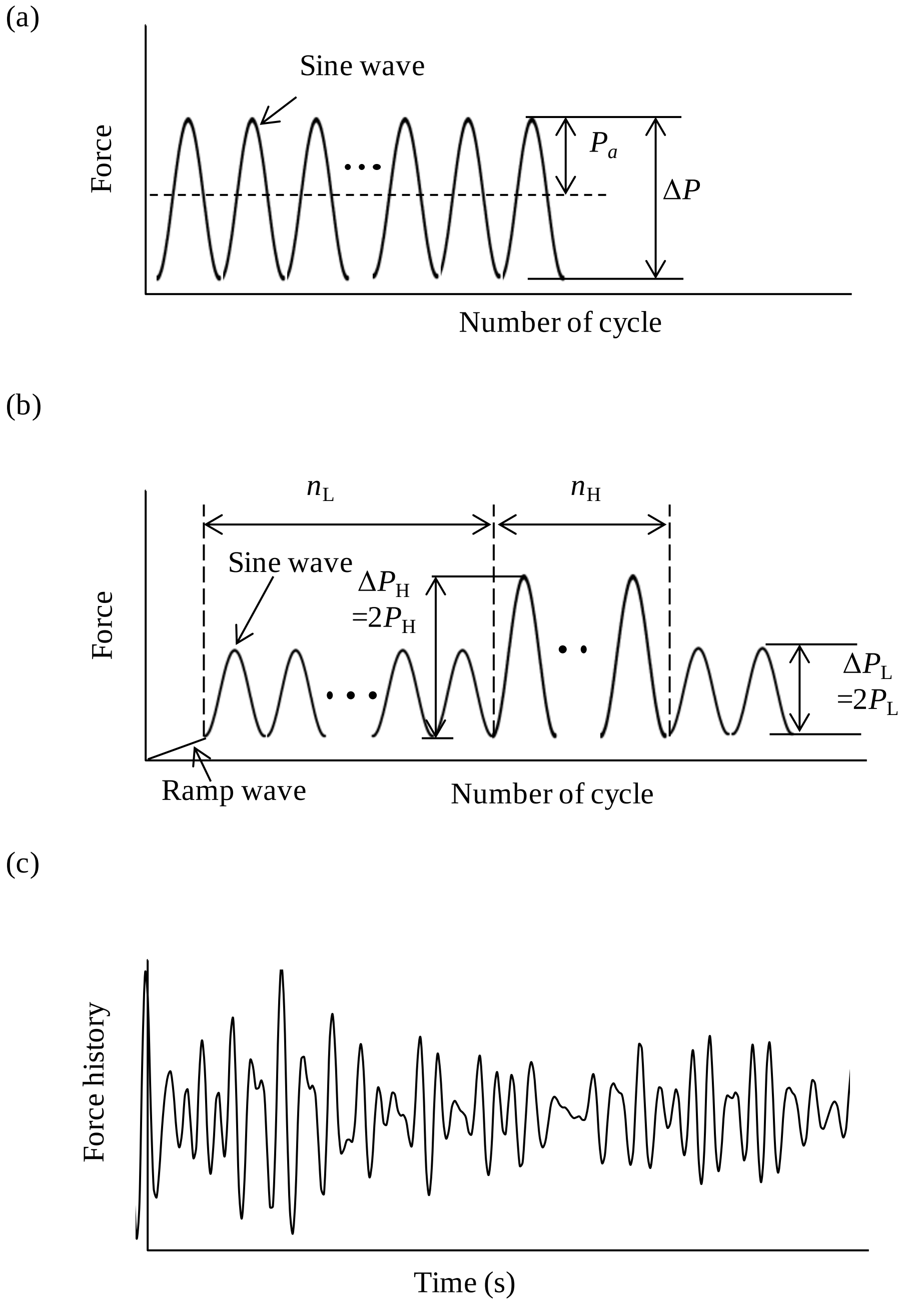

Fig. 3-9 Illustration of force amplitude wave form: (a) Constant force amplitude wave form, (b) Repeated two-step force amplitude wave form, (c) Random force amplitude history.

3.3.4 Strain measurement

The local strain behavior was measured during the fatigue test by considering strain behavior near the welded zone. The local strain was measured using strain measurement system KYOWA sensor interface PCD-300B, as shown in Fig. 3-10. The strain gage used in this study is KYOWA type KFG-2-120-C1-11. The specification of strain gage was given in Table 3-4. The Four strain gages were attached 9 mm from the center of the welded zone in the longitudinal direction on the front side of the upper sheet and the rear side of the lower sheet, as shown in Fig.3-11.

Fig. 3-10 Strain measurement devices (PCD300B).

Table 3-4 The specification of stain gage.

Strain gage type	KFG-2-120-C1-11
Gage factor (24 ^oC, 50%RH)	2.09 ± 1.0%
Gage length	2 mm
Gage resistance (24 ^oC, 50%RH)	120 ± 0.2 Ω

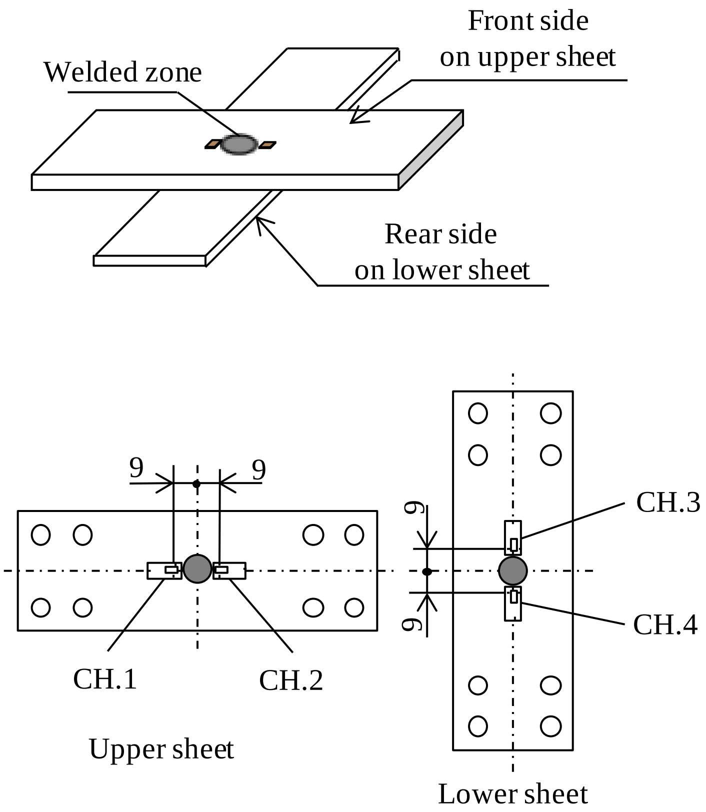

Fig. 3-11 Four strain gage locations on FSSW specimen.

CHAPTER 4

3-Dimensional observation of the interior fatigue fracture mechanism on friction stir spot welded cross-tension specimen

4.1 Introduction

Recently, automotive and aerospace industries have been manufacturing light weight, operational cost and environment friendly vehicles [25] by replacing iron based with light alloy and high strength materials, such as aluminum, copper, fiber reinforced polymer and carbon steel [34], [56] . Friction stir welding (FSW) developed and patented by The Welding Institute (TWI) in 1991, it serve a purpose to initially apply to aluminum and it alloys [122]. The basic concept of FSW is remarkably simple. A non-consumable rotating tool with a specially designed pin and shoulder is inserted into the abutting edges of sheets or plates to be joined and traversed along the line of join. And, friction stir spot welding (FSSW) is a relatively recent trend of joining carbon steel, that provides a superior alternative to resistant spot welding and riveting for fabricating automotive and railway body component. FSSW technique was invented by Kawasaki Heavy Industries Ltd. in 2000 as a variant of the linear friction stir welding (FSW) method [55], [85].

The FSSW studies correlate the mechanical properties and the parameters used to make the joint, aiming to find better parameter joins. The mechanical properties measured in most research are restricted to tensile tests [37], [168], however cross-tension tests have also been cited [169]. Regarding fatigue tests, some authors have performed studies in alloys series, determining fatigue lives, failure modes and microstructural analysis [63], [64]. Recently, FSW of carbon steel was studies. Several previous studies [53], [147] have reported the friction stir welding of carbon steels. However, there are few reports about fatigue properties and crack growth behavior of friction stir spot welded carbon steel, especially on cross tension FSSW specimen. In this study, we have investigate the fatigue properties and crack growth behavior of friction stir spot welded 300 MPa-class low carbon steel sheets used as the general automobile steels. Furthermore, fatigue crack initiation and fatigue crack propagation were observed by using the three-dimensional observation.

4.2 Experimental results and discussions

4.2.1 Microstructure classification and structural observation

The microstructure of the cross section of the welded area was observed using an optical microscope. The welded area was divided into four primary regions, as indicated in Fig. 4-1. BM represents the base metal, which was unaffected by heat and deformation. HAZ presents the heat-affected zone which was affected by heat only with the largest area on the welded joint. TMAZ represents the recrystallized structure, termed the thermomechanically affected zone which was affected by both heat and deformation. The TMAZ was small area, corresponding to the width of the shoulder on the upper surface and to the probe diameter at the root. The recrystallized structure was within SZ, termed the stir zone, which corresponded to the smallest area of the probe diameter. Figure 4-2 shows the microstructures of the four zones on the welded joint. The results show that the base metal and the HAZ contain ferrite in their band structures. The welded zones (the SZ and TMAZ) had a fine ferrite-pearlite dual-phase structure, resulting from the prevention of martensite formation. Therefore, the microstructures can be explained in terms of the peak temperatures of the welding process, which is below the A_1 point (eutectic temperature) on the Fe–Fe_3C phase diagram, as shown in Fig. 4-3 [68]. Additionally, the FSSW specimen was tested without inducing a phase transformation [69].

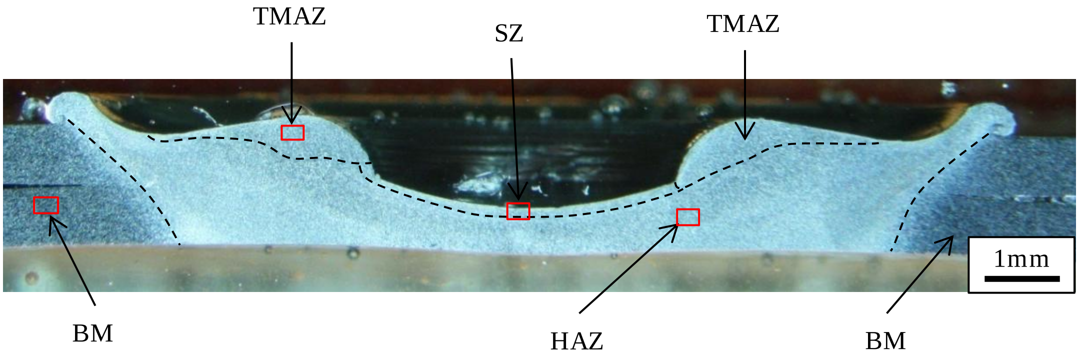

Area of each zones; TMAZ=1.9 mm^2, SZ=0.7 mm^2, HAZ=11.0 mm^2

Fig. 4-1 Optical microscopic image showing the cross-sectional macrostructure of the welded zone.

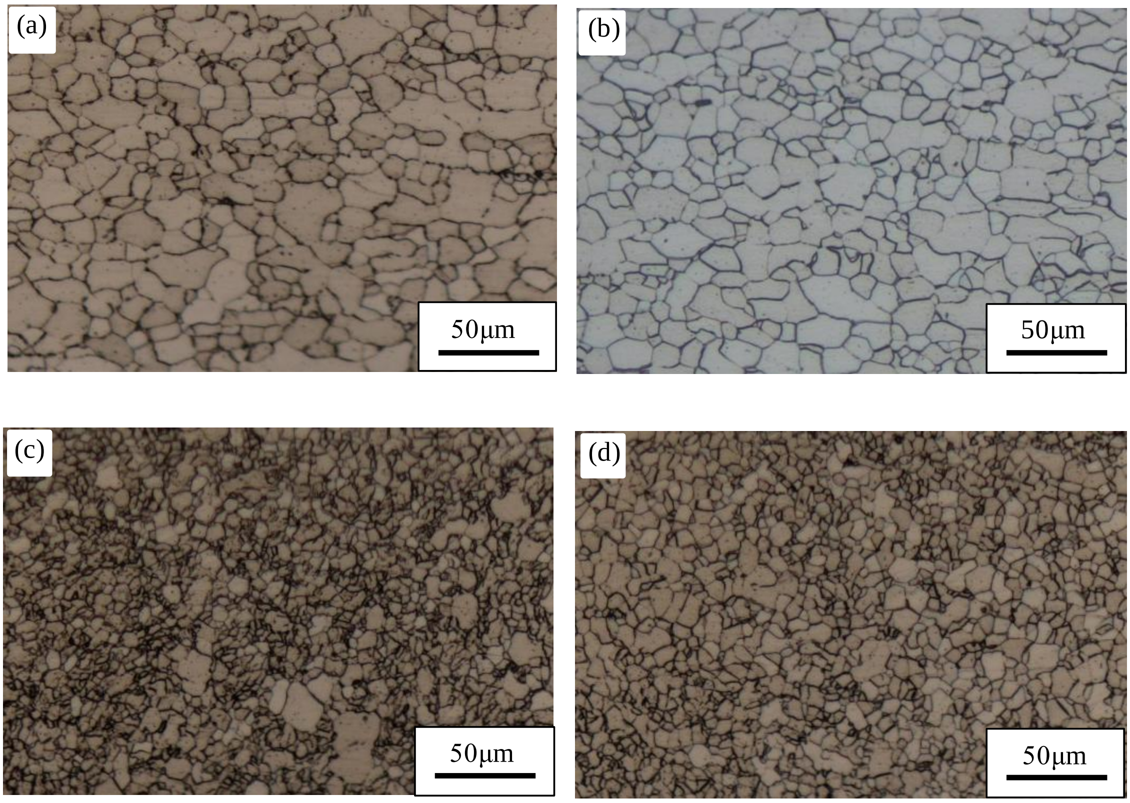

Fig. 4-2 Optical microscopic image showing the cross-sectional microstructure of 4 zones on the welded joint in Fig. 4-1: (a) Base metal, (b) HAZ, (c) TMAZ, (d) SZ.

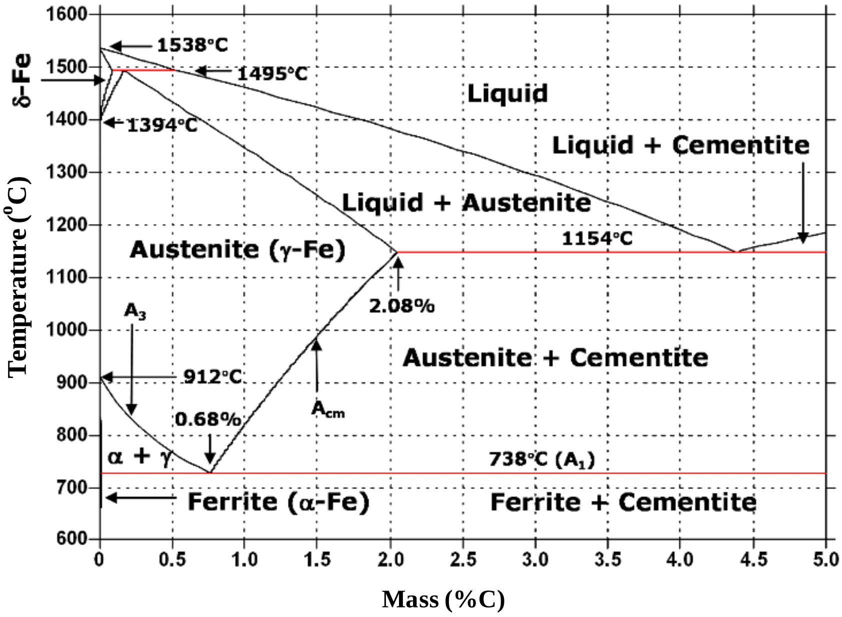

Fig. 4-3 Fe-Fe_3C phase diagram.

4.2.2 Hardness results

Figure 4-4 shows the horizontal micro-Vickers hardness profile for the two measurement lines of the welded area's cross-section. The hardness of the welded area was typically 160–180 HV, which is higher than that of the base metal at approximately 105 HV, as shown in Fig. 4-5. Therefore, hardening occurred up to 60% relative to the base metal. This was caused by the generation of extremely fine grains and pearlite phase structure in the SZ and TMAZ, and the impulse compressive force from the welding process.

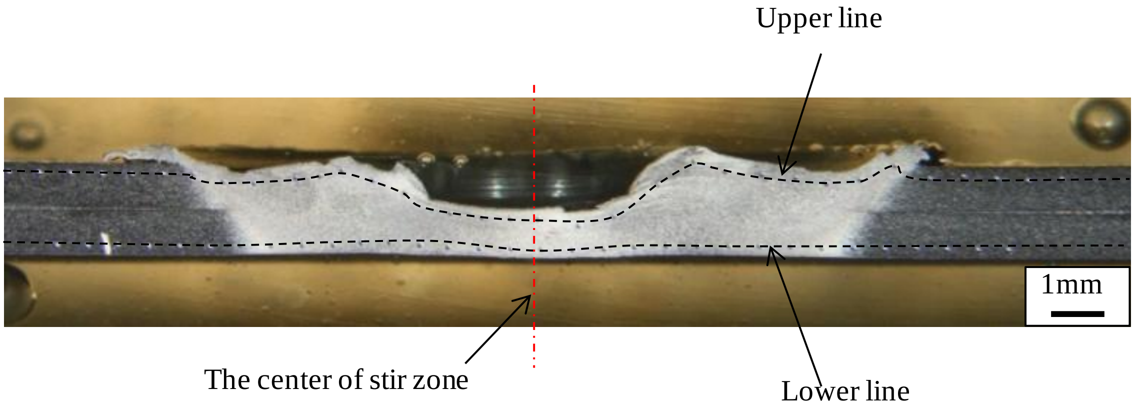

Fig. 4-4 The hardness survey locations of the welded area's cross-section.

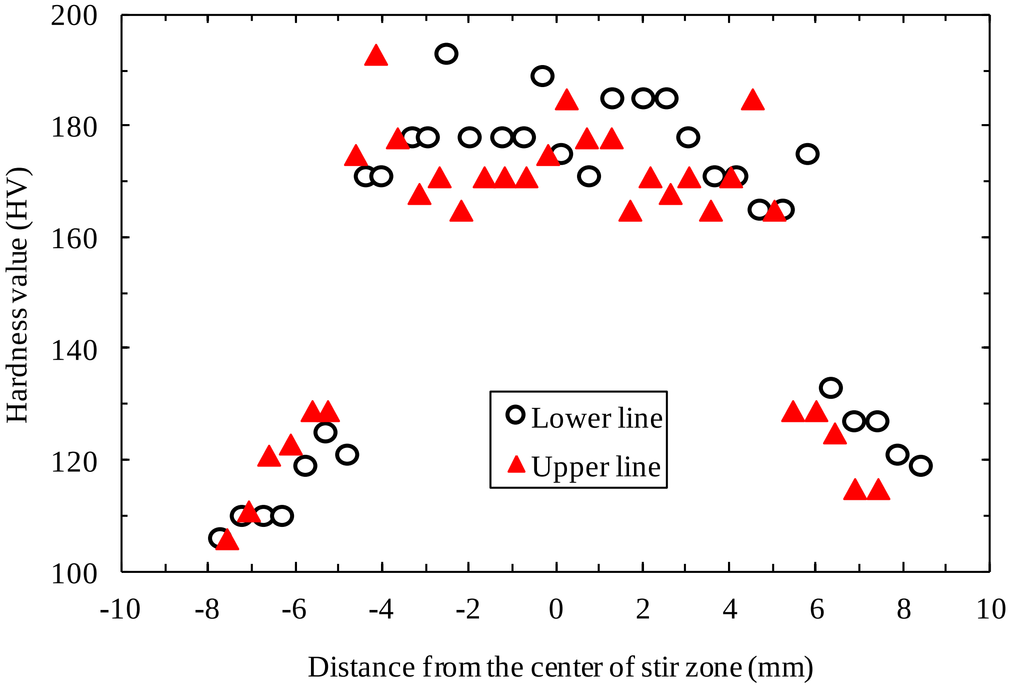

Fig. 4-5 Result of Vickers hardness test.

4.2.3 Static tensile test results

The result of tensile test for the welded joints is shown in Fig. 4-6. The tensile test specimen was used in this study do not have uniform cross sectional area. The maximum tensile force is approximately 8 kN. The welding joint fractured at the region between base metal and HAZ around the diameter of shoulder of FSSW tool on the upper sheet which is called the button fracture, as shows in Fig. 4-7.

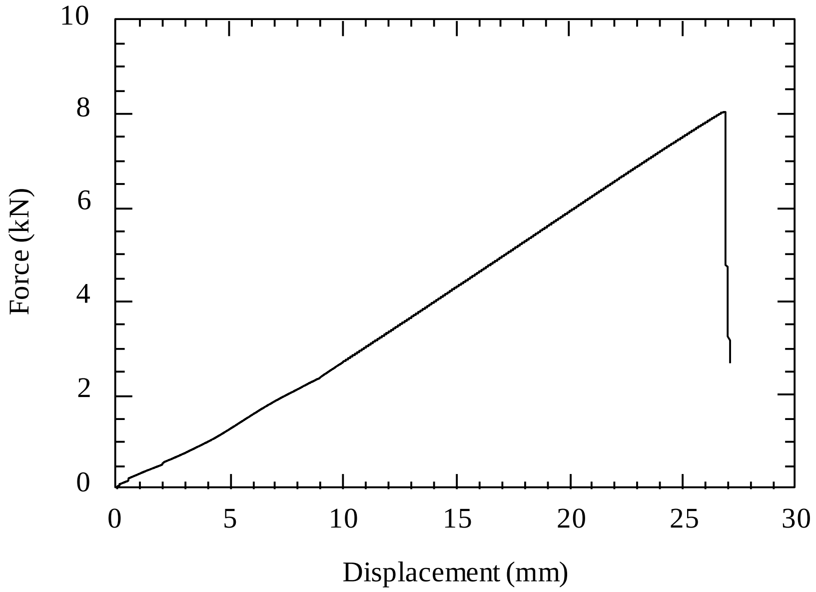

Fig. 4-6 Force-displacement curve of FSSW.

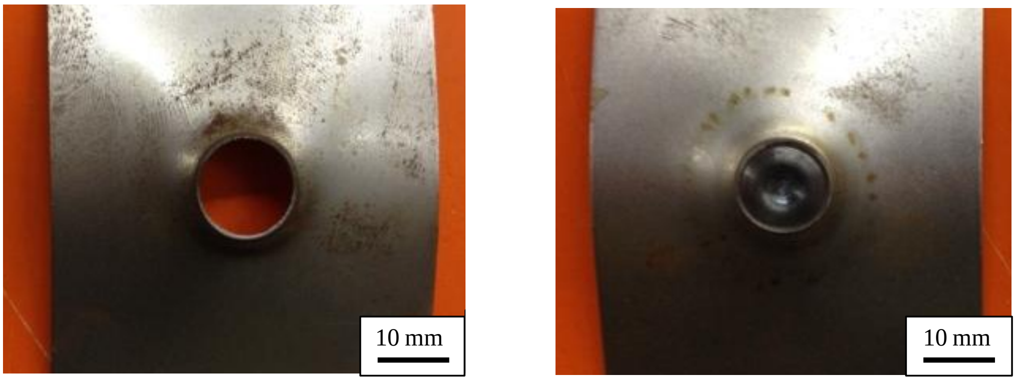

Upper sheet

Lower sheet

Fig. 4-7 The fracture of welded joint after tensile test.

4.2.4 Fatigue test results

4.2.4.1 *P-N* curve

Fatigue test results under constant force amplitude are shown in Fig. 4-8 as a plot of the force amplitude versus the number of cycles to failure. The fatigue limit of the welded joint was obtained by the JSMS standard “Standard Evaluation Method of Fatigue Reliability for Metallic Materials: Standard Regression Method of *S*–*N* Curves”. The results show that the specimen had a fatigue limit of approximately 0.11 kN. The FSSW joints can be seen to possess significantly lower fatigue resistance, as their fatigue limit was very low compared to the static strength of the welded joint (approximately 8 kN), as mentioned above.

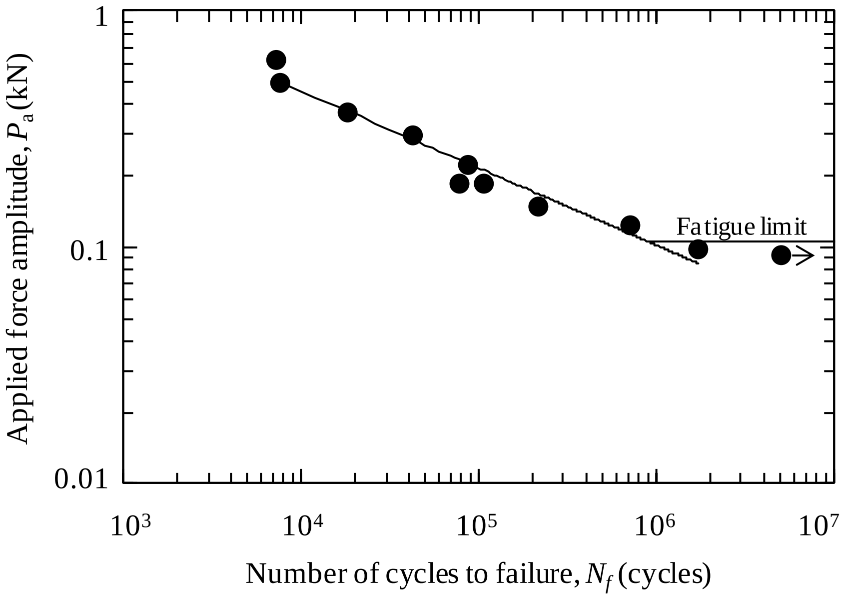

Fig. 4-8 *P-N* curve.

4.2.4.2 Fracture surface observation

From the *P-N* curve, fractures of the specimen from the fatigue test were observed. The macroscopic observation of the fractured specimens near the welded zone were conducted to 2 level of force amplitude which were conducted under constant low and high force amplitude P_a of 0.19 and 0.50 kN amplitudes, respectively. The micrographs were performed on a cross-section of the welded joints after fracture from fatigue test using scanning electron microscope (SEM).

The fractured specimen was then observed macroscopically. Figure 4-9 shows a schematic of the FSSW specimen, along with the loading direction in the *x–y–z* coordinate system. The macroscopic were observed on 2 sides on the front side of the upper sheet and rear side of the lower sheet.

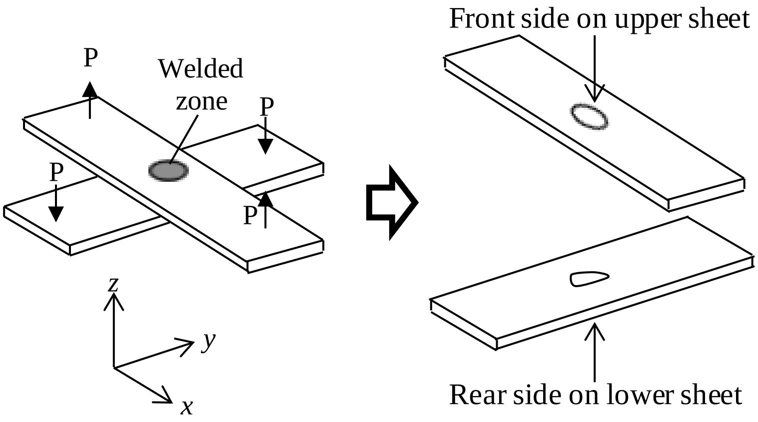

Fig. 4-9 Schematic illustration of the FSSW specimen with *x-y-z* direction incorporated with loading direction.

Typical fracture morphology fractured specimen near the welded joint at the low force amplitude of 0.19 kN was shown in Fig. 4-10. The results show that the fatigue crack of upper sheet propagated around the welded spot or as equal to a diameter of shoulder of FSSW tool, and then, propagated to the base metal until the specimen was broken as same as the lower sheet.

That is the intermingled fracture type of welded joint and base metal fracture morphologies which referred to this fracture morphology as the mixed mode fracture, which was including metal fracture and welded fracture.

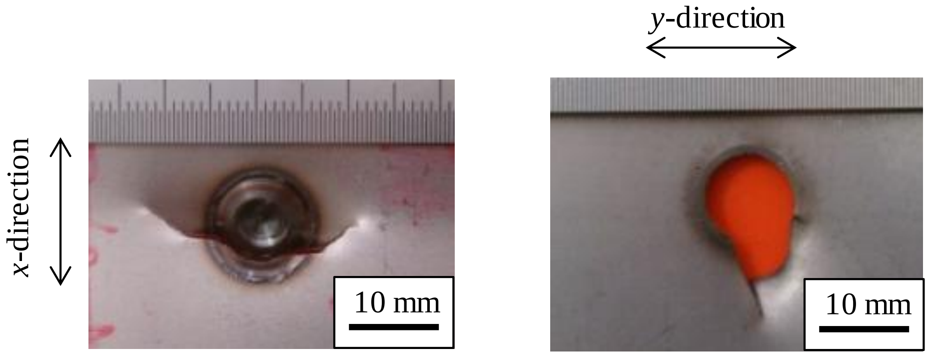

Front side of upper sheet

Rear side of lower sheet

Fig. 4-10 Fracture morphologies of FSSW under constant low force amplitude (P_a = 0.19 kN).

Microscopic observation of the fracture surface of fatigue test under constant low force amplitude (P_a = 0.19 kN) was carried out using the scanning electron microscope (SEM) on the fracture surface of upper sheet and lower sheet which are shown in the Figs. 4-11 and 4-12, respectively. Figure 4-11 shows the fracture surface observation of the upper sheet. In the fracture surface, the region has been divided into 4 parts, as shown in Fig. 4-11(a). The chipped vertical fracture surface can be seen in Area 1 and Area 3. The fatigue crack propagation area on fracture surface is about a half of sheet thickness on the bottom. On the top-half of sheet thickness, the fracture surface was worn during the test, as in the Area 2. Further, the dimple surface was observed in Area 4 and hence, the static fracture was occurred at this area.

Figure 4-12 shows the fracture surface observation of the lower sheet. Fig. 4-12(a) represents a schematic of two dimension diagram of the lower sheet. The depth direction of paper is corresponds to the direction of amplitude loading during the fatigue test. The chipped vertical fracture surface can be investigated in Area A and C. The ripples areas are due to fatigue crack propagate and wear was observed in Area B. Area D, E and F have showed the same fracture surface as on Area A, B and C, respectively.

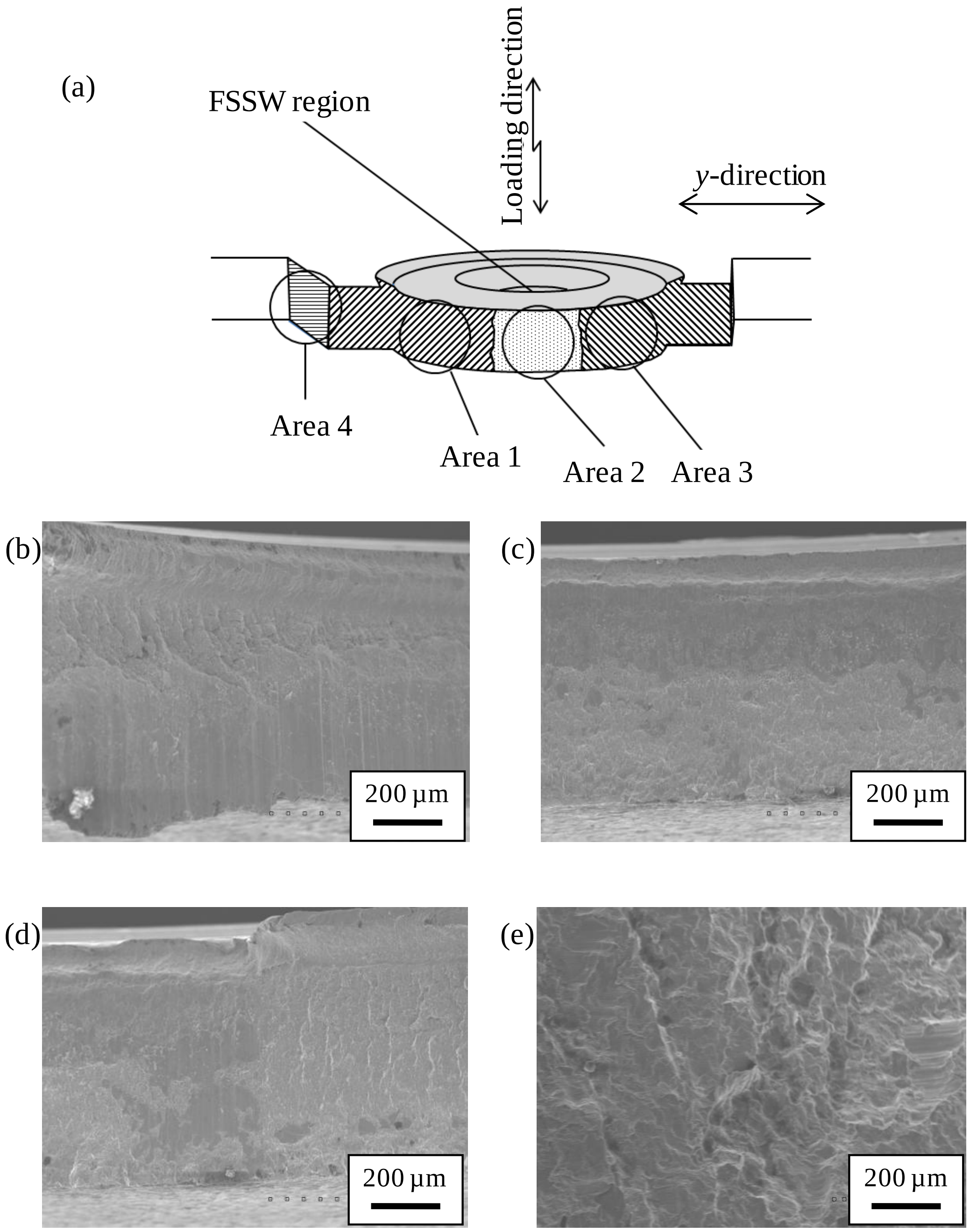

Fig. 4-11 SEM micrograph of fracture surface on upper sheet of fatigue test under low force amplitude level (P_a = 0.19 kN): (a) Schematic diagram of fracture surface of FSSW on upper sheet, (b)-(e) Micrographs of Area 1-4, respectively.

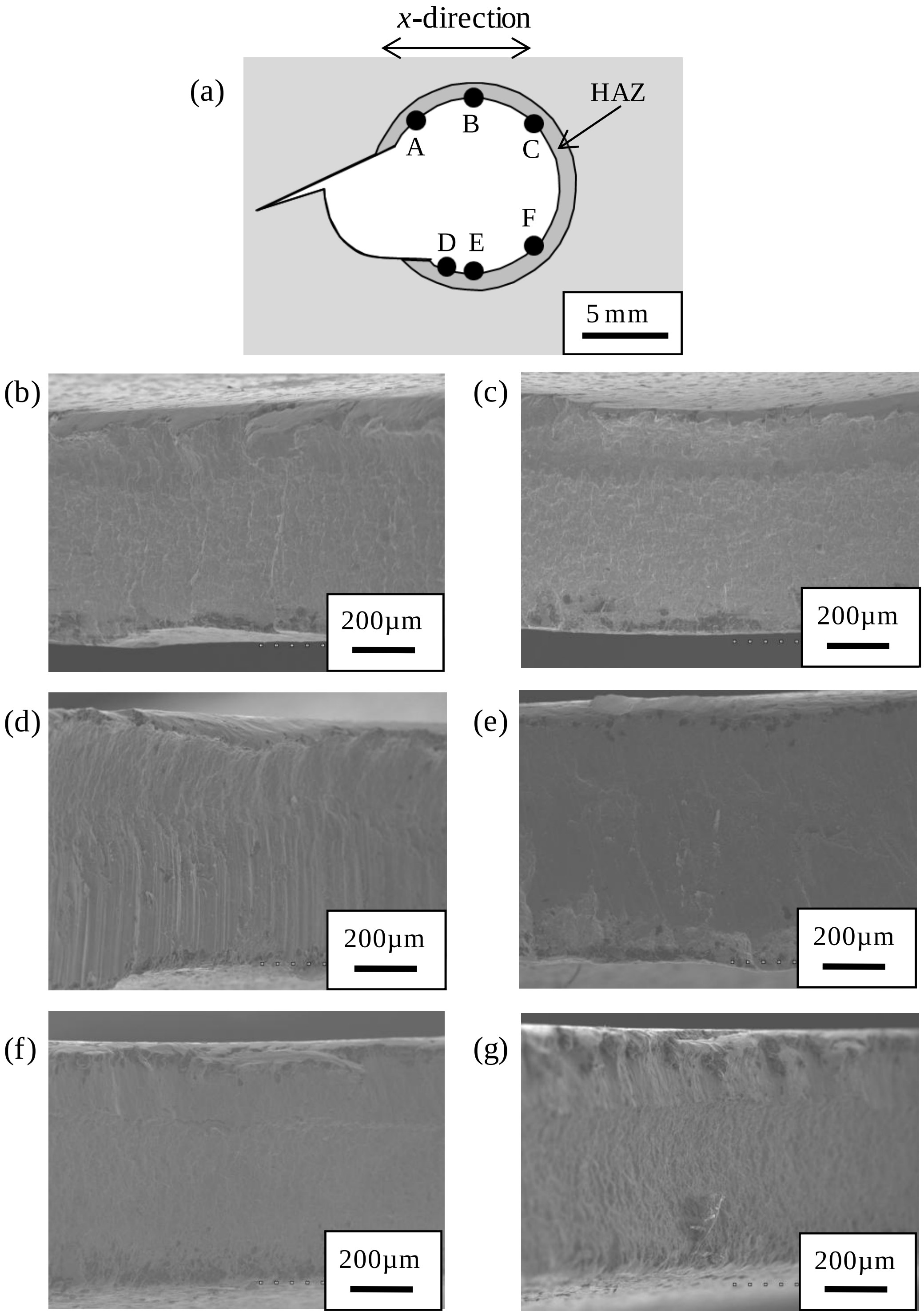

Fig. 4-12 SEM micrograph of fracture surface on lower sheet under low force amplitude level (P_a = 0.19 kN): (a) Schematic diagram of fracture surface of FSSW on lower sheet, (b)-(g) Micrographs of area A-F, respectively.

Typical fracture morphology fractured specimen near the weld joint at the high force amplitude of 0.50 kN is shown in Fig. 4-13. In addition, observational locations of fractured specimen were shown in Fig. 4-9. In the high force amplitude level, the fatigue crack of upper sheet propagated around the welded spot or the diameter of shoulder of FSSW tool approximately 25% of the diameter, and further it propagate to the base metal until the specimen was broken. The fatigue crack of lower sheet propagated around the diameter of shoulder of FSSW tool and propagated to base metal. That is the intermingled fracture type of welded joint and base metal fracture morphologies which referred to this fracture morphology as the mixed mode fracture, which was including metal fracture and welded fracture.

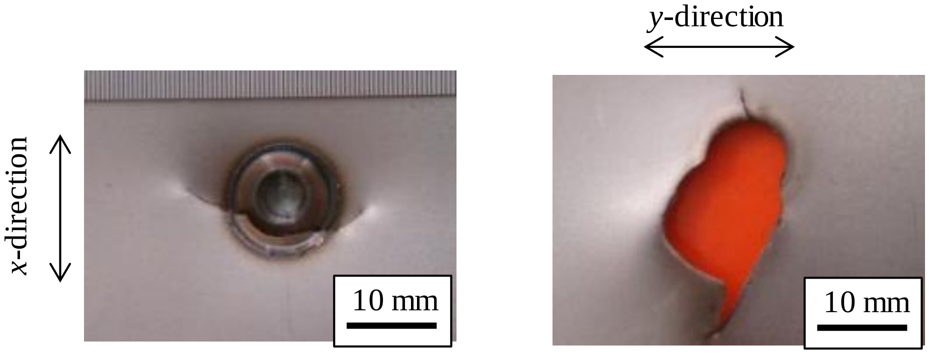

Front side of upper sheet

Rear side of lower sheet

Fig. 4-13 Fracture morphologies of FSSW under constant high force amplitude

(P_a = 0.50 kN).

Microscopic observation of the fracture surface of fatigue test under constant high force amplitude (P_a = 0.50 kN) was carried out using the scanning electron microscope (SEM) on the fracture of upper sheet and lower sheet as showed in Figs. 4-14 and 4-15, respectively. Figure 4-14 shows the fracture surface observation of the upper sheet. In the fracture surface, the region has divided into 4 shown in Fig. 4-14(a). The chipped vertical fracture surface can be seen in Area 1. In the Area 2, the fatigue crack propagation area on fracture surface is about a half of sheet thickness from the bottom. On a half of sheet thickness from the top, the fracture surface was worn during cyclic loading. The chipped vertical fracture surface and a part of static fracture are shown in Area 3. This area was changed from fatigue fracture to static fracture. Further, the dimple surface was observed in Area 4 and hence, the static fracture was occurred at this area.

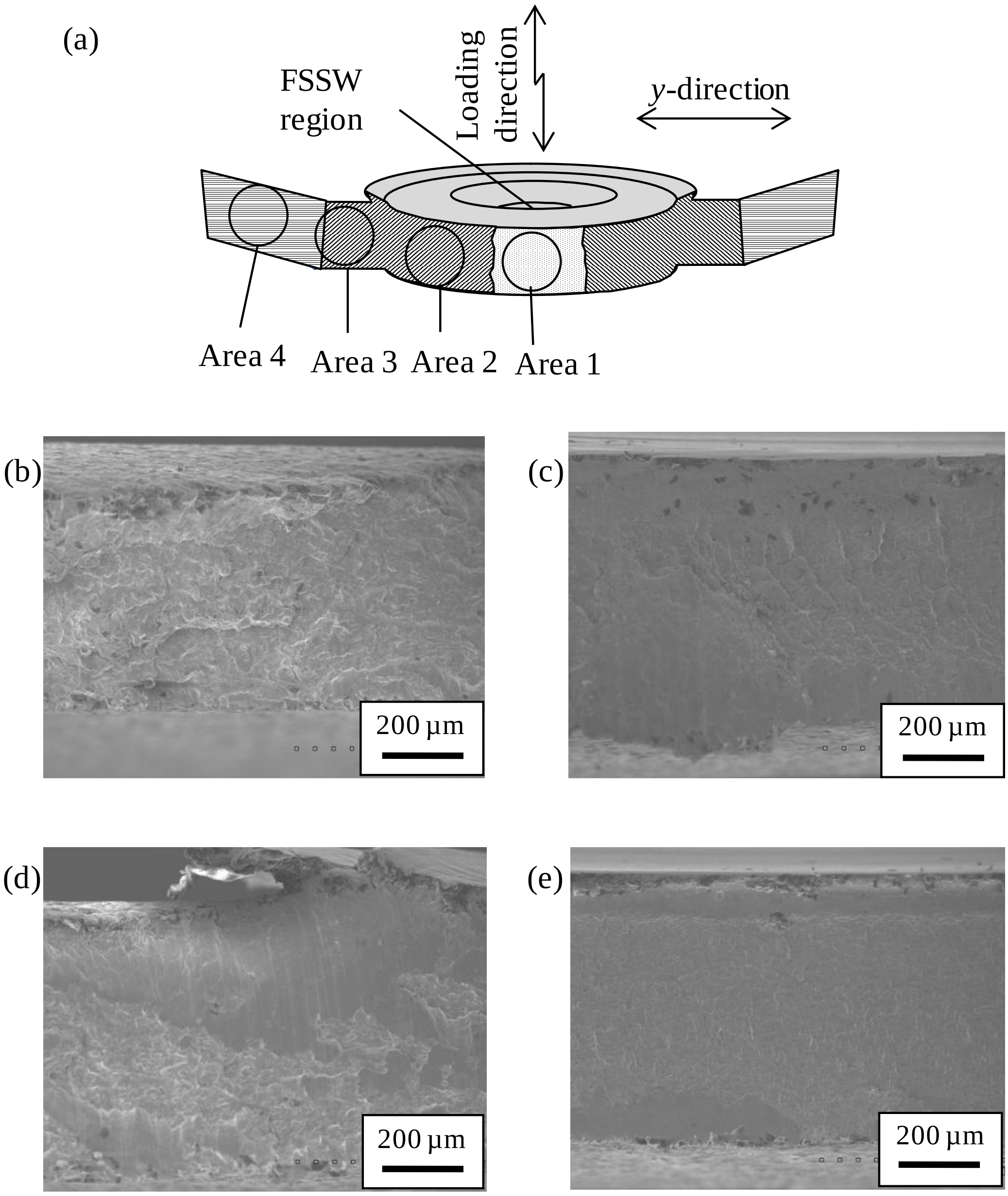

Fig. 4-14 SEM micrograph of fracture surface on upper sheet under high force amplitude level (P_a = 0.50 kN): (a) Schematic diagram of fracture surface of FSSW on upper sheet, (b)-(e) Micrographs of area 1-4, respectively.

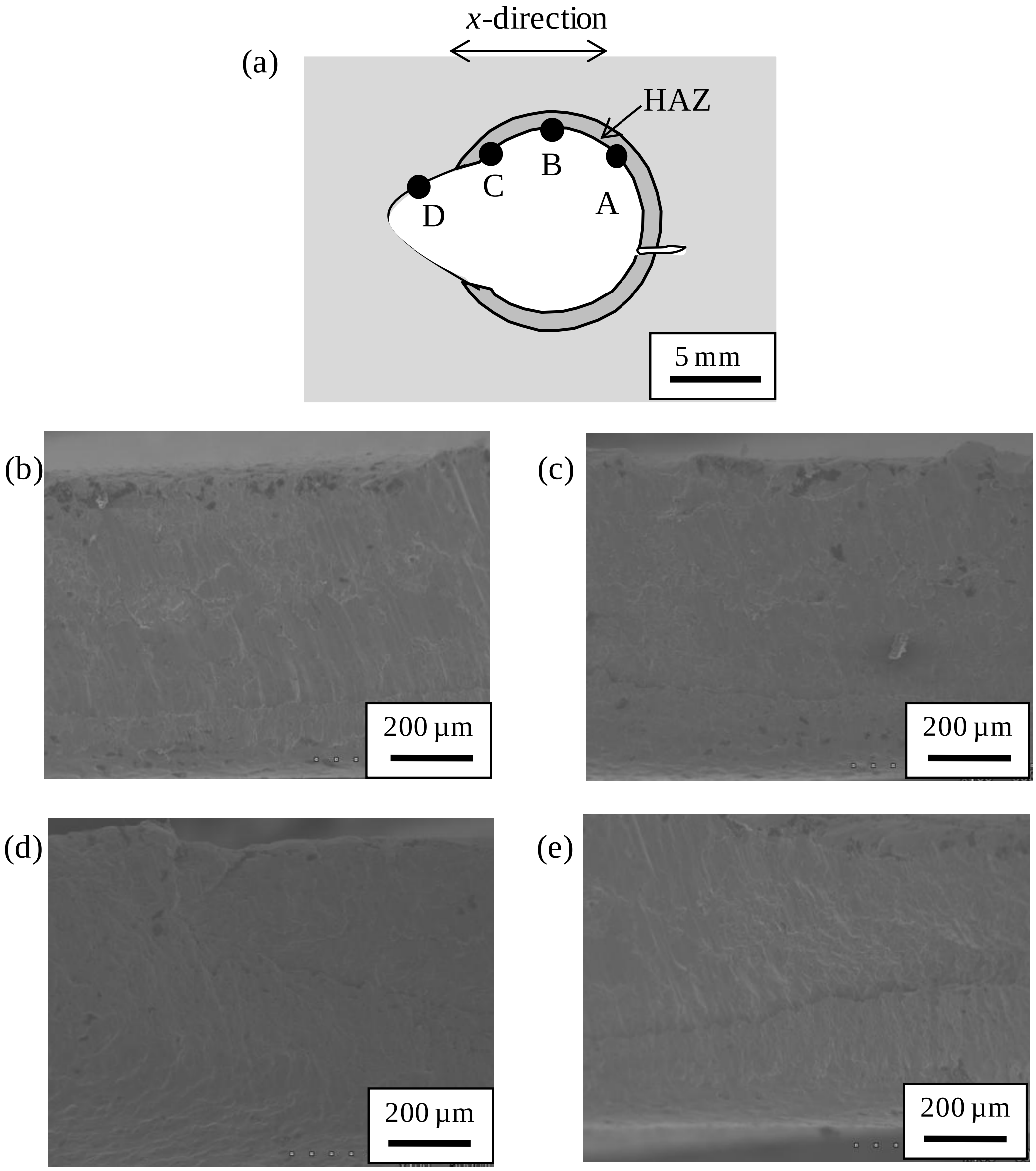

Fig. 4-15 SEM micrograph of fracture surface on lower sheet under high force amplitude level (P_a = 0.50 kN): (a) Schematic diagram of fracture surface of FSSW on upper sheet, (b)-(e) Micrographs of area A-D, respectively.

Figure 4-15 shows the fracture surface observation of the lower sheet. Figure 4-15(a) represents a schematic of two dimension diagram of the lower sheet. The depth direction of paper corresponds to the direction of force amplitude during the fatigue test. The chipped vertical fracture surface can be investigated in Area A, B and C. The ripples areas were occurred from fatigue crack propagation and wear was observed in this area. The static fracture was occurred in Area D until the specimen was broken.

The fracture mode with the high force amplitude was observed to be similar to that with the low force amplitude. The fatigue crack of the upper sheet first propagated around the welded zone and then propagated further into the base metal until the specimen was broken. The fatigue crack in the lower sheet propagated similarly. This means that the fracture mode of high force amplitude level is similar to low force amplitude level. However, when it come to the crack length propagated towards the base metal until specimens fractured, high force amplitude level increase the length more than that of the low force amplitude level.

4.2.4.3 Fatigue crack initiation site

In order to specify the crack initiation site, the cross section of the welded joint was fatigued under the constant low force amplitude P_a = 0.19 kN and interrupted before the final fracture was observed by an optical microscope. The interrupted cycle N_{stop} was 6.4×10^4 cycles, and the complete fatigue life N_f was 9.5×10^4 cycles (N_{stop}/N_f was approximately 67%). The observation results were shown in Fig. 4-16.

The crack was observed to initiate at the boundary between the edge of the welding interface zone and the noninterface zone, which is located in the HAZ. The fatigue crack on the upper sheet was found to start at the distal slit and continue to the surface of the sheet up to the concave zone. In addition, we confirmed that the crack initiation sites of all welded joints were the same, irrespective of the force amplitude level.

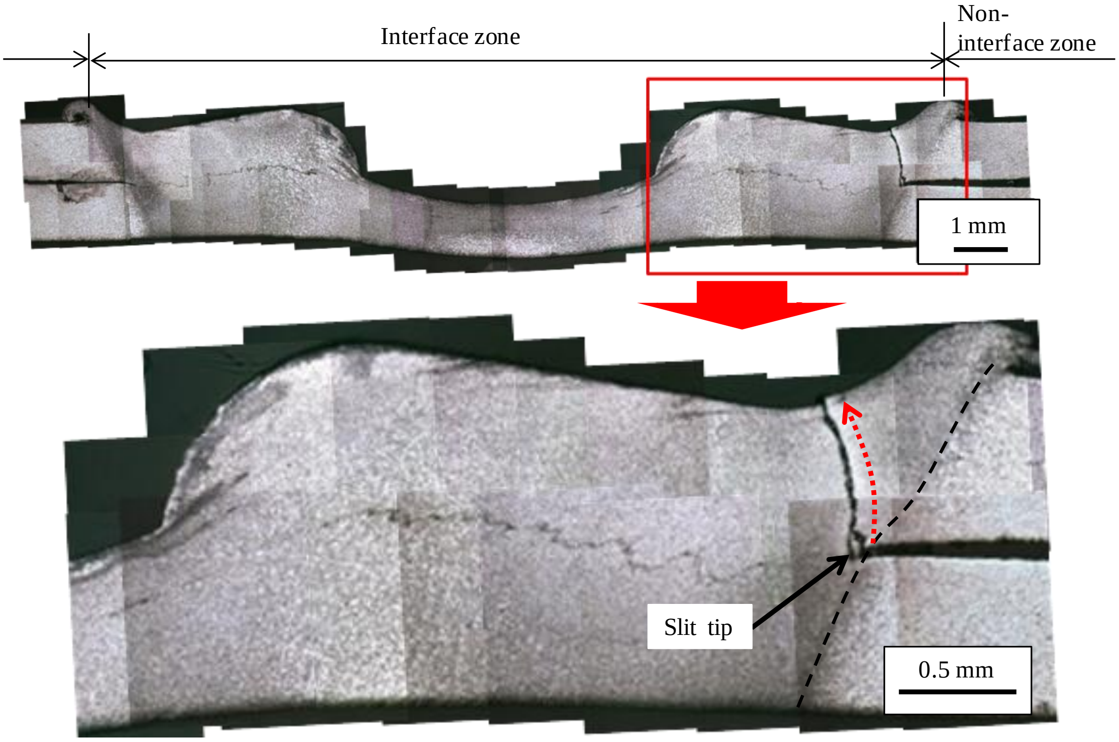

Fig. 4-16 Macrograph of cross-sectional welded zone under constant low force amplitude (P_a = 0.19 kN and stop at number of cycle, $N_{stop} = 6.4 \text{x} 10^4$ cycles.

These observations revealed that the microstructure near the welded zone hardly affected the fatigue crack initiation and propagation behavior, because the fatigue crack initiated at the slit tip which is located in HAZ regardless of the microstructure.

4.2.5 3-dimensional observation fatigue crack propagation

According to the result of *P-N* curve of the FSSWed AISI 1012 cold rolled-steel, 3-dimensional observation of the fatigue crack propagation was conducted under the constant low and high force amplitude level of 0.19 and 0.50 kN in the mixed mode fracture, respectively. The fatigue tests were conducted at $1x10^5$ cycles for low force amplitude level and $1x10^4$ cycles for high force amplitude level, which is the longest fracture life in each the stress level.

This research mainly investigates about the fatigue crack propagation conducting in the macro and microscopic observation of the fracture surface. Throughout analysis, the fatigue crack initiation and propagation should be observed three-dimensionally for the detailed consideration, because their behavior appeared at the interface between two thin steels sheet. Therefore, we carried out the three-dimensional observation of the small fatigue crack initiated on FSSW using the following procedure as shown in Fig. 4-17. At first, the specimen was cut out so that the area included welded joint, after the fatigue test was interrupted at the x% cyclic number for the whole fracture life called as N/N_f. We obtained an observed result at the cross section using the optical microscope after specimen was polished and etched. The specimen was polished in each step by approximately 100-300 μm towards the width direction, observation image was taken using the same procedure mentioned above. Using about 30-100 observation images taken at the cross section a specimen up to the $\%N/N_f$, the three-dimensional fatigue crack propagation was produced by the three-dimensional graphics software.

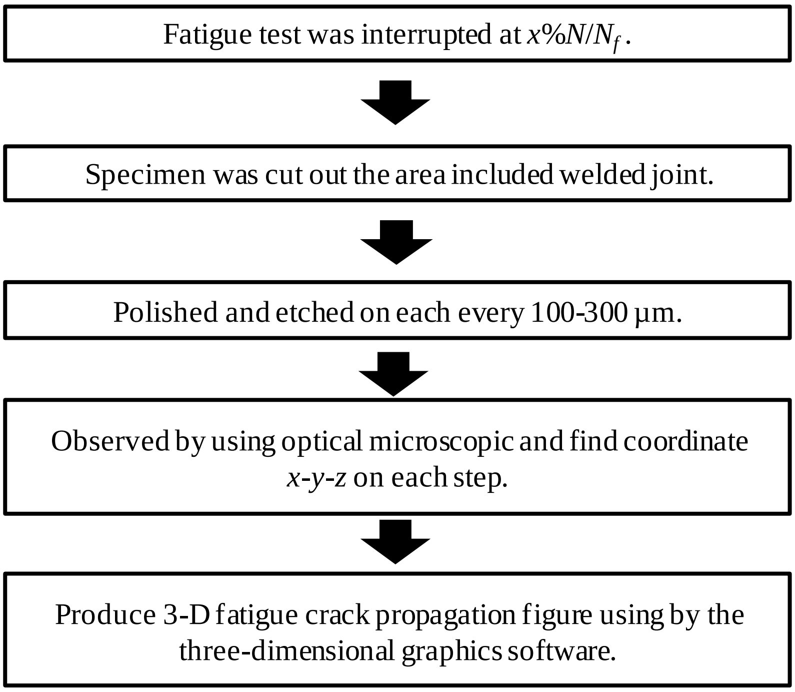

Fig. 4-17 3-dimensional observation procedure.

4.2.5.1 Low force amplitude level

Figure 4-18 shows the fatigue crack propagation behavior under constant low force amplitude. Figure 4-18(a) shows the schematic illustration the FSSW specimen with *x*-*y*-*z* direction and loading direction. On 61.5%N/N_f, fatigue crack propagated toward thickness direction of upper and lower sheets. Moreover, there was no fatigue crack near the welded on 55.9%N/N_f. This fact implies that specimen used in this study requires many cyclic loading to initiate the fatigue crack in the low force amplitude level. Figures 4-18(c) and (d) shown that the fatigue cracks grow to the full thickness of upper and lower sheet, and that the fatigue cracks tend to grow around the welded joint as equal to the diameter of shoulder of FSSW tool. Finally, on 83.3%N/N_f the fatigue crack propagation of upper sheet grows to the both side of base metal, and two sides of fatigue crack propagation of lower sheet come across nearly circular and propagated to base metal. After the initiation, as the number of cyclic increases, the fatigue crack grew gradually the thickness direction. It is likely for the fatigue crack propagate from the center of spot welded toward loading direction.

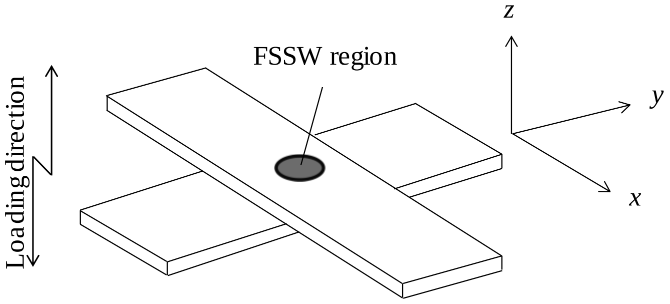

(a) Schematic illustration the FSSW specimen

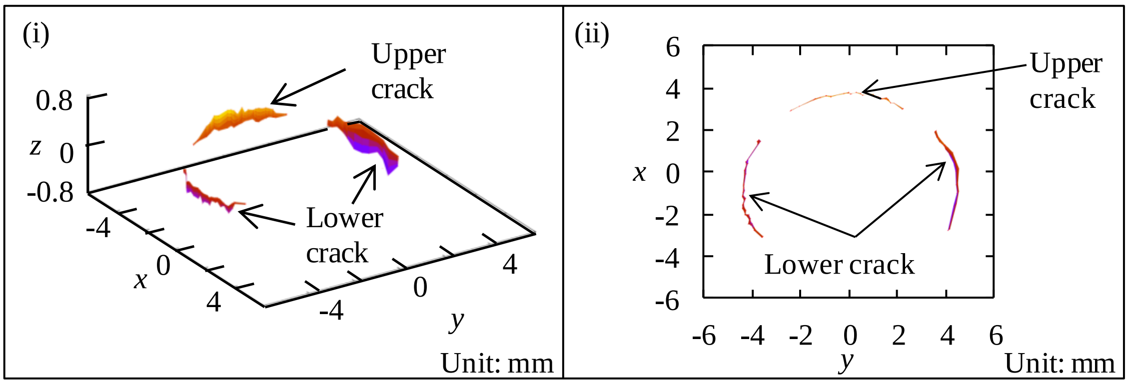

(b) 61.5%N/N_f

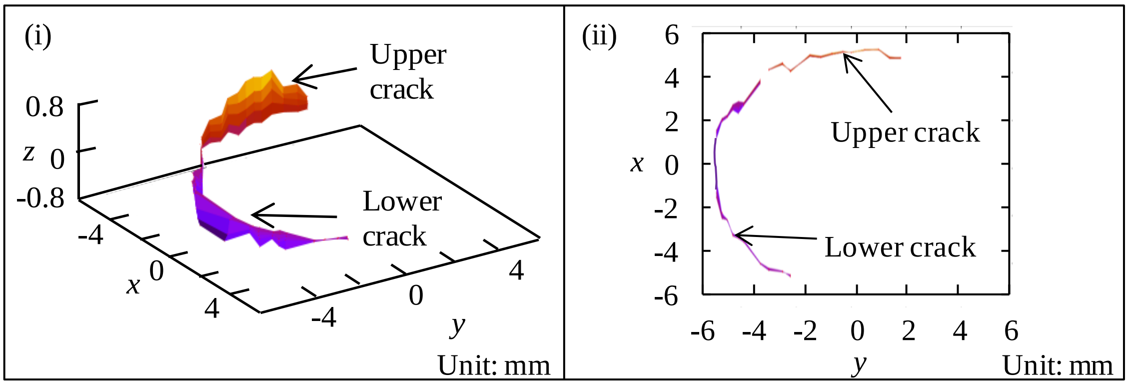

(c) 67.1%N/N_f

Fig. 4-18 Crack propagation of FSSW at low force amplitude level (P_a = 0.19 kN): (i) 3-dimension, (ii) 2-dimension.

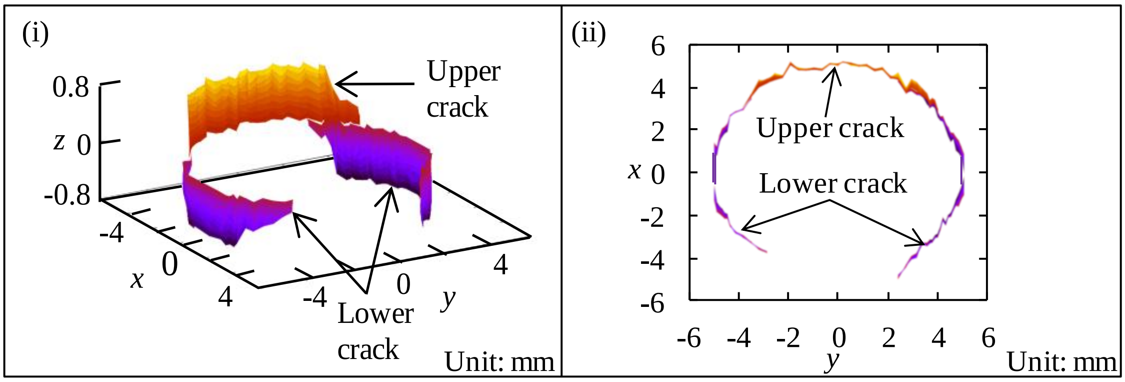

(d) 78.3%N/N_f

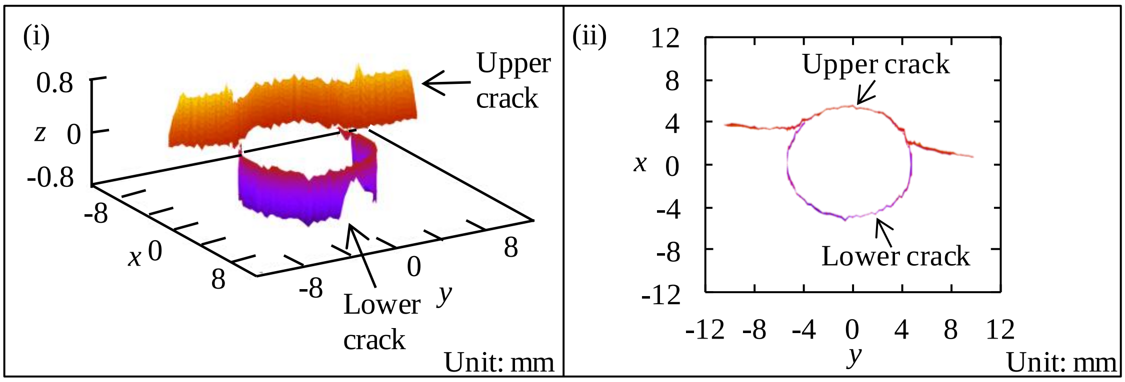

(e) 83.3%N/N_f

Fig. 4-18 Crack propagation of FSSW at low force amplitude level (P_a = 0.19 kN):

(i) 3-dimension, (ii) 2-dimension. (Continue)

4.2.5.2 High force amplitude level

According to schematic illustration in Fig. 4-18(a), Figure is shown the FSSW specimen along with *x*-*y*-*z* directions and loading direction shown in three-dimensional morphologies of the fatigue crack obtained in each observational result at the cross-sectional area. Figure 4-19 shows the fatigue crack propagation behavior under constant high force amplitude. On 23.4%N/N_f, Fig. 4-19(a) shown that the fatigue crack propagated with 0.7 mm towards thickness direction of upper sheet. This indicates that the fatigue crack has grown to the full thickness of the steel. Furthermore, there was no fatigue crack near the welded spot on 15.6%N/N_f. This fact implies that cross tension specimen used in this study requires few cyclic loading to initiate the fatigue crack in the high force amplitude level. On 45.2%N/N_f, Fig. 4-19(b) shows two fatigue cracks on upper sheet. In this case, fatigue crack grows to the full thickness of sheet. And, the fatigue cracks tend to grows around the welded joint as equal to the diameter of shoulder of FSSW tool and further it grows to the one side on base metal. Another fatigue crack was occurred opposite side of the first crack with propagation of 0.4 mm toward thickness direction and the crack length 1.5 mm near the welded joint. Finally, Figs. 4-19(c) and (d) show two fatigue cracks on upper sheet those fatigue cracks grows to the full thickness of sheet and tend to grows around the welded joint. Further, first fatigue crack grows to the one side on base metal and another fatigue crack was occurred opposite side of the first fatigue crack around the welded joint. As cracks on lower sheet, two cracks were occurred and grow around the welded joint.

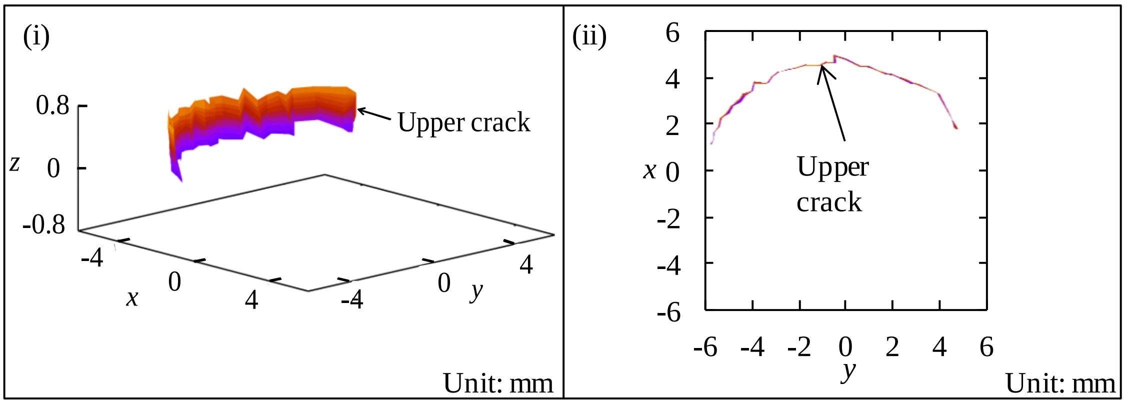

(a) 23.4.%N/N_f

Fig. 4-19 Crack propagation of FSSW at high force amplitude level (P_a = 0.50 kN):

(i) 3-dimension, (ii) 2-dimension.

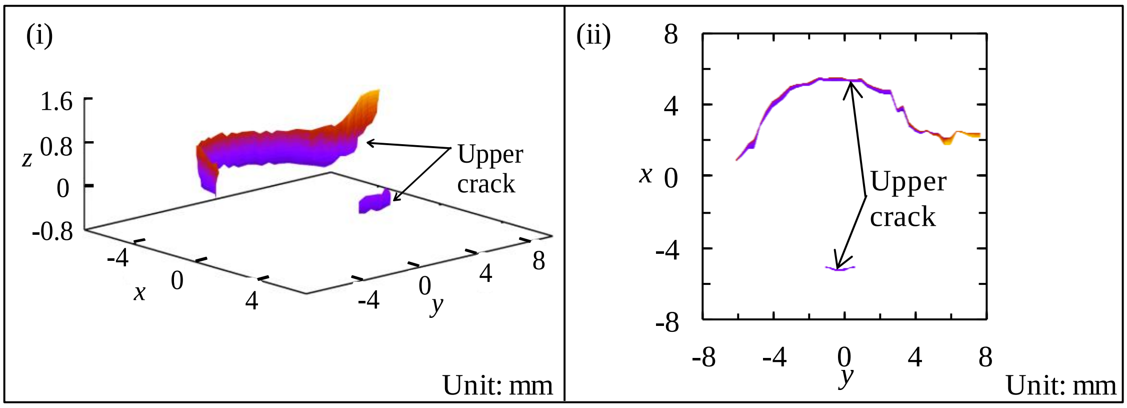

(b) 45.2%N/N_f

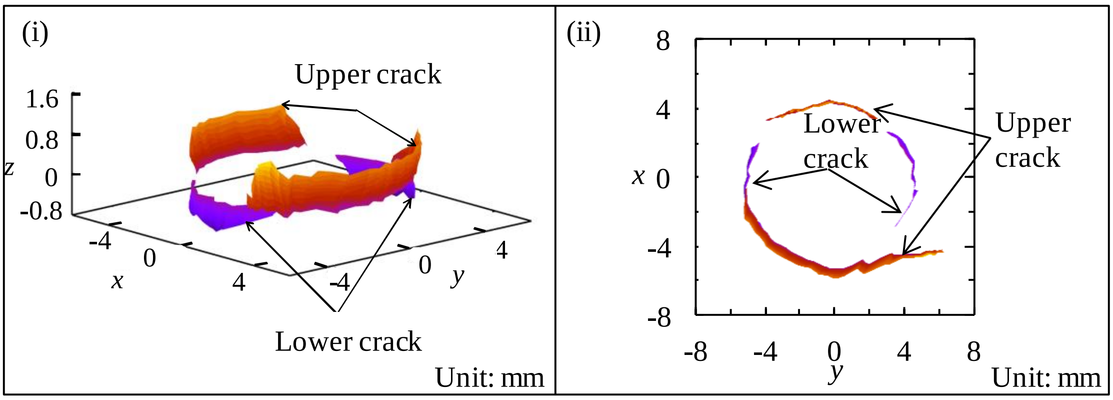

(c) 58.5%N/N_f

Fig. 4-19 Crack propagation of FSSW at high force amplitude level (P_a = 0.50 kN):

(i) 3-dimension, (ii) 2-dimension. (Continue)

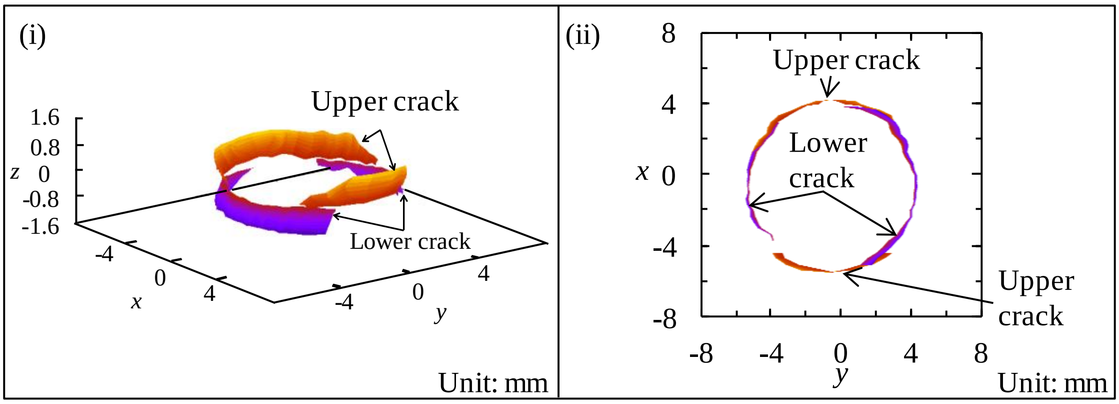

(d) 70.2%N/N_f

Fig. 4-19 Crack propagation of FSSW at high force amplitude level (P_a = 0.50 kN):

(i) 3-dimension, (ii) 2-dimension. (Continue)

Based on the three-dimensional observation, it is clarified that the fatigue crack in the welded joints used in this study initiated at the slit tip, then propagated with the complex behavior regardless of the force amplitude level. However, the fatigue crack initiation life against the entire fatigue life was dependent on the force amplitude; the higher force amplitude, the faster fatigue crack initiation life.

4.3 Conclusions

In this chapter, the mechanical properties and fatigue crack growth behavior of the FSSW cold-rolled carbon steel joints were investigated under constant force amplitude. The low temperature friction stir welding of steels was observed around 973 K, which should be the first example of welding general steels without any transformation. In addition, the control of the temperature enabled the steels to be welded in various regions, such as the α-γ two-phase region and the γ single-phase region. From this work, the following conclusions were achieved.

(1) It has observed that the relationship between the peak temperature and the A_1 point. When the FSSW is performed in the α-γ two-phase region, the microstructure is refined and the highest hardness is then achieved.

(2) The hardness of the welded area was hardening occurred up to 60% relative to the base metal. This was caused by the generation of extremely fine grains and pearlite phase structure in the SZ and TMAZ, and the impulse compressive force from the welding process.

(3) The specimen used for this study had a fatigue limit of 0.1 kN. This value is very low compared with the maximum tensile force of the base metal and FSSW joint itself.

(4) The crack initiation occurred as a boundary between the welding interface zone and non-interface zone or slit tip regardless of amplitude level. In addition, the distal slit is located in the HAZ. The fatigue crack was found on the upper sheet at the distal slit through to the surface of sheet up to the concave zone. The fracture morphology is the mixed mode fracture. Therefore, fatigue fracture modes were independent on force amplitude level.

(5) Three-dimensional observation clarified the fatigue fracture mechanism in FSSW joints.

Furthermore, the results of the three-dimensional observation and the micrograph near the welded joint showed that the fatigue crack initiation of low force amplitude level was approximately 56%N/N_f of the whole fatigue life. Consequently, the FSSW joints had a fatigue crack initiation life that accounted comparatively large- proportion of the whole fatigue life. In contrast with high force amplitude level was approximately 16%N/N_f of the whole fatigue life, which FSSW joints had a fatigue crack initiation life that accounted comparatively less proportion of the whole fatigue life. Therefore, fatigue crack initiation on high force amplitude level is very fast compared to low force amplitude level.

CHAPTER 5

Fatigue damage evaluation of friction stir spot welded cross-tension joints under repeated two-step force amplitudes

5.1 Introduction

Recently, the majority of fatigue tests were carried out under constant amplitude loading. Engineer are faced with the problem of how to use constant amplitude fatigue data in the prediction of the fatigue lives under the wide range of variable amplitude histories encountered service. The investigated of fatigue properties under variable amplitude loading came to known as the cumulative damage study. As applied in fatigue test, a block loading is one in which the loading parameters vary stepwise with the time. Interaction effects affecting fatigue crack propagation rates in metallic materials can occur when load levels change during a block fatigue loading. Within a block fatigue loading each block consists of a constant amplitude fatigue loading. At the new load level the fatigue crack propagation rate may not be the same as it would be for the same fatigue load under constant amplitude fatigue loading. Numerous tests have been carried in attempts to quantify interaction effects, including tests using the simple two level loads.

The previous chapter proposed the interior fatigue crack mechanism of FSSW using AISI 1012 cold-rolled steel sheet in detailed of fracture mode, 3-dimensional crack observation and crack initiation site. In addition, the experiment of FSSW has focused on microstructure, tensile test, and hardness test.

Previous research of FSSW on fatigue test, many authors have performed fatigue test under constant amplitude loading. Some authors have studied the fatigue tests under repeated two-step amplitude loading on alloy series to analyze the strain behavior [65], [66] or determine fatigue life, and failure modes of specimens [35], [53]. However, few reports exist on the fatigue fracture mechanism and fatigue crack propagation behavior in FSSW-joined carbon steel, particularly for cross-tension FSSW specimens [58]. Moreover, some stress concentration parts remain at the area welded by FSSW: a hollow called a keyhole caused by the tool shape, a discontinuity in shape called a lip, and a slit between the upper and lower sheet. Furthermore, the area welded by FSSW has several microstructures: base metal (BM), heat-affected zone (HAZ), thermo-mechanically affected zone (TMAZ), and stir zone (SZ) as showed in previous chapter. It is highly advantageous to identify the relationship between the shape of the welded area unique to FSSW, the microstructure, and the fatigue crack behavior; however, details are not definitively known. Moreover, most studies on the fatigue properties of FSSW joints were conducted under constant force amplitude conditions; although some studies have reported the fatigue properties under variable force amplitude conditions [19], [71]. However, automobile loads randomly vary in service and very little is known about fatigue properties under variable force amplitude conditions, which are assumed to occur in actual force situations.

This chapter, fatigue tests were performed under repeated two-step force amplitudes to investigate the fatigue properties of FSSW-joined AISI 1012 cold-rolled steel sheet by using the results of fatigue tests under constant force amplitude from the chapter 4. Welded components are often subjected to repeated two-step force amplitudes, which call for fatigue life prediction methods that consider fatigue damage accumulation. Therefore, this study proposes and demonstrates the effectiveness of a method for evaluating cumulative fatigue damage under repeated two-step force amplitude conditions.

5.2 Results and discussion

5.2.1 Deformation behavior of FSSWed specimen

In this section, a fatigue damage evaluation method under repeated two-step force amplitudes was investigated based on the results under constant force amplitude from a previous chapter. The FSSW joints used in this study shows a deformation behavior specific to the thin plate structure as shown in Fig.5-1. From the figure, it was found that the FSSW specimen is deformed from the force during fatigue test. Therefore, the deformation behavior around the welded zone with the constant applied force amplitude was observed prior to the repeated two-step fatigue tests.

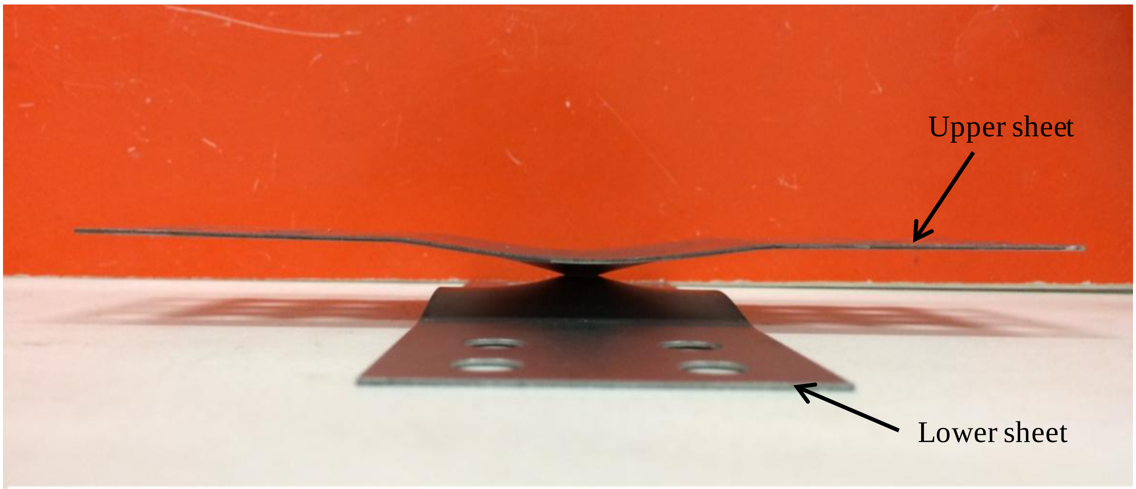

Fig. 5-1 The deformation behavior of FSSW specimen.

To study the deformation behavior, the strain behaviors were measured near the welded joints under force-loop test. Figure 5-2 shows the schematic of the force-loop test, which was performed by operating the ramp wave to loading and unloading for 10 s each in each step. In addition, the applied force was increasing of 0.5 kN in each step when the loop performed by loading. The local strain was measured during the force-loop test near the welded zone using the local strain measurement method shown in Fig.5-3.

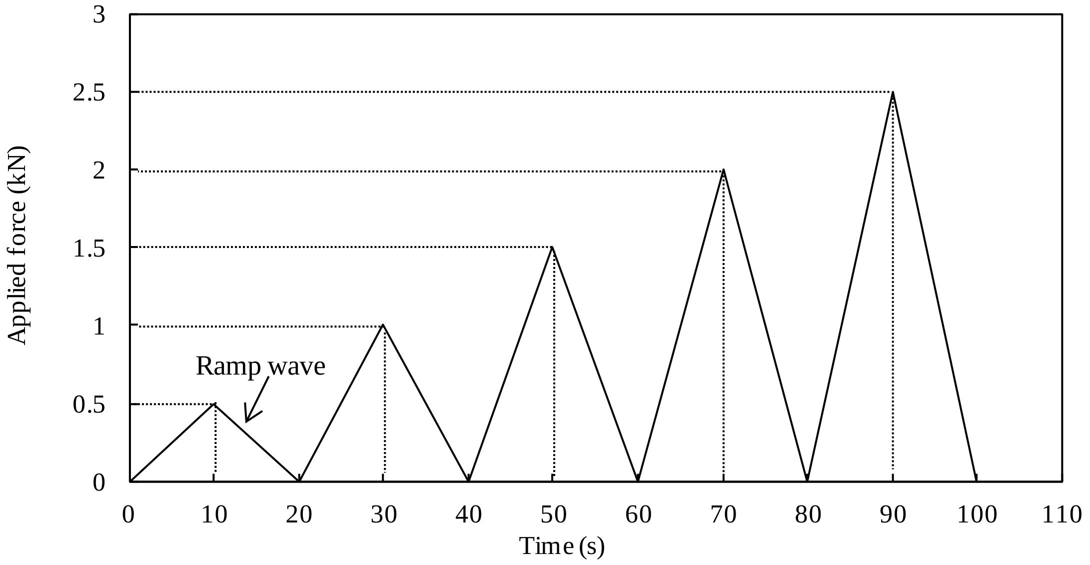

Fig. 5-2 Schematic illustration of the force-loop test.

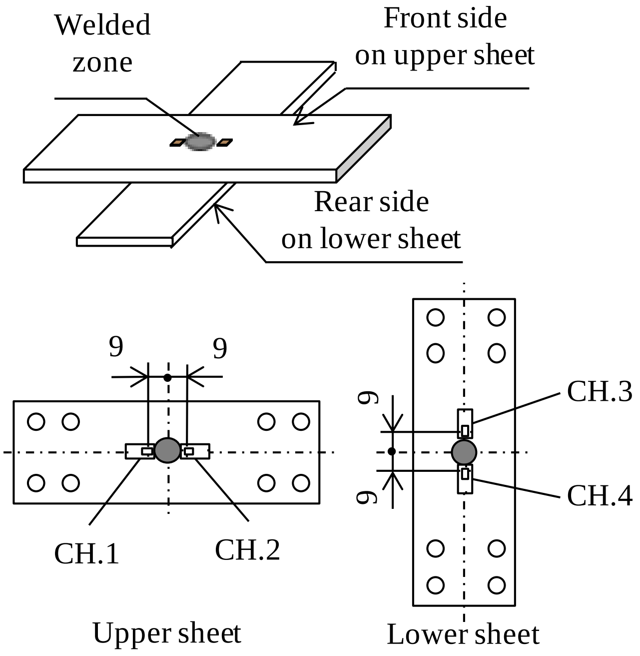

Fig. 5-3 Four strain gage locations on FSSW specimen.

The results are displayed in Figs. 5-4 (a)-(d) as a plot of applied force and local strain, which is measured from the strain gage CH.1, CH2, CH3, and CH.4 respectively. Figures 5-4 (e) and (f) show enlarged images of the first and second steps with force loops of 0→0.5→0 kN and 0→1.0→0 kN, respectively.

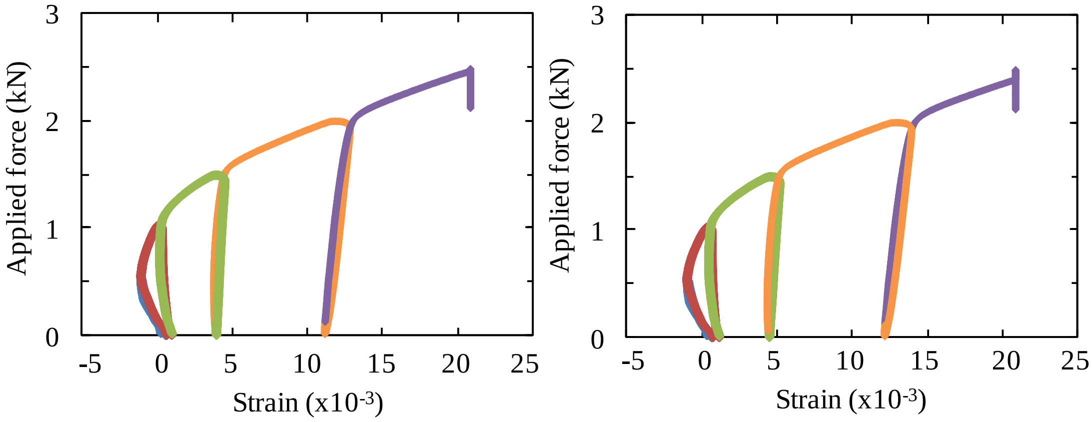

(a) CH 1

(b) CH 2

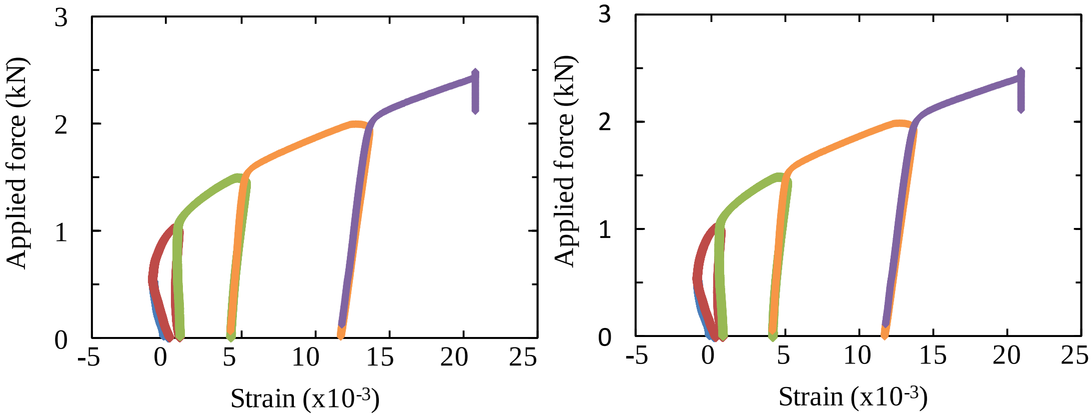

(c) CH 3

(b) CH 4

Fig. 5-4 The relationship between local strain and applied force.

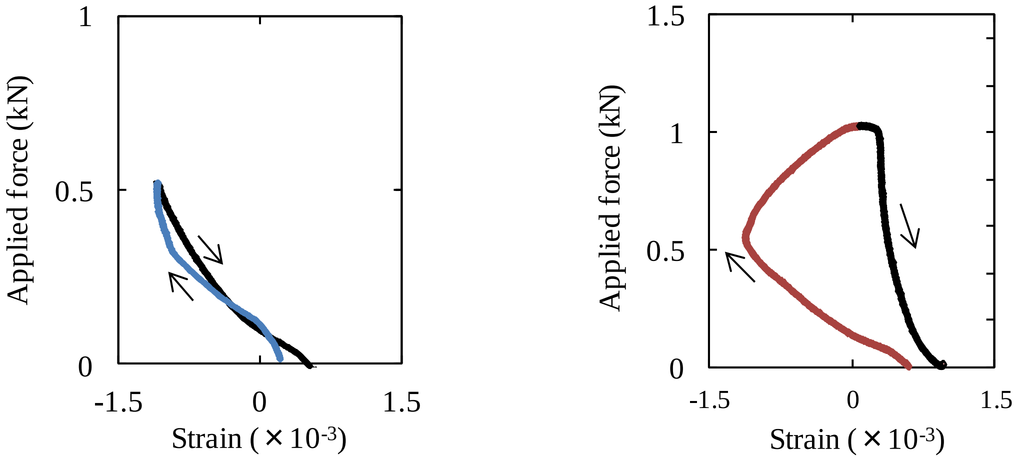

(e) The enlarged image of CH.1 of the first step with a force loop of 0→0.5→0 kN

(f) The enlarged image of CH.1of the second step with a force loop of 0→1.0→0 kN

Fig. 5-4 The relationship between local strain and applied force. (Continue)

The results show that the plastic deformation near the welded zone occurred under a force of 0.4–0.5 kN. Therefore, in this study, fatigue tests were performed under repeated two-step force amplitudes, consisting of a case in which no macroscopic plastic deformation occurred and a case in which significant plastic deformation occurred. Through these experiments, the effect of repeated two-step force amplitudes on the fatigue characteristics of the FSSW joints was investigated.

Based on the illustration of the repeated two-step force amplitude waveform in Fig. 5-5, fatigue tests were performed with 200 and 500 cycles loaded with ΔP_{H} after the specimen was loaded with ΔP_{L}. The force ratios R were 0.01 for ΔP_{H} and 0.01–0.04 for ΔP_{L} because the minimum force of ΔP_{L} was set to follow the minimum force of ΔP_{H}.

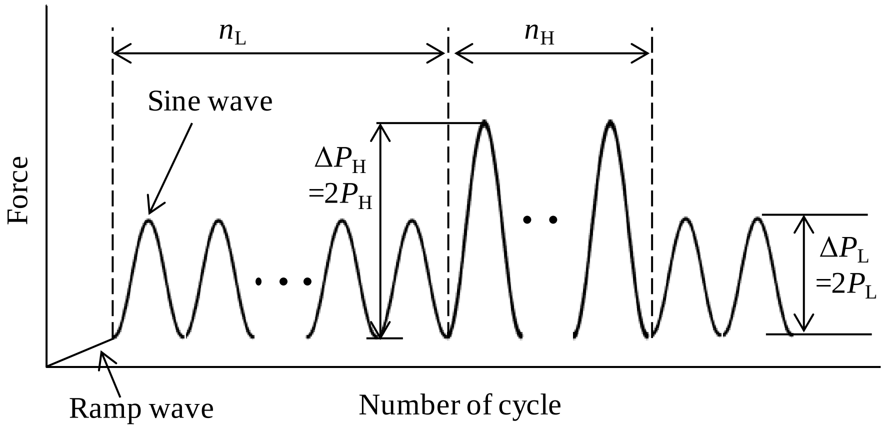

Fig. 5-5 Illustration of force amplitude wave form of repeated two-step force amplitude.

5.2.2 Case without macroscopic plastic deformation

This section describes the fatigue tests that were performed under repeated two-step force amplitudes with a high force range of ΔP_H = 0.39 kN and a low force range ΔP_L lower than the fatigue limit. Linear damage cumulative rule is used in this section. Theoretical and experimental research has shown that use of the linear damage cumulative rule, which is Miner's rule (LDR). Miner represented the Palmgren linear damage concept in mathematical form as the LDR equation presented by Eq. (5-1);

$$D = \sum r_i = \sum (n_i / N_{fi}) = 1 \tag{5-1}$$

In the LDR, the measurement of damage is the cycle ratio with basic assumptions of constant work absorption per cycle, and characteristic amount of work absorbed at failure. The energy accumulation, therefore, leads to a linear summation of cycle ratio or damage. Failure is accounted to occur when $\sum r_i = 1$, where r_i is the cycle ratio corresponding to the i load level or $r_i = n_i/N_{fi}$. Damage versus cycle ratio plot for this rule is simply a diagonal straight line as shown in Fig. 5-6, independent of loading levels (the damage curve as it is usually called). In the S-N

diagram, the residual life curves corresponding to different life fractions are essentially parallel to the original *S*-*N* curve at failure. The main deficiencies with LDR are its load-level independence, load-sequence independence and lack of load-interaction accountability.

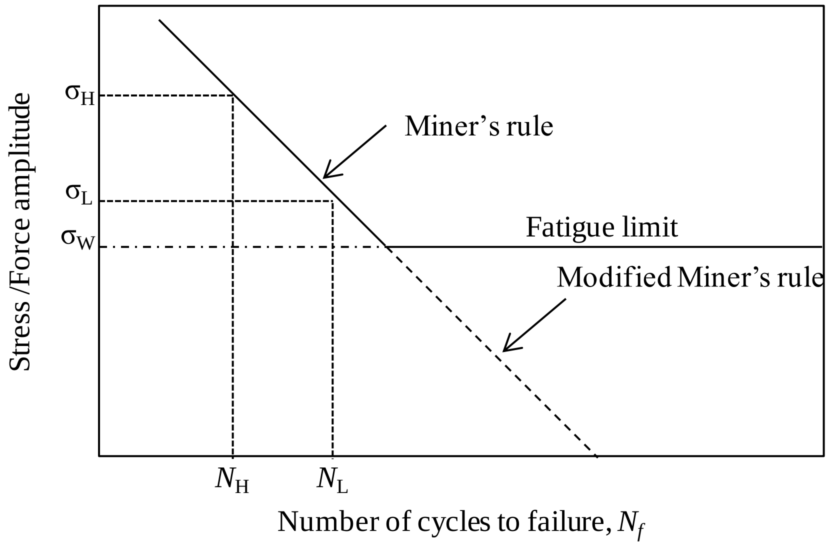

Fig. 5-6 Schematic illustration for LDR.

The fatigue damage was estimated based on Miner's rule (D_M), which considers only the damage due to the forces above the fatigue limit, and the modified Miner's rule (D_{MM}), which considers the damage due to the forces both below and above the fatigue limit, as expressed by Eqs. (5-2) and (5-3), respectively. From the fatigue test results of each approach, the validity was evaluated based on the cumulative damage rule.

$$D_M = \left(\frac{n_H}{N_H} \right) \times Block\ \ number \tag{5-2}$$

and

$$D_{MM} = \left(\frac{n_L}{N_L} + \frac{n_H}{N_H} \right) \times Block\ \ number \tag{5-3}$$

where n_H and n_L are the number of repeated cycles with high and low force amplitudes in one block, respectively, and N_H and N_L are the estimated fatigue lifetimes, measured in numbers of cycles, corresponding to the force amplitudes P_H and P_L, respectively. The values for N_H and N_L were obtained from the fatigue test results with a constant force amplitude by using the regression line of the *P*–*N* curve, as shown in Fig. 5-7, with N_L taken as the value from the regression line extended below the fatigue limit. The regression equation was obtained on a log–log scale, as expressed by Eq. (5-4).

$$\log P_a = -0.325 \log N_f + 3.956 \tag{5-4}$$

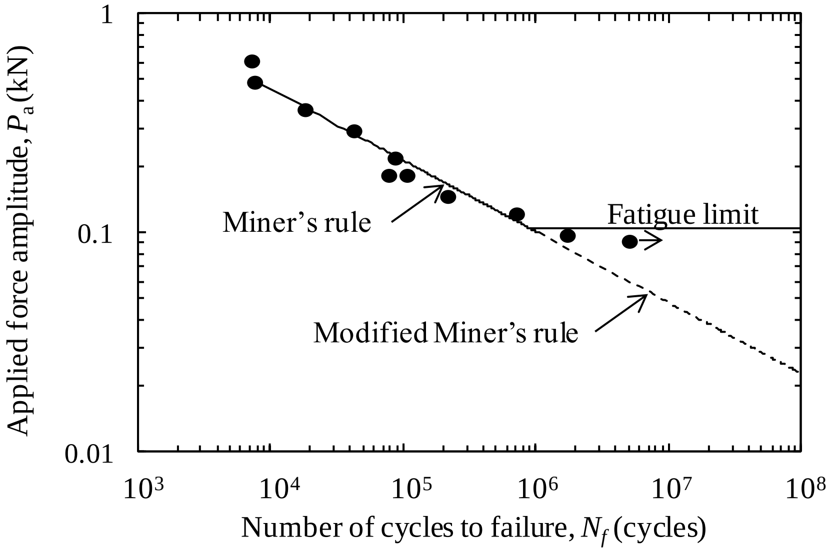

Fig. 5-7 *P*–*N* curve of the FSSW specimen.

The cumulative damage results of repeated two-step force amplitudes in the case without macroscopic plastic deformation summarize in Table 5-1. The results show that D_M was considerably lower than unity for all specimens and D_{MM} was larger than unity. The experimental results obtained using the modified Miner’s rule indicated that the forces below the fatigue limit influence fatigue damage. As such, the fatigue limit of the welded joint disappeared under repeated two-step force amplitude conditions. However, it is not appropriate to use the modified Miner's rule in estimating the fatigue damage of the welded joint under variable force amplitude conditions, because D_{MM} was consistently larger than unity. This means that the fatigue damage evaluation with the modified Miner's rule tends to overestimate the damage by applied forces below the fatigue limit, which yields an evaluation erring too much on the side of safety. Therefore, the fatigue damage in this study was re-evaluated using the regression equation suggested by Haibach [170].

Table 5-1 Results of cumulative fatigue damage test with repeated two-step force amplitude in the case without macroscopic plastic deformation.

Specimen No.	n_H/n_L (cycles)	ΔP_H (kN)	ΔP_L (kN)	$\sum n_H$ (cycle)	$\sum n_L$ (cycle)	D_M	D_{MM}
1-1	200/6000	0.39	0.15	9.14×10^4	2.75×10^6	0.72	1.77
1-2				6.35×10^4	1.91×10^6	0.50	1.23
2-1	200/24000	0.39	0.10	7.38×10^4	8.83×10^6	0.58	1.55
2-2				9.02×10^4	1.08×10^7	0.71	1.90

The suggestion for extending the *P*-*N* curves (*S*-*N* curve) below the fatigue limit was proposed by Haibach, which is Haibach's method line in Fig.5-8. Haibach postulated that cycles with amplitudes above the fatigue limit will reduce the fatigue limit of the undamaged material. The damage of these cycles was accounted for by applying the Miner rule to the modification of the *S*-*N* relation by the extension with Haibach's method line in Fig.5-8.

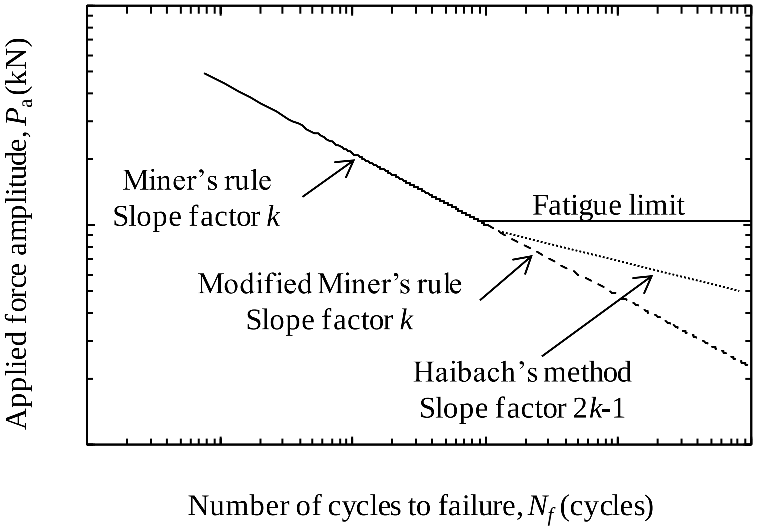

Fig. 5-8 Modification of *P-N* curve for Haibach's method.

According to Haibach, the slope of Haibach's method line is related to the slope of the Basquin relation of the original *S-N* curve; $S^k_a \cdot N$ is constant. In this equation, k should be replaced by $2k$-1. The prediction with this modified *S-N* curve is more conservative than the original Miner rule prediction, but less conservative than for the extended *S-N* curve with modified Miner's rule line. It must be recalled that the prediction with n/N remains a Miner rule prediction, which does not account for any interaction effect. Predictions must be considered with caution. The extrapolated *S-N* curves imply that an extra safety margin is introduced which intuitively seems to make sense, but it remains unknown how large this margin, and also whether the prediction will be conservative, $\sum n/N \geq 1$.

In general, Haibach's method yields an accurate evaluation when the number of repeated cycles of an applied force below the fatigue limit is quite large. The regression line modified by Haibach is shown in Fig. 5-9, and its regression equation is given by Eq. (5-5).

$$\begin{aligned} \log P_a &= -0.325 \log N_f + 3.956 \quad \text{for}\, P_a \geq 0.1\,\text{kN} \\ \log P_a &= -0.194 \log N_f + 3.068 \quad \text{for}\, P_a < 0.1\,\text{kN} \end{aligned} \qquad (5\text{-}5)$$

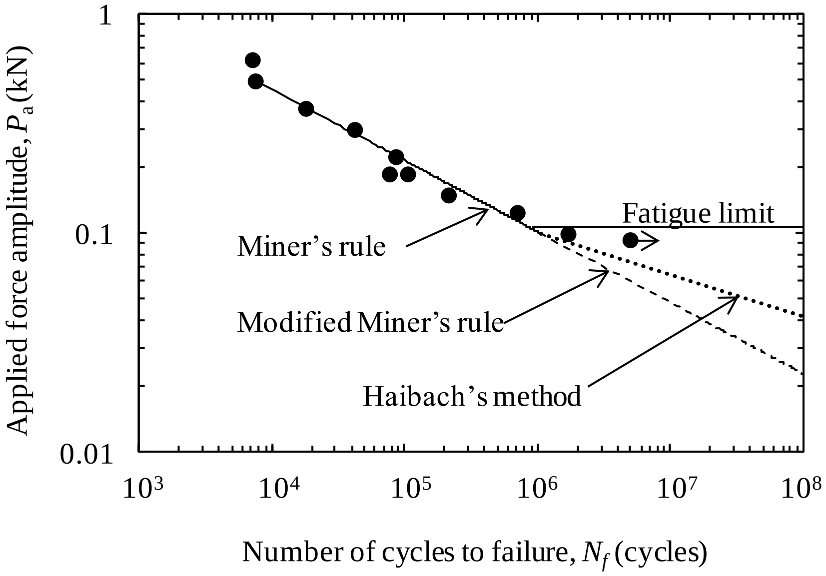

Fig. 5-9 Modification of *P*-*N* curve using Haibach's method.

The resulting cumulative damage D_H determined by Haibach's method is shown in Table 5-2. The results show that D_H was approximately unity for each of the specimens. This is due to the fact that the damaging effect resulting from the number of cycles with a force below the fatigue limit depends on the frequency ratio of the number of cycles with a force above the fatigue limit (Frequency ratio is ratio of number of cycle of high force amplitude (n_H) to number of cycle of low force amplitude (n_L) on 1 block, or n_H/n_L). Therefore, Haibach's method yields an accurate evaluation when a large number of cycles are performed below the fatigue limit, and considering the effect of forces below the fatigue limit is important in practical applications when evaluating the fatigue characteristics of the welded joint under variable force amplitudes.

Table 5-2 Results of the modification cumulative fatigue damage test under repeated two-step force amplitude in the case without macroscopic plastic deformation with Haibach's method.

Specimen No.	D_{M}	D_{MM}	D_{H}
1-1	0.72	1.77	1.28
1-2	0.50	1.23	0.89
2-1	0.58	1.55	0.80
2-2	0.71	1.90	0.98

5.2.3 Case with significant plastic deformation

In this section, fatigue tests under repeated two-step force amplitudes were performed with a high force range of $\Delta P_{\mathrm{H}} > 0.4$ kN and low force range of $\Delta P_{\mathrm{L}} = 0.39$ kN. Both the high and low force ranges were set to exceed the fatigue limit. This means that $D_{\mathrm{M}} = D_{\mathrm{MM}} = D_{\mathrm{H}}$. Therefore, Miner's rule (D_{M}) is used as the fatigue damage evaluation method for these tests.

Table 5-3 shows the cumulative damage results of repeated two-step force amplitudes in the case with significant plastic deformation. D_{M} was larger than unity for all specimens but one. This means that the evaluation by D_{M} erred too much on the side of safety. Significant plastic deformation occurred when forces higher than 0.4 kN were applied to the welded zones, as mentioned previously. It is possible that the plastic deformation led to changes in the strain behavior.

Table 5-3 Results of cumulative fatigue damage test with repeated two-step force amplitude in the case with significant plastic deformation.

Specimen No.	n_H/n_L (cycle)	ΔP_H (kN)	ΔP_L (kN)	$\sum n_H$ (cycle)	$\sum n_L$ (cycle)	D_M
3-1	500/1500	0.69	0.39	1.61×10^4	4.95×10^4	1.09
3-2				1.38×10^4	4.20×10^4	0.93
4-1	200/1800	0.99	0.39	7.07×10^3	6.48×10^4	1.47
4-2				7.61×10^3	7.20×10^4	1.57
5-1	500/4500			7.22×10^3	6.66×10^4	1.52
5-2				9.03×10^3	8.55×10^4	1.86

The present result has confirmed that the evaluation by D_M erred too much on the side of safety. It is possible that the plastic strain led to change the strain behavior when the force was applied higher than 0.4 kN. Therefore, the local strain near a welded zone was measured under both constant and repeated two-step force conditions.

The strain ranges of the constant force range and two-step force range specimens (Nos. 3-1, 4-1, and 5-1) were selected from strain gages that the strain range is changed, which is the indication that the strain gage is located near the crack initiation side. The local strain measurement method is shown in Fig. 5-3. The strain range of the two-step force range specimens corresponded to the strain behavior for applied force range $\Delta P_L = 0.39$ kN.

The results of the strain range under constant and two-step force ranges for each specimen as shown in Fig. 5-10. From the results, the strain ranges of the two-step force range specimens (Nos. 3-1, 4-1, and 5-1) are lower than those of the constant force range specimen. In addition, the strain range decreased as the high force range ΔP_H increased.

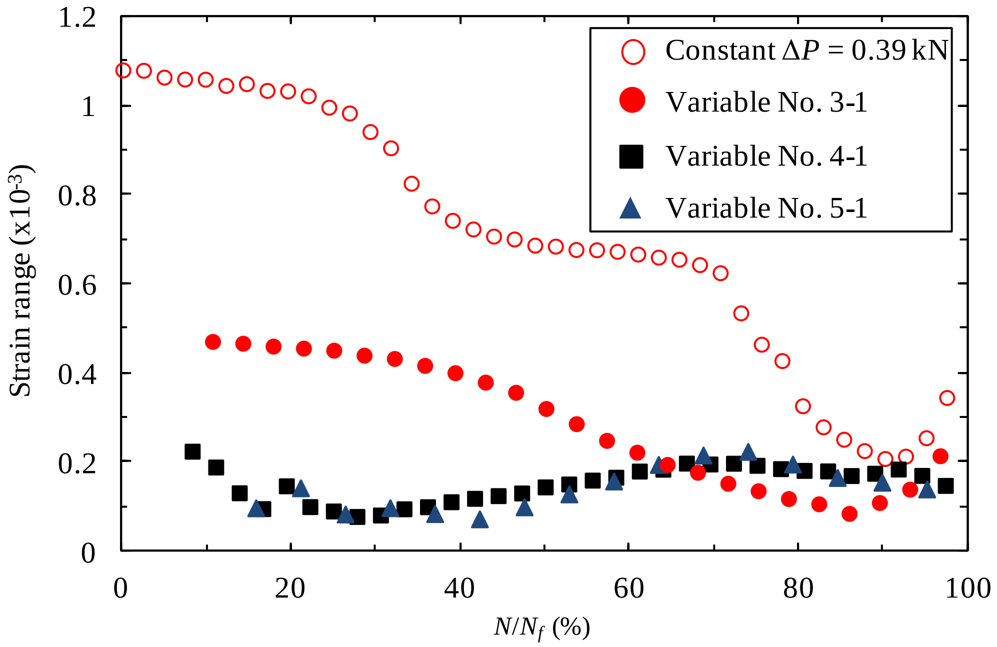

Fig. 5-10 Relationship between strain range and %N/N_f under constant and repeated two-step force range in each condition.

From the results shown in Fig. 5-10, the data of specimen No. 4-1 were plotted as strain versus time in Fig.5-11(a) with Fig.5-11(b) presenting a schematic illustration of the strain behavior. Compared to the low force range of block 1 (ΔP_{L1}), the low force range of block 2 (ΔP_{L2}) has a lower strain range and an increased mean strain. Additionally, the strain behavior under the low force range of block 2 (ΔP_{L2}) was approximately equal to that under the high force range of block 1 (ΔP_{H1}). Therefore, pre-strain from the high force range ΔP_H influenced the strain behavior and tended to affect the fatigue life of the welded joint.

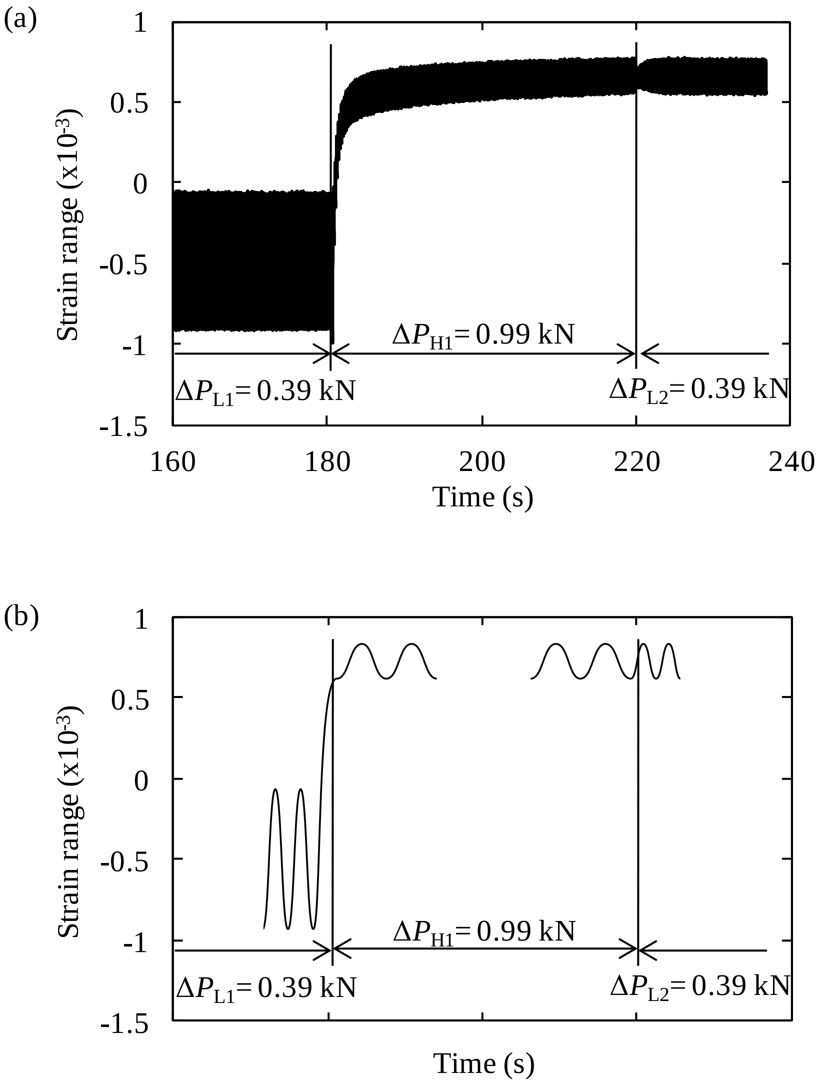

Fig. 5-11 (a) Local strain of the specimen of repeated two-step force range No. 4-1, (b) Schematic illustration of Fig. (a).

To investigate the effect of the high force range ΔP_H, additional fatigue tests were performed with 100 cycles each of the high force range ΔP_H and the low force range $\Delta P_L = 0.39$ kN until the specimen was broken; this type of test is called a pre-strain fatigue test. The waveform of the pre-strain fatigue test is shown in Fig.5-12.

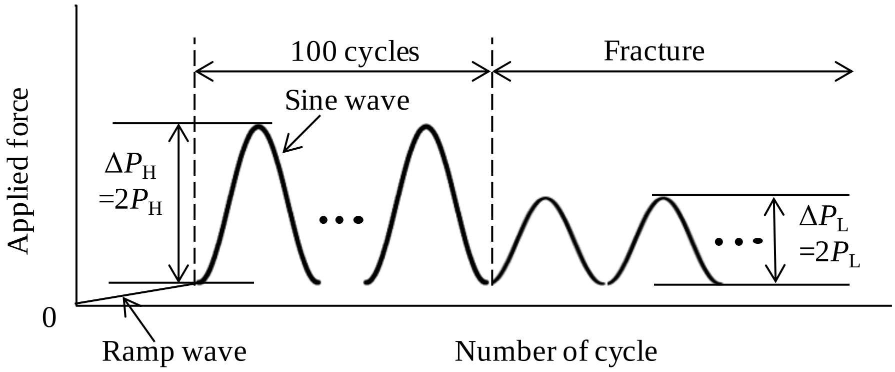

Fig. 5-12 Illustration of waveform of pre-strain fatigue test.

Figure 5-13 shows the results of the pre-strain fatigue test. The vertical axis in this figure indicates the applied low force amplitude P_L after 100 cycles of the high force range ΔP_H, and horizontal axis is the number of cycle to failure (N_{LPRE}) under the low force amplitude P_L after 100 cycles of the high force range ΔP_H. For comparison, the results under constant force amplitude are also plotted in this figure, with the data represented by circles. From the results, the effect of pre-strain from the high force range ΔP_H was clearly observed. Furthermore, the fatigue life was extended with an increased high force range ΔP_H.

Base on the experimental results, the cumulative fatigue damage was re-determined under the extended fatigue life. Therefore, the fatigue life from the pre-strain fatigue test (N_{LPRE}) is substituted by N_L in Eq. (5-3) to determine cumulative fatigue damage (D_{MPRE}), as expressed by Eq. (5-6).

$$D_{MPRE} = \left(\frac{n_L}{N_{LPRE}} + \frac{n_H}{N_H} \right) \times Block\ number \tag{5-6}$$

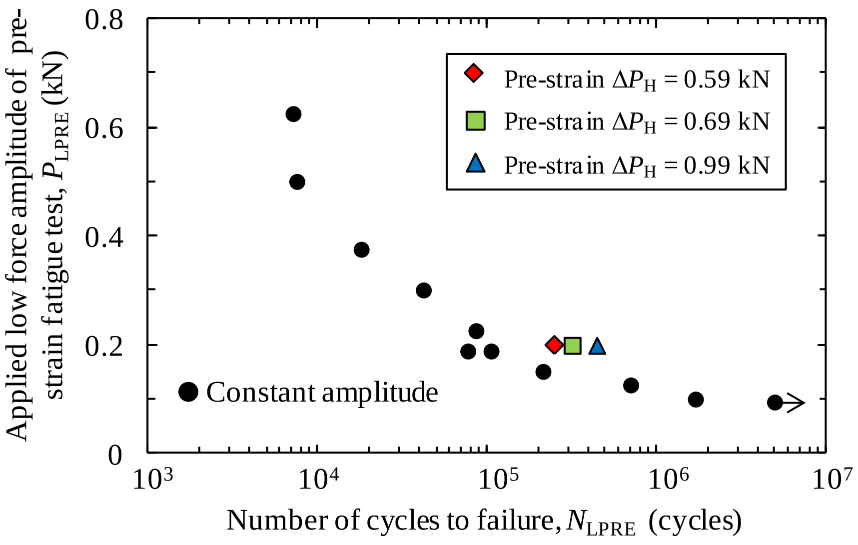

Fig. 5-13 Results of fatigue test under pre-strain and constant force amplitude.

Consequently, D_{MPRE} was approximately unity, as shown in Table 5-4. In the case with significant plastic deformation occurring near the welded zone caused by the high force range ΔP_H, a relatively accurate estimation of the cumulative damage can be achieved. Therefore, it is important to consider the cumulative damage estimation taking into account the effect of pre-strain by the high force amplitude.

Table 5-4 Results of cumulative fatigue damage test under repeated two-step force amplitude in the case with significant plastic deformation with extended fatigue life.

Specimen No.	n_H/n_L (cycle)	ΔP_H (kN)	ΔP_L (kN)	$\sum n_H$ (cycle)	$\sum n_L$ (cycle)	D_M	N_{LPRE} (cycle)	D_{MPRE}
3-1	500/1500	0.69	0.39	1.61×10^4	4.95×10^4	1.09	3.19×10^5	0.86
3-2				1.38×10^4	4.20×10^4	0.93		0.74
4-1	200/1800	0.99	0.39	7.07×10^3	6.48×10^4	1.47	4.46×10^5	1.10
4-2				7.61×10^3	7.20×10^4	1.57		1.16
5-1	500/4500			7.22×10^3	6.66×10^4	1.52		1.13
5-2				9.03×10^3	8.55×10^4	1.86		1.38

5.3 Conclusions

In this chapter, the fatigue damage of FSSW specimens under two-step force amplitude conditions was investigated. Two cases were considered: in the first, macroscopic plastic deformation near the welded zone did not occur, and in the second, significant plastic deformation occurred. The conclusions obtained are as follows.

1. In fatigue tests with repeated two-step force amplitude, the fatigue limit of the welded joint disappeared. However, the fatigue damage evaluation using the modified Miner’s rule erred too much on the side of safety, as the modified Miner’s rule tends to overestimate the damage by applied forces below the fatigue limit. Thus, it was determined that, within the testing conditions used in this study, the fatigue damage evaluation using Haibach’s method yielded an accurate evaluation.
2. In the case where significant plastic deformation caused by the applied force occurred near the welded zone, the cumulative fatigue damage value based on Miner’s rule was often larger than unity. Therefore, it is important to consider a cumulative damage estimation that takes into account the effect of pre-strain from the high force amplitude.

CHAPTER 6

Fatigue damage evaluation of friction stir spot welded cross-tension joints under random force amplitude

6.1 Introduction

For dimensioning of automotive components and structures to endure fatigue loading, results which use loading series similar to in service loading have been used increasingly during the last decade. Therefore, the *S*-*N* curve has lost some of its importance, although measurements at constant stresses are necessary in any case as a basis for lifetime predictions of tests simulating in service loads.

Early, fatigue tests on structures, components and test specimens were all carried out using constant amplitude fatigue loading. However, many structures and components are subjected in service to variable amplitude fatigue loading, with variations following either a regular or a random pattern [171], [172]. Variable amplitude fatigue loadings can divided into two broad classes: those in which individual load cycles can be distinguished, such as narrow band random loading as an example shown in Fig. 6-1(a), and those in which individual load cycles cannot be distinguished, such as broad band random loading shown in Fig. 6-2(b) [173]–[175]. The modern technology for fatigue testing equipment makes it possible to apply practically any required loading history, and narrow and broad band random loading have been used extensively for some time, especially in structural testing. The use of broad band random loading can make the analysis of test results difficult. Concepts taken from random process theory are used in the characterization of random load histories. Conventions used in the fatigue testing literature sometimes differ from those usual in random process theory. Although referred to as random, load histories used in tests are usually pseudo random in that they repeat exactly after a return period [176].

The previous chapter have been studied the fatigue damage of friction stir spot welded AISI1012 cold rolled-steel sheet under repeated two-step force amplitude. The results show that the fatigue limit of the welded joints disappeared. However, the fatigue damage evaluation using modified Miner’s rule tends to overestimate by applied force below the fatigue limit. Thus, within the testing conditions used in this study, the fatigue damage modification using Haibach’s method yielded an accurate evaluation. In the case where signification plastic deformation caused by applied force occurred near the welded zone, the cumulative fatigue damage value was often larger than unity. Thus, it is important to consider a cumulative fatigue damage evaluation that takes into account the effect of pre-strain from the high force amplitude. Based on the experimental knowledge gained in this study, the fatigue characteristics of the welded joints under random force amplitude conditions should be evaluate with Miner’s rule, which is considers the cumulative fatigue damage cause by the applied force lower than the force in the case without macroscopic plastic deformation.

The main objective of this chapter is evaluating fatigue damage of cross-tension specimen by using friction stir spot welding technique, under random force amplitude conditions. The capabilities of rainflow cycle counting method and Miner’s linear damage rule are used. Therefore, this paper propose a quantitative evaluation method for cumulative damage evaluation methodology involving cycle counting base on the external random force acting on the welded joints.

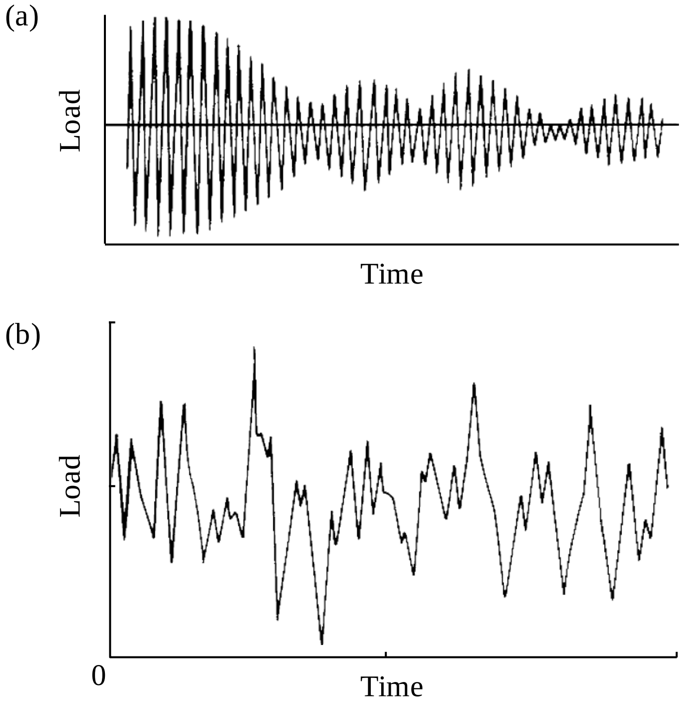

Fig. 6-1 (a) Narrow band random loading, (b) Broad band random loading.

6.2 Experimental methods

6.2.1 Random force history

Many types of random loadings encountered in the fatigue work caused. The automobile, in which a car is running, is supposed to be such a process. The same applies to random noise of an engine and body weight. It is often assumed that such processes are a random Gauss process which implies that the relevant variables have a normal distribution function, as an example of Gaussian random distribution [157], [161], [172], [176]–[178].

A Gaussian random process is defined by a power spectral density function, $\phi(\omega)$, which fully describes its statistical properties. Examples are shown in Fig. 6-2(a), the power spectral density function shows how the energy of the signal is distributed as a function of the frequency ω. This concept can be understood by considering a Fourier series with a very large number of terms and small differences ($\Delta\omega$) between the frequencies of successive terms, and coefficients x being a function of ω, as shown in Fig. 6-2(b). The load-time history is given in Eq. (6-1),

$$x(t) = a_k \cos(\omega_k t + \phi_k) \qquad (k=1,2,3...N) \tag{6-1}$$

where N is division of power spectrum distribution number. ω_k is angular frequency, t is time. ϕ_k is uniform random number in the range of (0, 2π). a_k is variable that can be determine as followed the absolute area. The absolute area can be multiplied between the power spectrum density ($S(\omega)$) and angular frequency from lower angular frequency to upper angular frequency, divided by N as expressed in Eq. (6-2). Fig. 6-3 shown the absolute area of power spectrum density ($S(\omega)$) and $\Delta\omega$.

$$\Delta\omega = (\omega_u - \omega_l)/N \qquad (6\text{-}2)$$

$$\omega_k = \omega + (k - 0.5).\Delta\omega \qquad (6\text{-}3)$$

where, a_k^2 is given by;

$$a_k^2 = 4S(\omega_k)\Delta\omega \qquad (6\text{-}4)$$

Substitute Eq. (6-4) to Eq. (6-1), the stationary Gaussian random equation is given by;

$$x(t) = \sum_{k=1}^{N} 2\sqrt{S(\omega_k)\Delta\omega}\cos(\omega_k t + \phi_k) \qquad (6\text{-}5)$$

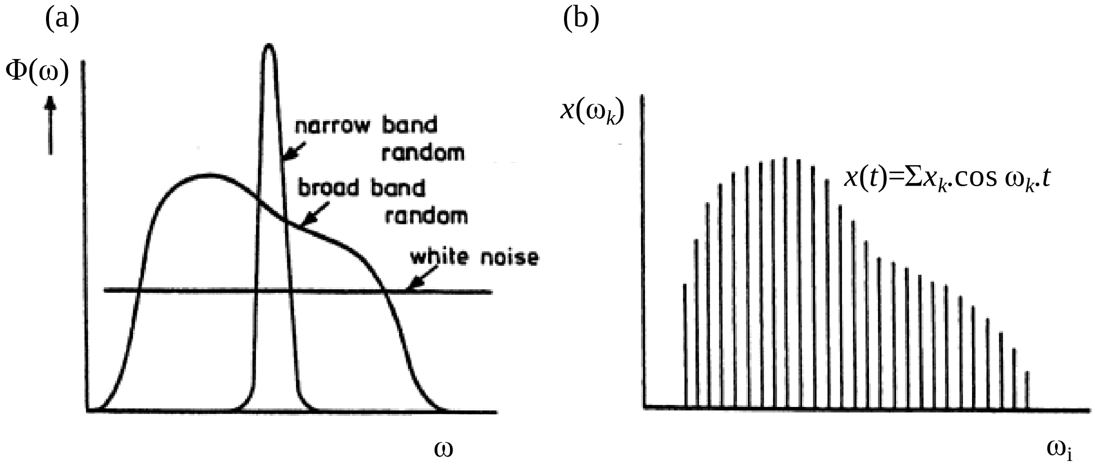

Fig. 6-2 Energy density functions to define the random load Gauss process: (a) Different types of energy density functions of the random signal, (b) Fourier series approximation of the random signal.

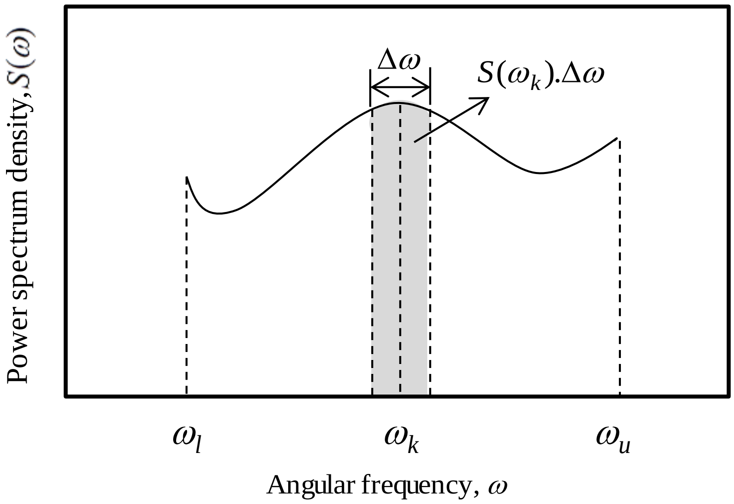

Fig. 6-3 Schematic illustration of the division of power spectrum distribution.

In this study, the frequency range speed effect on the fatigue crack growth does not almost appear, therefore, the narrow band waveform having a uniform distribution with the frequency range of 1 Hz, as shown in Fig 6-4(a) and the broad band waveform having a uniform distribution with the frequency range of 9 Hz, as shown in Fig. 6-4(b).

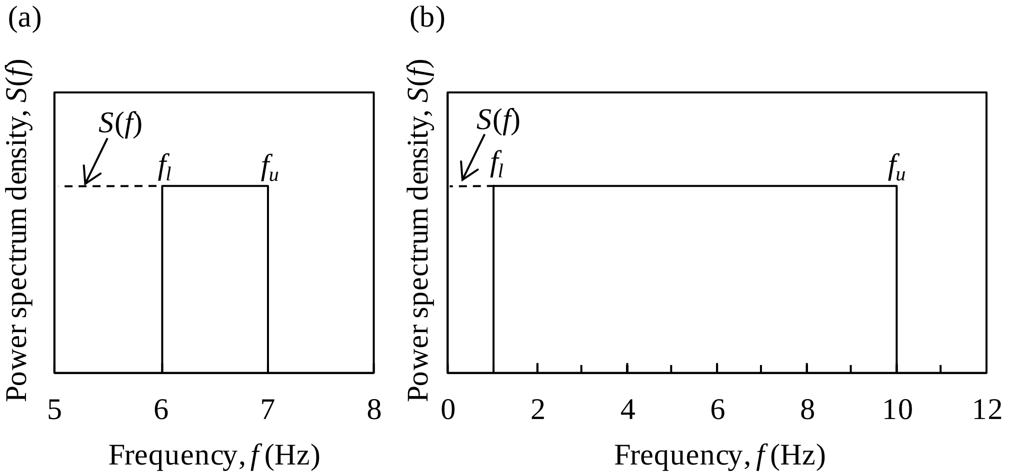

Fig. 6-4 Schematic illustration of power spectrum distribution for pseudo random loading wave: (a) Narrow band random waveform, (b) Broad band random waveform.

This sum gives a signal *x*(t) which is approximately similar to random wave. It becomes a real random Gaussian signal, if ω→0. The energy is proportional to the square of the amplitude:

$$\Phi(\omega) \propto (x(\omega))^2 \tag{6-6}$$

The examples of a stationary Gaussian random wave and the corresponding power spectral density functions are shown in Fig. 6-5. In Fig. 6-5(a), the energy is concentrated in a narrow band frequency and as a result the load-time history is somewhat similar to an amplitude modulated signal, in this case with a random modulation. This narrow band random loading is resonance frequency, if activated by some external random process covering a wider frequency band. The structure acts as a frequency filter to the excitation. The second example in Fig. 6-5(b) shows a random signal covering a wider frequency band and the corresponding broad band random waveform shows a higher degree of irregularity. It was shown that the distribution function of the peak values of a random Gaussian signal can mathematically be derived from the spectral density function (ω). This is also true for the irregularity factor *k* defined earlier as ratio of the number of peaks and the number of zero-crossings. As might be expected, this factor is almost equal to 1 for narrow band random loading, whereas it is larger for more irregularly varying signals.

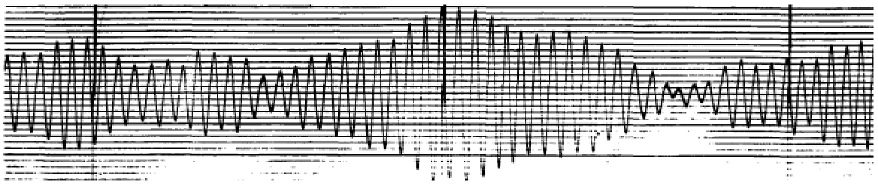

(a)
Narrow band
random load
(*k*=1)

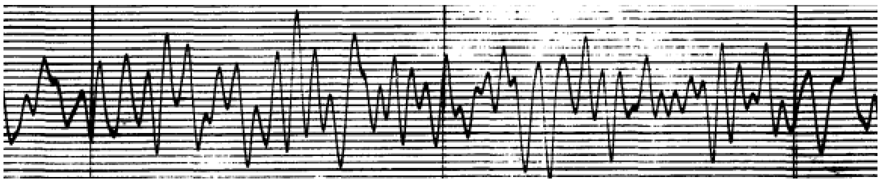

(b)
Broad band
random load
(*k*=1.27)

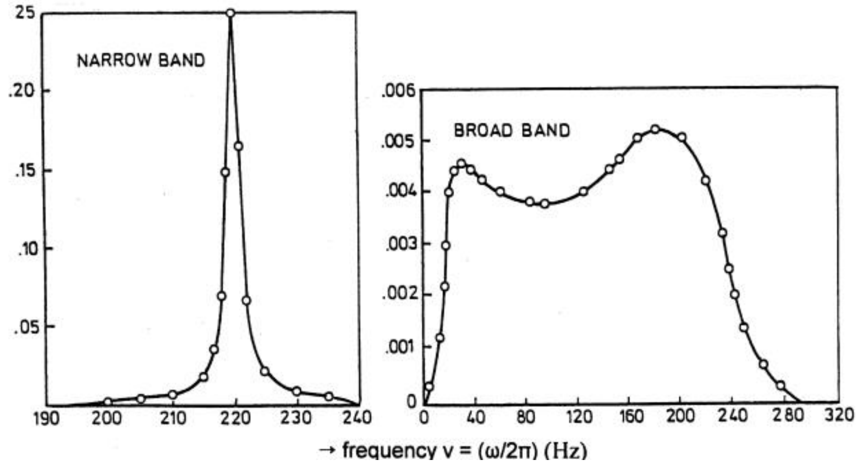

(c) Normalized spectrum density function of wave form (a) and (b.)

Fig. 6-5 The random loading history and the corresponding spectral density functions [179].

6.2.2 Cycle counting procedures

This section explains the introduction of cycle counting method. Cycle counting is used to summarize irregular loading versus time histories by providing the number of times cycles of various sizes occurred. These practices cover the procedures used to obtain cycle counts by various methods as an example as, simple-range counting, level crossing counting, and rainflow counting method. Cycle counting method can be made for time histories of force, stress, strain, torque, deflection or other loading parameters.

6.2.2.1 Level-crossing counting method

A load-time history defined by a sequence of maximum and minimum if time-dependent phenomena are not considered, such a sequence is usually reduced to a statistical representation in order to have a useful survey of the fatigue loads. In the past, several counting techniques were developed for this purpose based on counting level-crossings for a number of load levels or counting peak values above a number of load levels. The historical development will not be followed here, but basic aspects of statistical count procedures are considered. With this counting method, every time the load-time history crossing a class limit in a positive sense, a count is performed. The counting of level crossings neglects small load variations, when they are in one class. This is not the case, however, when a class limit is crossed (however, small an amount). For this reason, the result of this counting method depends on the magnitude of the amplitude suppression. The result of the counting is a cumulative frequency which is usually presented in a spectrum.

6.2.2.2 Peak counting method

From a fatigue damage viewpoint, loading amplitudes are more significant than mean loads. The amplitude is half the range between a minimum loading and the subsequent maximum loading. Load ranges represent important characteristic values of a load-time history exerted on a structure or applied in a fatigue tests. Load ranges of a load-time history can be counted, but since ranges are defined by minimum and a maximum reversal, a two-parameter counting methods must be adopted. Results can be presented in matrix format.

6.2.2.3 Simple range counting method

Range is the difference between two successive reversals. The range is positive when a valley is followed by a peak. The range is negative when a peak is followed by a valley. Count positive or negative ranges as one cycle if only one or the other is counted. Count each as one-half cycle if both are counted. Eliminate ranges smaller than a chosen number before counting.

6.2.2.4 Rainflow counting method

The rainflow counting method [172], [175], [180], [181] is a method for counting fatigue cycles from a time history. The fatigue cycles are stress (loading)-reversals. The rainflow counting method allows the application of Miner's rule in order to assess the fatigue life of a structure subjected to complex loading. In the principle, the range counting includes counting of all successive load ranges, also small load variations occurring between adjacent larger ranges. It might be thought that small load variations can be disregarded in view of a slight contribution to fatigue damage. A fundamental counting problem arises, if a small load variation occurs between larger peak values. This situation is illustrated in Fig. 6-6. Figure 6-6(a) illustrates a two-parameter range counting procedure will count the ranges AB, BC and CD, and store this information in a matrix. Now, consider the situation that the intermediate range BC was not occurred. Then, the large range AD would be counted only. Fatigue damage is related to load ranges, so it should be expected that the fatigue damage of the large range AD alone is larger than for the three separate ranges AB, BC and CD. The intermediate small load reversal BC is counted as a separate cycle and then removed from the major load range AD. This larger range can then is counted as separate load ranges followed Fig. 6-6(b). If four successive peak values are indicated by P_i, P_{i+1}, P_{i+2} and P_{i+3}, the rainflow count requirement for counting and removing a small range from a larger range is $P_{i+1} < P_{i+3}$ and $P_{i+2} > P_i$. If the intermediate small load reversal occurs in a descending load range followed Fig. 6-6(c), the requirement is $P_{i+1} > P_{i+3}$ and $P_{i+2} < P_i$.

(a) Range counts

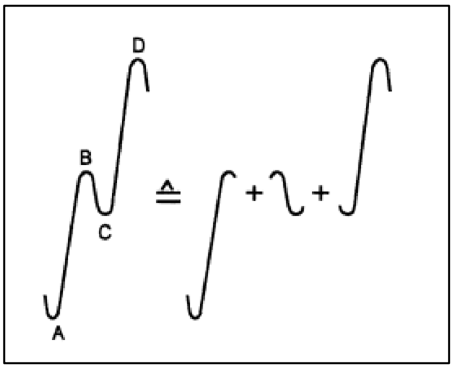

(b) Rainflow counts

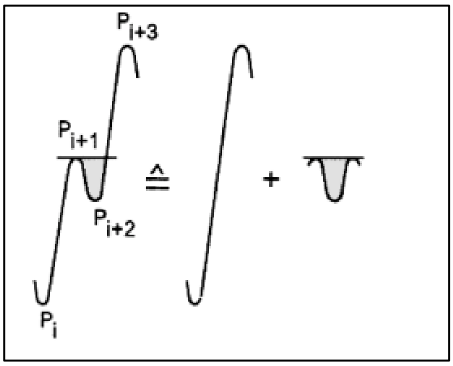

(c) Rainflow counts

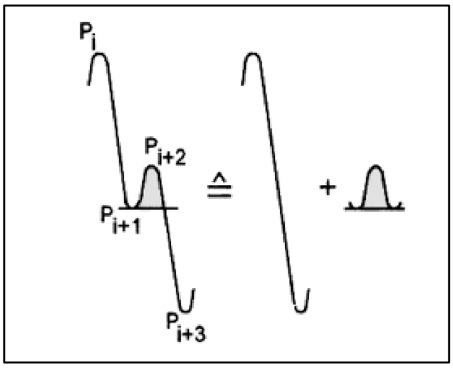

Fig. 6-6 Intermediate load reversal as part of a larger range.

The peak values of the intermediate small load reversal should be inside the range of the two peak values of the larger range. Successive rainflow counts are indicated in Fig. 6-7. Figure 6-7(a), five rainflow counts can be made. After counting and removing these small cycles which was obtained in Fig. 6-7(b). In this figure again three rainflow counts can be made, but now of larger ranges. Removing these cycles lead to Fig. 6-7(c), which again two still larger load reversals can be counted and removed. Finally, there are the residues; no further counts are possible as show in Fig. 6-7(d). The ranges of the residue must be counted separately at the end of the counting procedure.

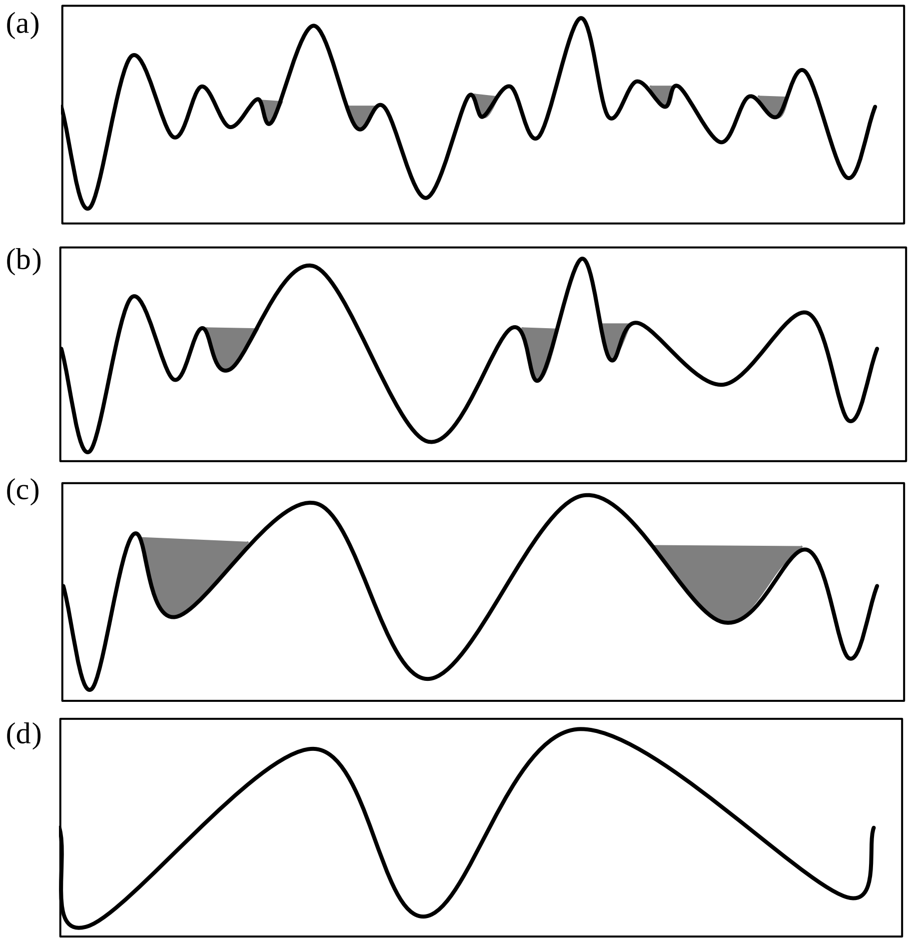

Fig. 6-7 Successive rainflow count: (a) 5 small cycles counted, (b) 3 cycle counted, (c) 2 cycles counted, (d) residue.

To replace a random loading spectrum by a set of complete stress-strain hysteresis loops, the actual strain course versus time is represented in a vertical way following to Fig. 6-8. Starting rain flows off all strain amplitudes as if they were roofs of a pagoda according to the following rules. The rain flow is stopped, (i) when it reaches a load value where the opposite load minimum falls below the starting minimum; that is, $|\varepsilon_H|$ is below $|\varepsilon_0|$. This mean that, rain flow coming from ε_0 is stopped at ε_G, (ii) when it reaches a load value where the opposite load maximum is higher than the starting maximum; that is, $|\varepsilon_T|$ is above $|\varepsilon_N|$. This mean that, rain flow coming from ε_M is stopped at ε_Q), or (iii) when it is interrupted by rain coming from the pagoda roof above, for the example, at ε_D or ε_R.

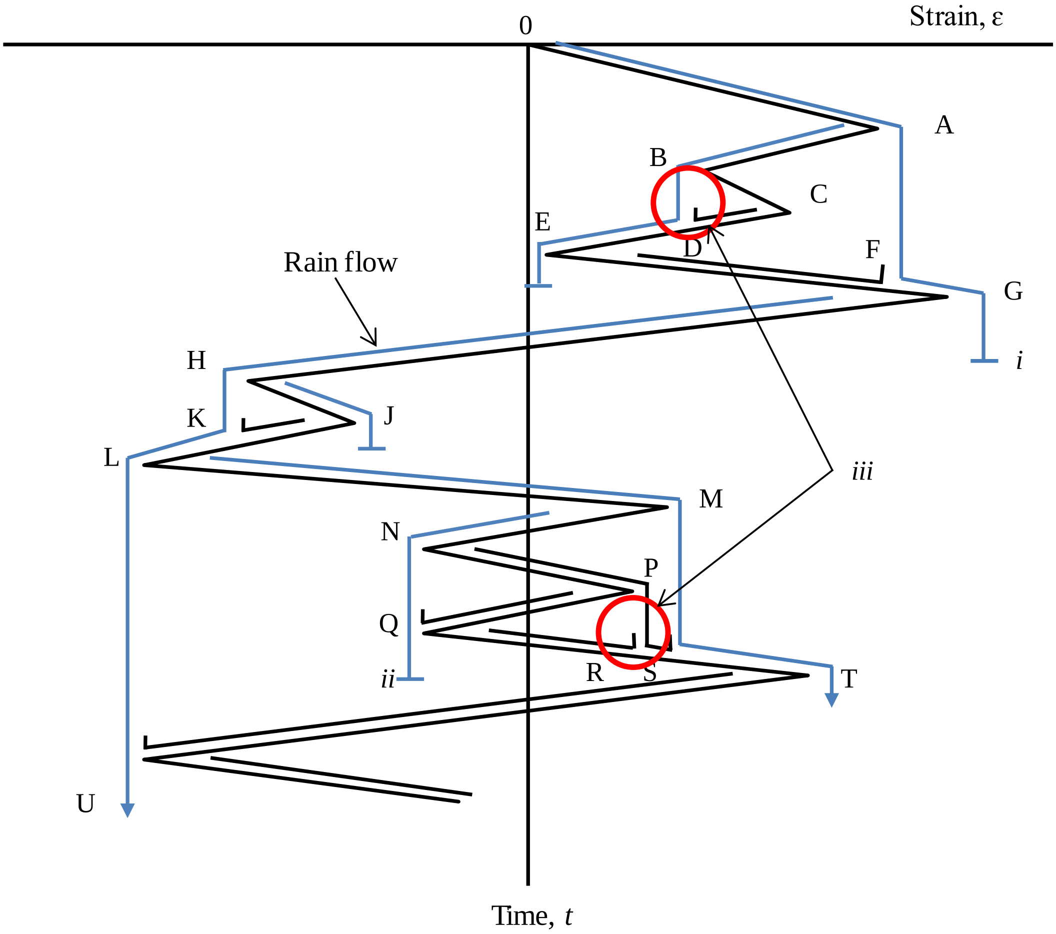

Fig. 6-8 Application of the rainflow counting method: Rainflow along a random loading spectrum.

By implementing these rules as computer algorithms in fatigue life assessment programs one can replace random loading spectra together with the experimental cyclic stress-strain curve stepwise as the hysteresis loops shown in Fig. 6-9. Only when a hysteresis loop is complete, it will be counted as one loading cycle of a certain class, corresponding to the partitioning of the loading spectrum. Again, these loading classes can be treated by the damage-accumulation approach after Palmgren and Miner. In several cases, 3-dimensional structural integrity problems should not be simplified by applying a uniaxial-loading approach, since real loading and damage conditions are determined by complex superimposition of cyclic torsion, bending and compression–tension. To treat such kinds of multiaxial fatigue, the concept of the critical plane has become established. The critical plane represents the areas where the service-life-relevant damage mechanisms are active, depending on the degree of exceeding of certain criteria that are defined by the mechanical load combination (normal and shear stresses within the critical plane).

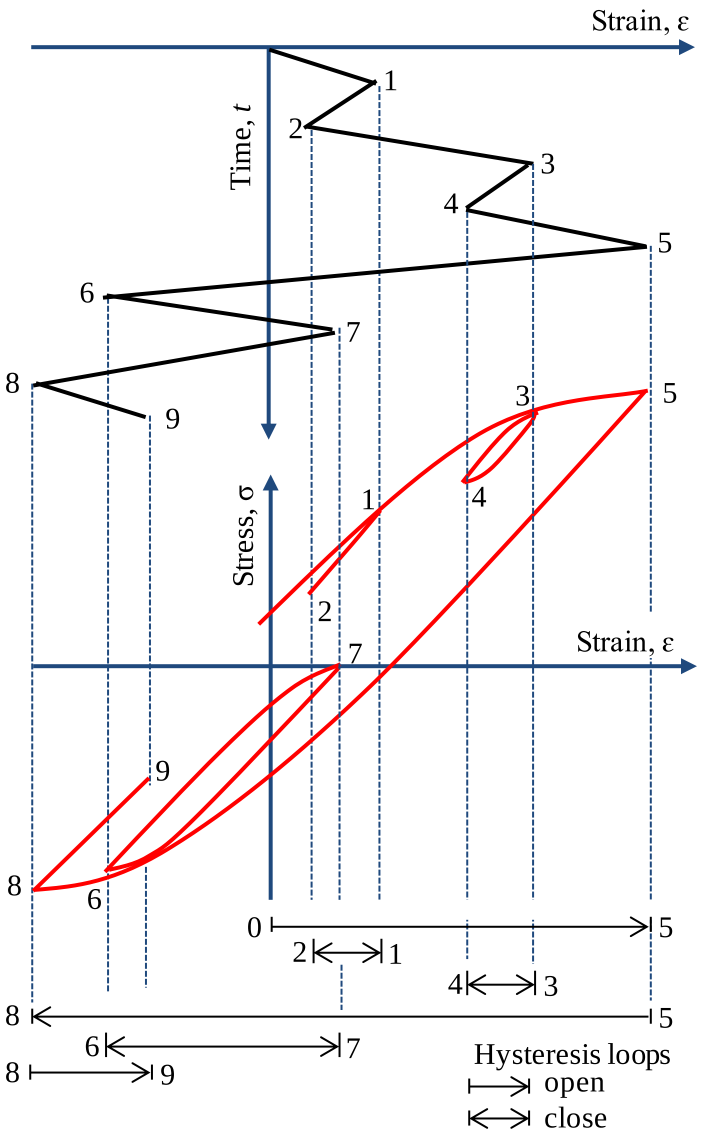

Fig. 6-9 Application of the rainflow counting method; Construction of stress–strain hysteresis loops

This chapter, the rainflow counting method was calculated using PROGRAM RAINFLOW which is complied under FORTRAN. Algorithm for rainflow counting method as followed;

1. Reduce the time history to a sequence of peaks (Tension) and troughs (Compression).

2. Imagine that the time history is a pagoda.
3. Turn the sheet clockwise 90°, so the starting time is at the top.
4. Each tensile peak is imagined as a source of water that drips down the pagoda.
5. Count the number of half-cycles by looking for terminations in the flow occurring when either:
    a) It reaches the end of the time history
    b) It merges with a flow that started at an earlier tensile peak; or
    c) It encounters a trough of greater magnitude.
6. Repeat step 5 for compressive troughs.
7. Assign a magnitude to each half-cycle equal to the stress difference between its start and termination.
8. Pair up half-cycles of identical magnitude (but opposite sense) to count the number of complete cycles. Typically, there are some residual half-cycles.

Figure 6-10 shows the code of PROGRAM RAINFLOW which is complied under FORTRAN programming language. The complied process uses the value at each reversal which is arranges the reversal from maximum value to maximum value or minimum value to maximum value in text file. The complied process followed Fig. 6-11. The input.txt file was added to code of program, complied on FORTRAN, and the output resulting with maximum value, minimum value, range, and mean.

```
 PROGRAM RAINFLOW

      PARAMETER (MX = 100)
      DIMENSION XLOAD(MX)


      OPEN(7,FILE='INPUT.D', STATUS = 'OLD')
      OPEN(8,FILE='OUTPUT.D')
      OPEN(9,FILE='XMAX.CSV')
      OPEN(10,FILE='XMIN.CSV')
      WRITE(8,250)
 250  FORMAT(5X,'"RANGE"',6X,'"MEAN"',7X,'"MAX."',8X,'"MIN."')
C
      READ(5,*) NUM ! Number of reversals in the load history
      DO 40 I = 1,NUM
      READ(7,*) XLOAD(I) ! Magnitude of the load
  40  CONTINUE
C
      NCOUNT = 0
      IPOS = 3
      DO WHILE (NUM.GE.3)
      IF (IPOS.LT.3) THEN
      IPOS = 3
      ENDIF
C

 DNOW = ABS(XLOAD(IPOS-1) - XLOAD(IPOS)) !abs(X)
      DPASS = ABS(XLOAD(IPOS-2) - XLOAD(IPOS-1)) !abs(Y)
C
      IF (DNOW.GE.DPASS) THEN
      XMEAN = (XLOAD(IPOS-2)+ XLOAD(IPOS-1))/2. !Mean load
      XRANGE = ABS(XLOAD(IPOS-2))- XLOAD(IPOS-1)) !Load range
      XMAX=XMEAN+XRANGE/2.0D0
      XMIN=XMEAN-XRANGE/2.0D0
      WRITE(8,260)XRANGE,XMEAN,XMAX,XMIN
      WRITE(9,270)XMAX
      WRITE(10.270)XMIN
 260  FORMAT(4(1X,F12.5))
 270 FORMAT(F12.5))
C
      DO 45 I = IPOS,NUM
      XLOAD(I-2) = XLOAD(I)
  45  CONTINUE
C
      NUM = NUM - 2
      IPOS = IPOS - 2
      NCOUNT = NCOUNT + 1
```

Fig. 6-10 Rainflow counting method program.

```
ELSE
IPOS = IPOS + 1
ENDIF
ENDDO
STOP
END
```

Fig. 6-10 Rainflow counting method program (continue).

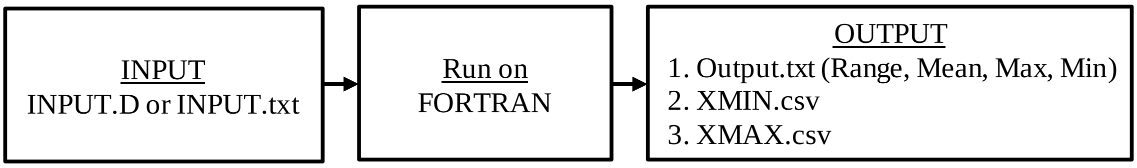

Fig. 6-11 Complied process for PROGRAM RAINFLOW.

The program is verified for accuracy by using the load-time history, as shows in an example of Fig. 6-12. The arrangement of reversals of the load-time history is 25, 5,-14, 16, 2, 7, -12, 25, that is, the reversals arranged with maximum value to maximum value as shows in Fig. 6-13(a). The calculated results listed in text file, as shown in Fig. 6-13(b). The results were compared with the results of the calculations by hand in Table 6-1. The results of both methods are the same. Therefore, programs that could be used in the calculation the rainflow counting method from actual experiment.

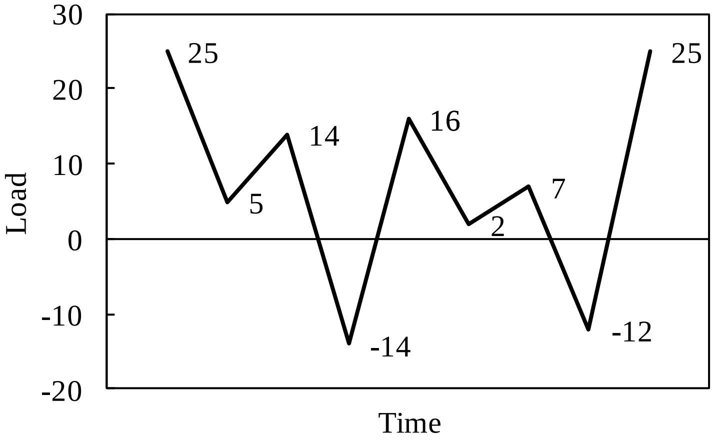

Fig. 6-12 Example of load-time history.

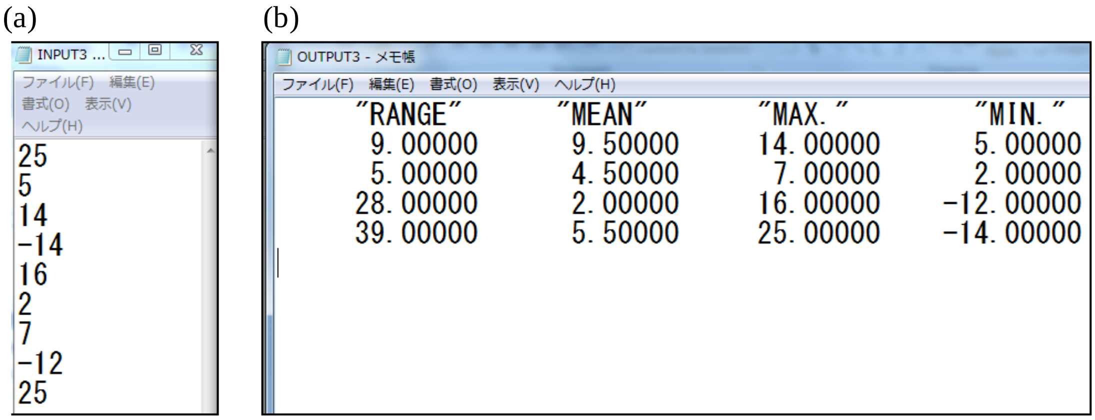

(a)

```
25
5
14
-14
16
2
7
-12
25
```

(b)

```
  "RANGE"       "MEAN"        "MAX."        "MIN."
   9.00000      9.50000     14.00000      5.00000
   5.00000      4.50000      7.00000      2.00000
  28.00000      2.00000     16.00000    -12.00000
  39.00000      5.50000     25.00000    -14.00000
```

Fig. 6-13 (a) Input: Reversal value in text file: (b) Output: Rainflow counted using PROGRAM RAINFLOW.

Table 6-1 Rainflow counted by hand calculation.

Cycle	Max.	Min.	Range	Mean
25-(-14)-25	25	-14	39	5.5
5-14-5	14	5	9	9.5
16-(-12)-16	16	-12	28	2
2-7-2	7	2	5	4.5

6.3 Results and discussion

6.3.1 Fatigue results under constant force amplitude with difference force ratios

In the automobiles, varied the force operated randomly in service, it has been thought that the force which has various a kind of force amplitude. Therefore, the fatigue tests were conducted under constant force amplitude with frequency of 5-10 Hz and difference force ratios *R* to consider the effect of the force ratio on the fatigue life. Fig. 6-14 shows the fatigue test results for three levels of the force ratios *R* of 0.01, 0.3 and 0.5. The results show that the fatigue life of each force ratio was slightly different with the same force amplitude level. Therefore, the various force ratios have no mean stress effect on the fatigue life.

For the random force amplitude fatigue test, the damage evaluation was conducted using the power regression equation which is obtained from *P*-*N* curve for the various force ratios. The regression equation was obtained on a log-log scale, as expressed by Eq. (6-7).

$$\log P_a = -0.321 \log N_f + 3.910 \tag{6-7}$$

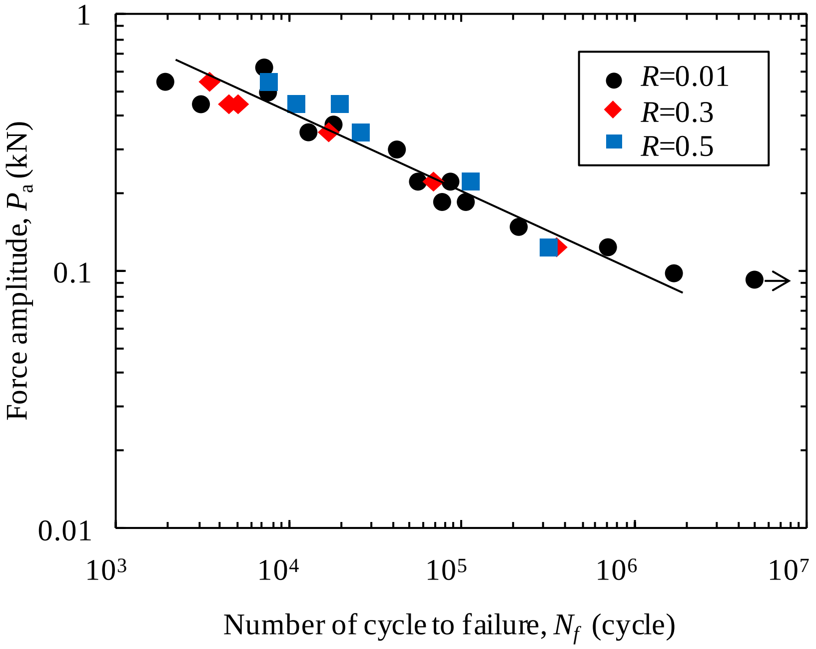

Fig. 6-14 Fatigue test results under constant force amplitude conditions with the various force ratios.

6.3.2 Fatigue damage under narrow band and broad band random force amplitude conditions

In this section, the fatigue tests were performed under random force amplitude to evaluate the cumulative fatigue damage. The both of bandwidth of the random force amplitude signal were obtained by digital simulation which simulated using the stationary Gaussian random process x(t), as described in Eq. 6-5. The waveform of random amplitude fatigue testing wave were applied to consider the force below 0.4 kN, which was no significant plastic deformation on the cumulative fatigue damage of the welded joints. The testing waveforms were the narrow band and broad band random force amplitude wave, which consisting the force amplitude both of above and below fatigue limit. The condition of both bandwidth random fatigue test is given in Table 6-2.

Table 6-2 The condition of random force amplitude waveform.

Waveform	Narrow band	Broad band
Frequency range (f_u-f_l)	1 Hz (6 to 7 Hz)	9 Hz (1 to 10 Hz)
Force range, ΔP	0.4 kN (0.0 to 0.4 kN)	0.4 kN (0.0 to 0.4 kN)
Duration time on 1 block	40 s	40 s

In this study, the frequency range speed effect on the fatigue crack growth is not almost appear, therefore, the conditions of bandwidth waveform having a uniform distribution with the frequency range of 1 Hz for narrow band waveform and 9 Hz for broad band waveform. Figure 6-15, and 6-16 show 3-types of the narrow band force amplitude and narrow band force amplitude waveforms, respectively. The random force amplitude wave was simulated to avoid applying compressive force to the welded joints during the fatigue test, this mean that the force ratio R was positive in all random fatigue tests.

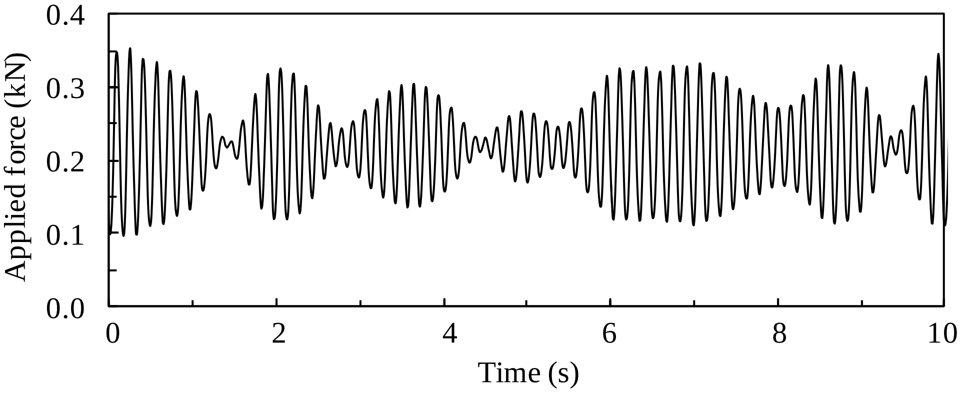

(a) Narrow band random waveform No. N1

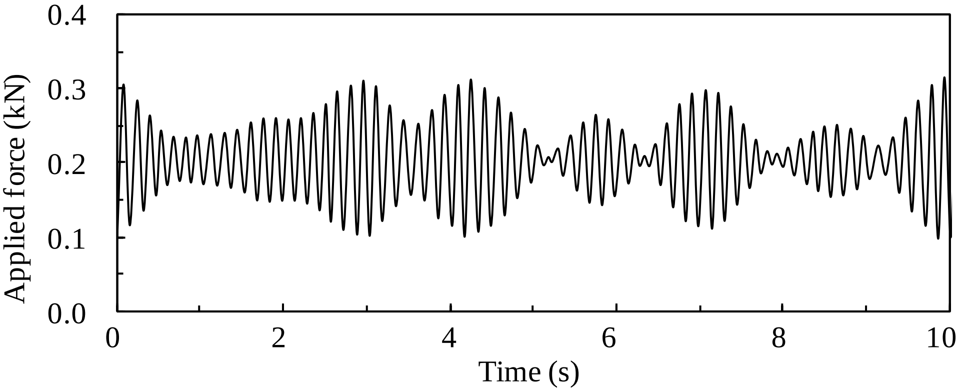

(b) Narrow band random waveform No. N2

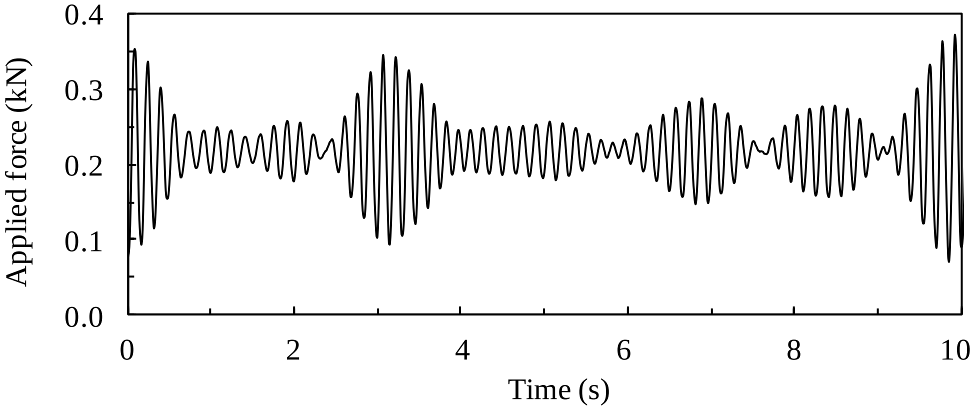

(c) Narrow band random waveform No. N3

Fig. 6-15 3-types of narrow band random force amplitudes for fatigue tests.

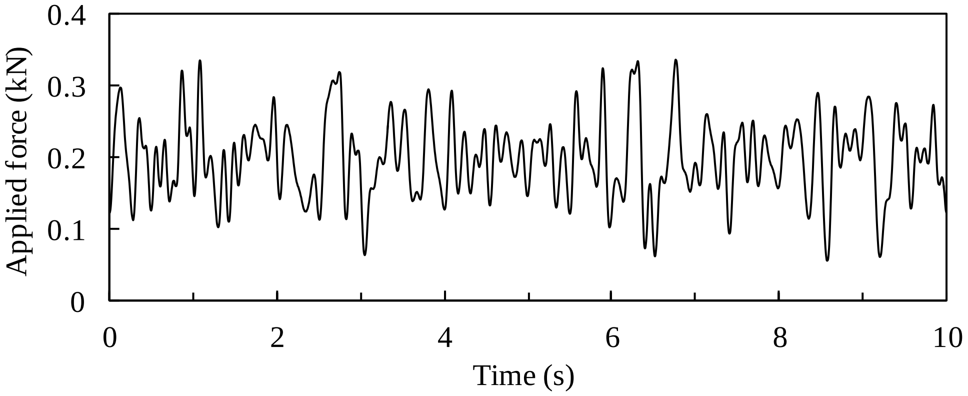

(a) Broad band random waveform No. B1

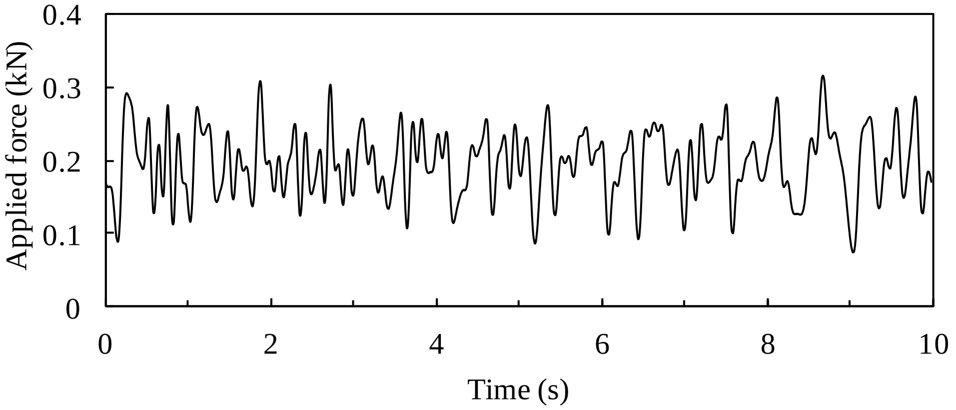

(b) Broad band random waveform No. B2

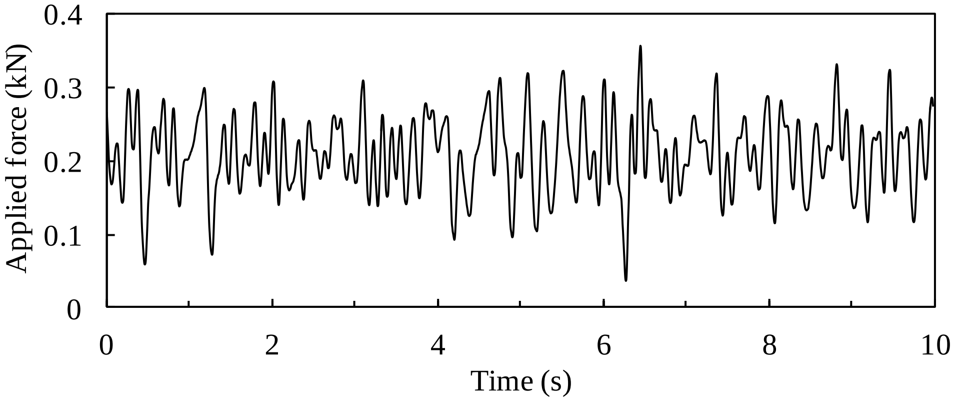

(c) Broad band random waveform No. B3

Fig. 6-16 3-types of broad band random force amplitudes for fatigue tests.

The cumulative fatigue damage were calculated by applied the rainflow cycle counting method for the applied force output from the load cell in testing machine, as mention above. When their force outputs were used to calculate the cumulative fatigue damage, the actual fatigue damage occurred at the location near the welded zone. Therefore, it is necessary to consider the behavior of the force output which was obtained from load cell corresponded with the local strain response near the welded zone in the order to conduct the evaluation of the cumulative fatigue damage.

The local strain was measured during the random force amplitude fatigue test by considering strain behavior. Two strain gages were attached 9 mm from the center of the welded zone in the longitudinal direction on the front side of the upper sheet, as show in Fig. 6-17. Figure 6-18 shows the result of the behavior of the average local strain value and applied force amplitude. In the figure, vertical axis indicates that the absolute value of the local strain which is obtained from the strain gage near the welded zone, to compare with the normalized by maximum value of the force output. The satisfaction of the method to applied the random force amplitude which is possible to conduct a precise evaluation of the cumulative fatigue damage on the welded joints by applying the rainflow counting method based on force output from the load cell. Therefore, the random fatigue test conducting the above mentioned test for several welded joints for different random amplitude waves, that the fatigue testing waves showed whole the same behavior.

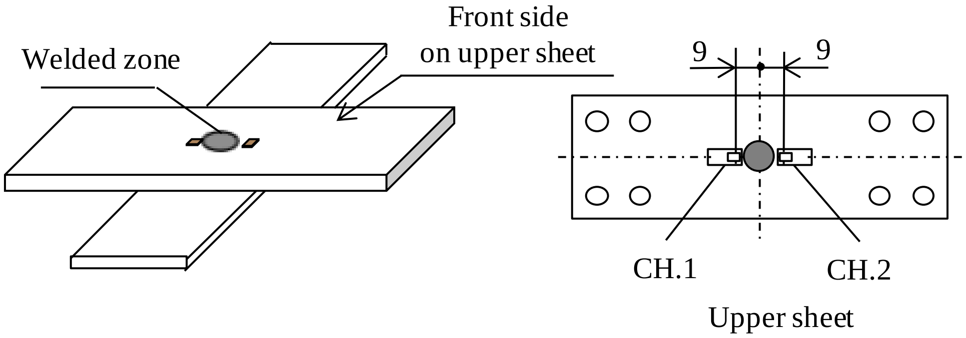

Fig. 6-17 Two strain gage locations on upper sheet of FSSW specimen.

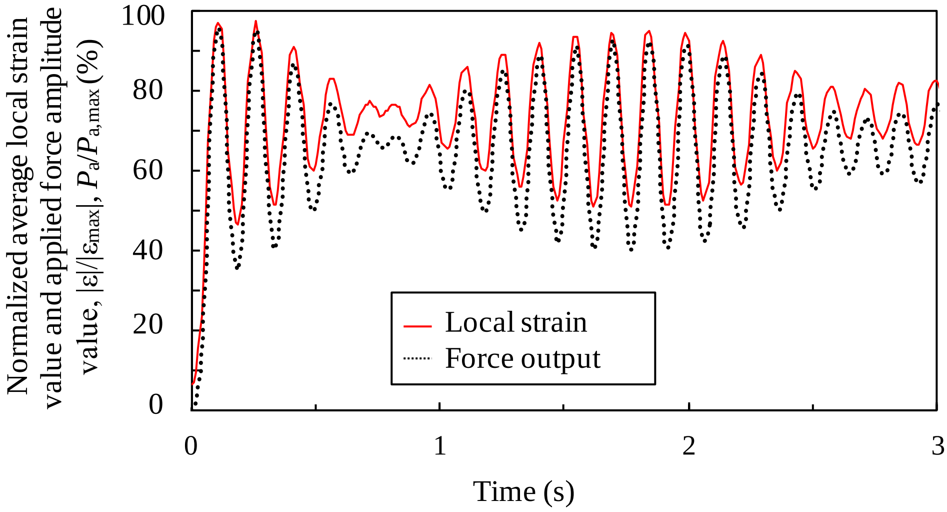

Fig. 6-18 Behavior of the average local strain value and applied force amplitude.

Tables 6-3 and 6-4 summarize the cumulative damage of the narrow band, and broad band random force amplitude fatigue test, respectively. The fatigue damage was estimated based on Miner' rule (D_M), which considers only the damage due to the force above the fatigue limit and modified Miner' rule (D_{MM}), which considers the damage due to the force both below and above the fatigue limit. The results show that the fatigue damage, D_M was extremely lower than unity, and D_{MM} was considerably low rather than unity for all specimens. The experimental results obtained using modified Miner's rule indicate that force below fatigue limit influence fatigue damage, such as the fatigue limit of the welded joint disappeared under the variable force amplitude conditions. In addition, the force amplitude distribution during random fatigue test was counted from the rainflow counting method, as shown in Figs. 6-19 and 6-20 for narrow band force amplitude waveform (specimen Nos. N1-N3) and broad band force amplitude waveform (specimen Nos. B1- B3), respectively. The results found that in the random waveform is included the cyclic numbers of force amplitude above fatigue limit approximately 10-15% of the total cyclic numbers for narrow band, and 3-7% of the total cyclic numbers for broad band.

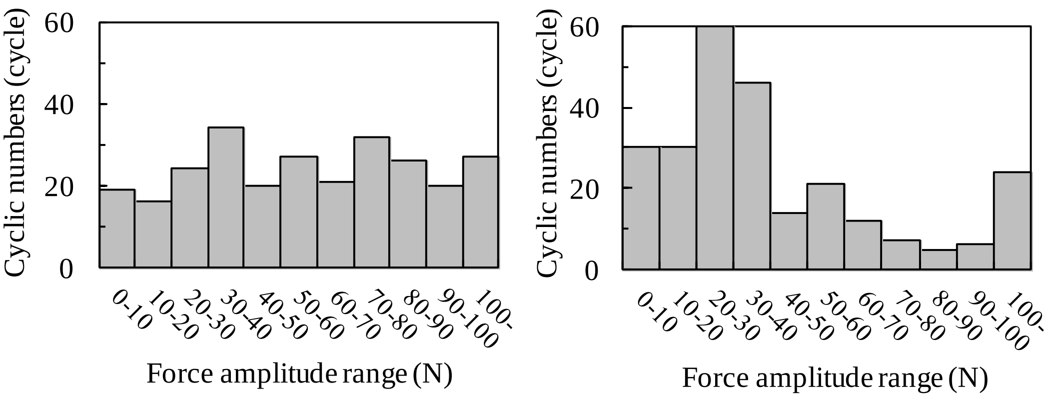

(a) Specimen N1

(b) Specimen N2

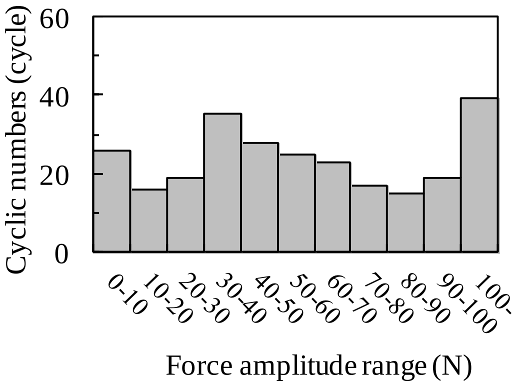

(c) Specimen N3

Fig. 6-19 Force amplitude distributions on the narrow band random force amplitude in a loop of random testing wave.

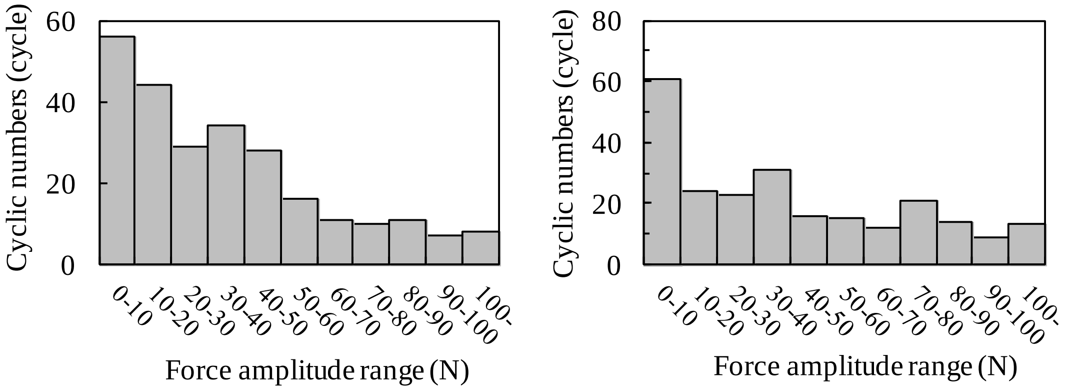

(a) Specimen B1 (b) Specimen B2

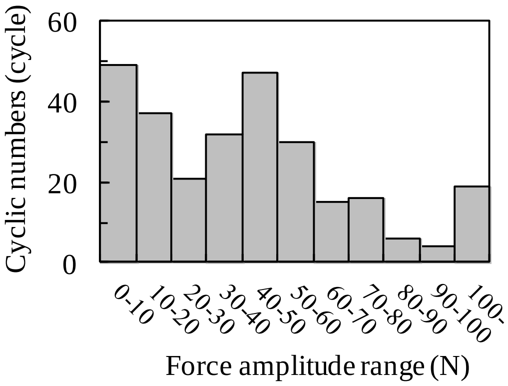

(c) Specimen B3

Fig. 6-20 Force amplitude distributions on the broad band random force amplitude in a loop of random testing wave.

Table 6-3 Results of cumulative damage under narrow band random force amplitude fatigue test.

Specimen No.	Force above fatigue limit (%)	D_M	D_{MM}
N1	10.1	0.19	0.54
N2	9.4	0.49	0.73
N3	14.9	0.28	0.49

Table 6-4 Results of cumulative damage under broad band random force amplitude fatigue test.

Specimen No.	Force above fatigue limit (%)	D_M	D_{MM}
B1	3.1	0.12	0.38
B2	5.4	0.25	0.67
B3	6.9	0.27	0.55

In the automobile industries, fatigue damage evolutions based on the linear cumulative fatigue damage rule variable range for strength design is generally from 0.5-2.0 [157]. These mean that the fatigue damage evaluation with the modified Miner's rule tends to underestimate the damage by applied random waveform which was include the force below fatigue limit, which yields an evaluation approaching on the dangerous side. As the results of the fatigue damage relatively low, this may be due to the effect of the frequency ratio between the cyclic numbers of force amplitude above and below fatigue limit. Therefore, in this chapter, the fatigue damage was re-evaluated using the modification method suggested by Corten-Dolan[182], [183] as discussed in section 6.3.3.

6.3.3 Effect of frequency ratio (Number of cycle fraction)

In this section, the modification method by Corten-Dolan's method [155], [183]–[186] were proposed. Corten and Dolan proposed the modified method by determining a damage line as shown in Fig. 6-21. The fatigue test under repeated two-step force amplitude was investigated for the effect of frequency ratio base on the results under constant force amplitude from previous study. Generally, mechanical component are stressed with variable stress during usage. Therefore, the stress must be classified by mean of counting methods. Furthermore, the parameter of the *S*-*N* curve must be known to calculate the fatigue life of the component. It should be noted that the *S*-*N* curve is given for a defined reliability statement. The fatigue life is given within a defined reliability statement when the each *S*-*N* curve indicated with difference reliability statement. The cumulative damage of the component caused by the applied force is generally calculated by the linear damage accumulative as mention in Chapter 5.

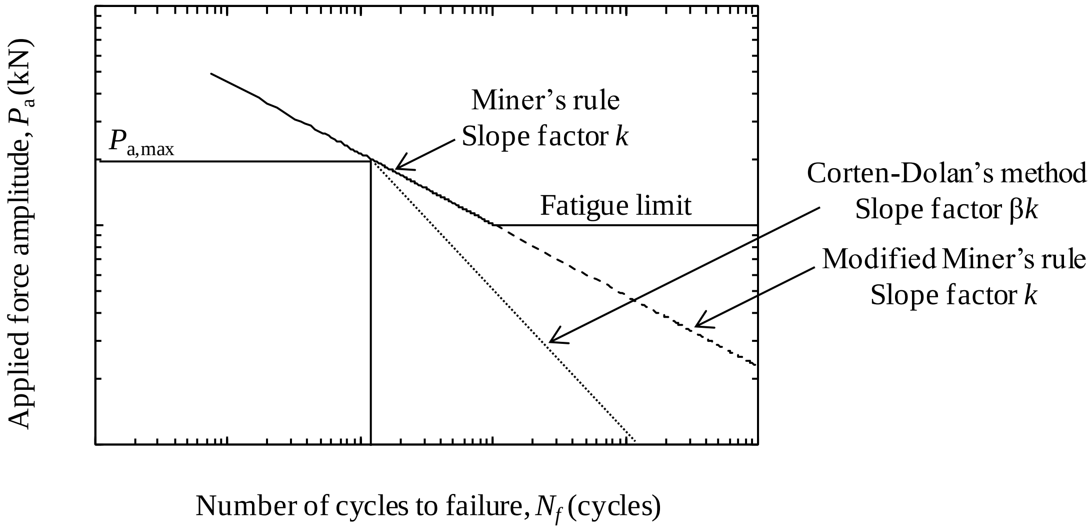

Fig. 6-21 Modification of *P*-*N* curve for Corten-Dolan's method.

The Corten-Dolan's method proposes a non-linear theory of cumulative damage, based on the number of nuclei (m) likely to be damage and on the velocity (r) of crack propagation. The accumulative damage on the stress level i is given by:

$$D_i = m_i r_i N_i^{a_i} \tag{6-8}$$

where, D is the damage, N is the applied cycle, a_i is an experimentally determined constant, and m and r are constants for given stress level. Damage to failure occurs for D=1. It is expressed as a function of the number of cycles according to:

$$D_i = \left({n_i}/{N_i} \right)^{a_i} \tag{6-9}$$

It is a about a law depending on the stress level with interaction. The effects of interaction are included in the concept of cracks. In the experiment, the cycle of maximum load is decisive for the initial damage since it determines the number of points where cracks will be formed. Once this number is established, one supposes that the propagation is carried out according to a cumulative process without interaction. With the following notation of α_i is percentage of cycles carried out at level σ_i, d is constant value, σ_1 is maximum amplitude of the sinusoidal stress for the fatigue life of N_1, and N_g is total number of cycles. The equation is given that:

$$\alpha_i N_g = n_i \tag{6-10}$$

By a process of summing damage increments, equating the total damage at failure in a constant amplitude test at σ_1 , and incorporating some simplifying assumptions based on numerous two-stress level block tests, the theory predicts the life N_g is given by:

$$N_g = \frac{N_1}{\alpha_i + (1-\alpha_i)(\sigma_2 / \sigma_1)^d} \tag{6-11}$$

Similarly, using these concepts and the assumptions stated earlier, Corten and Dolan developed an expression for estimating the number of cycles to failure for repeated blocks of many different stress levels as:

$$N_g = \frac{N_1}{\sum_{i=1}^{k} \alpha_i .(\sigma_2 / \sigma_1)^d} \tag{6-12}$$

This relationship, comparable with that of Freudenthal and Heller, can be reduced to that of Miner by using a modified fatigue curve which on *S-N* curve on log-log scale, intersects the *y*-axis at σ_1 and has a negative slope equal to 1/*d*. The equation of this curve is given:

$$N'\sigma^d = A \tag{6-13}$$

where N' is the fatigue life given by the modified curve. From Eq. (6-10), α_i can be substituted in Eq.(6-12) by taking account of Eq.(6-13), to calculate σ_1 and σ_i:

$$N_i'\sigma^d = N_1\sigma_1^d \tag{6-14}$$

where N_1=1,

$$N_g = \frac{N_1}{\sum_{i=1}^{k} (n_i / N_g)(\sigma_2 / \sigma_1)^d} = \frac{N_1}{\sum_{i=1}^{k} (n_i / N_g)(1/ N_1')} \tag{6-15}$$

yielding,

$$\sum_{i=1}^{k} n_i / N_i' = 1 \tag{6-16}$$

For comparison with Miner's rule, it is convenient to express as the follow failure of the component is assumed to occur when D=1. According to the Corten–Dolan's model, an experimental value of d must be obtained for each material of interest. The parameter d is interpreted as the inverse slope of a hypothetical S-N curve, which allows for the interaction between high and low stress levels.

This experimental method, the fatigue tests were performed under repeated two-step force amplitude. The waveform for the repeated two-step force amplitude is shown in Fig. 6-21. The waveform put a terminal point in the P-N curve at the maximum force amplitude which appears in the force output history of random force amplitude fatigue test as approximately 0.4 kN. The fatigue test were performed with the various the frequency ratio in 1 block (n_H/n_L) and the force ratio R approximately 0.01. Table 6-5 Show the results of the repeated two-step force amplitude fatigue tests and the fatigue life prediction for $P_L(N_f^*)$. A new linear damage line in the logarithm diagram is shown in Fig. 6-23.

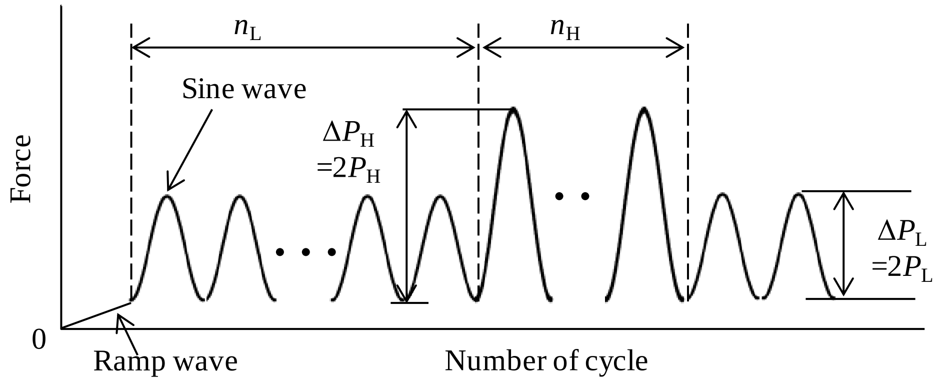

Fig. 6-22 Illustration of force amplitude wave form of repeated two-step force amplitude.

Table 6-5 Results of fatigue life prediction from the repeated two-step force amplitude.

Specimen No.	n_H/n_L (cycle/cycle)	ΔP_L (kN)	ΔP_H (kN)	N_f^* for P_L (cycle)
i	200/1000	0.10	0.39	2.07×10^6
ii	200/2000			2.07×10^6
iii	200/6000			8.42×10^6
iv	200/24000			2.89×10^7
v	200/24000			7.18×10^7
vi	200/1000	0.15	0.39	6.76×10^5
vii	200/2000			1.00×10^6
viii	200/6000			1.98×10^7
ix	200/6000			4.75×10^6

In the results as mention above, the random waveform is included the cyclic numbers of force amplitude above fatigue limit approximately 10–15% of the total cyclic numbers for narrow band frequency and 3-7% of the total cyclic numbers for broad band frequency. From Fig. 6-23, the frequency ratio was also suitable for evaluating the fatigue damage using Coten-Dolan's method which is n_H/n_L approximately 200/1000 and 200/2000 cycles. New linear damage line using Corten-Dolan damage method is expressed by Eq. (6-17)

$$\log P_a = -0.461 \log N_f + 4.605 \qquad (6\text{-}17)$$

The resulting cumulative damage D_{CD} determined by Corten-Dolan's method for the random force amplitude fatigue test of narrow band random force amplitude fatigue test (Specimen no. N1 to N3), and broad band random force amplitude fatigue test (Specimen no. B1 to B3) shown in Table 6-6. The results show that D_{CD} was approximately unity for each of the specimens. This is due to the fact that the damaging effect resulting from the number of cycles with a force below fatigue limit depends on the frequency ratio of the number of cycle with the force above the fatigue limit. The cumulative fatigue damage is affected by the frequency ratio of the force amplitude below the fatigue limit in the block of the random force amplitude wave. These experimental results implied that the proposed method can be applied for various kind of narrow band/broad band random force amplitude wave with the actual load component. Therefore, Corten-Dolan’s method yields an accurate evaluation for narrow band frequency, and broad band frequency, when the random force amplitude is performed a few number of cycles below fatigue limit, and considering the effect of frequency ratio is important in practical application when evaluating the fatigue characteristics of the welded joint under random force amplitude.

Table 6-6 Results of cumulative damage under narrow band, and broad band random force amplitude fatigue test with the modification of Corten-Dolan’s method.

Specimen No.	D_{M}	D_{MM}	D_{CD}
N1	0.19	0.54	1.28
N2	0.49	0.73	1.57
N3	0.28	0.49	1.04
B1	0.12	0.38	0.97
B2	0.25	0.67	1.59
B3	0.27	0.55	1.37

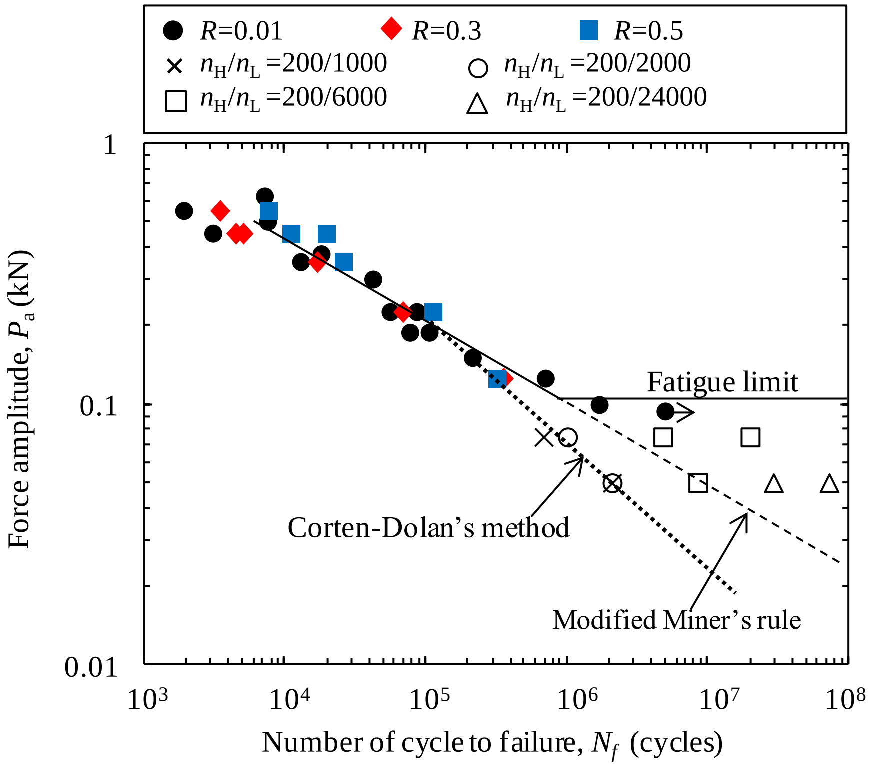

Fig. 6-23 Modified *P*-*N* curve using Corten-Dolan's method.

6.4 Conclusions

This chapter, the fatigue damage of FSSW cross-tension specimens under random force amplitude condition was investigated. Two kinds of difference bandwidth force amplitude history generated using the stationary Gaussian random process, having narrow band and broad band frequency content. The conclusions obtained are as follows.

1. The various force ratios have no mean stress effect on the fatigue life of the welded joints. Therefore, it was possible to consider the cumulative damage by the rainflow counting method.
2. The fatigue damage evaluation with the modified Miner's rule tends to underestimate the damage by applied random wave form which was include the force below fatigue limit, which yields an evaluation approaching on the dangerous side. However, the modification of fatigue damage using Corten-Dolan's method has been the results are satisfactory and the frequency ratio affects the evaluation of damage, and the frequency ratio to the suitable for consideration the fatigue damage is approximately 5-10 times. By considering the cumulative fatigue damage evaluation base on Corten-Dolan's method, it was possible to evaluate the fatigue life of the FSSW joints under random force amplitude conditions, which appropriated the strength designed range to considerable attention in the automotive industry.

CHAPTER 7

Conclusions

This chapter has presented the conclusions of the present work, including of Chapter 4, Chapter 5, and Chapter 6 for the fatigue tests under constant, repeated two-step and random force amplitude condition, respectively. Subsequently, the recommendations for future work are proposed in the end of this chapter.

First, the mechanical properties and fatigue crack growth behavior of the FSSW cold rolled-carbon steel joints was investigated under constant force amplitude. The low temperature friction stir welding of steels was observed around 973 K, which should be the first example of welding general steels without any transformation. In addition, the control of the temperature enabled the steels to be welded in various regions, such as the α-γ two-phase region and the γ single-phase region. From this work, the following conclusions were achieved. It has observed that the relationship between the peak temperature and the A_1 point. When the FSSW is performed in the α-γ two-phase region, the microstructure is refined and the highest hardness is then achieved. The hardness of the welded area was hardening occurred up to 60% relative to the base metal. This was caused by the generation of extremely fine grains and pearlite phase structure in the SZ and TMAZ, and the impulse compressive force from the welding process.

The specimen used for this study had a fatigue limit of 0.1 kN. This value is very low compared with the maximum tensile force of the base metal and FSSW joint itself. The crack initiation occurred at a boundary between the welding interface zone and non-interface zone or slit tip regardless of amplitude level. In addition, the slit tip is located in the heat affected zones. The fatigue crack was found on the upper sheet at the distal slit through to the surface of sheet up to the concave zone. The fracture morphology is the mixed mode fracture. Therefore, fatigue fracture modes were independent on force amplitude level.

Base on the 3-dimensional observation, the macroscopic fracture modes were independent on the force amplitude. The fatigue initiation life was dependent on the force amplitude. In other words, the fatigue crack initiation life under low force amplitude accounted for a comparatively large proportion of the entire fatigue life; whereas the fatigue cracks initiation life occurred in a relatively early stage under high force amplitude.

Next, the fatigue damage of FSSW specimens under two-step force amplitude conditions was investigated. Two cases were considered: in the first, macroscopic plastic deformation near the welded zone did not occur, and in the second, significant plastic deformation occurred. The conclusions obtained are as follows.

In fatigue tests with repeated two-step force amplitude, the fatigue limit of the welded joint disappeared. However, the fatigue damage evaluation using the modified Miner’s rule erred too much on the side of safety, as the modified Miner’s rule tends to overestimate the damage by applied forces below the fatigue limit. Thus, it was determined that, within the testing conditions used in this study, the fatigue damage evaluation using Haibach’s method yielded an accurate evaluation. In the case where significant plastic deformation caused by the applied force occurred near the welded zone, the cumulative fatigue damage value based on Miner’s rule was often larger than unity. Therefore, it is important to consider a cumulative damage estimation that takes into account the effect of pre-strain from the high force amplitude.

Finally, the fatigue damage of FSSW cross-tension specimens under random force amplitude condition was investigated. Two kinds of difference bandwidth force amplitude history generated using the stationary Gaussian random process, having narrow band and broad band frequency content. The conclusions obtained are as follows.

The various force ratios have no mean stress effect on the fatigue life of the welded joints. Therefore, it was possible to consider the cumulative damage by the rainflow counting method. The fatigue damage evaluation with the modified Miner’s rule tends to underestimate the damage by applied random wave form which was include the force below fatigue limit, which yields an evaluation approaching on the dangerous side. However, the modification of fatigue damage using Corten-Dolan’s method has been the results are satisfactory and the frequency ratio affects the evaluation of damage, and the frequency ratio to the suitable for consideration the fatigue damage is approximately 5-10 times. By considering the cumulative fatigue damage evaluation base on Corten-Dolan’s method, it was possible to evaluate the fatigue life of the FSSW joints under random force amplitude conditions, which appropriated the strength designed range to considerable attention in the automotive industry.

The recommendations for future work on this particular study as followed:

As an experiment had already determined the fatigue damage under repeated two-step force amplitude condition with the case of the external force less than 0.4 kN which is the plastic deformation not occurred. The results of pre-strain fatigue test as shown in Fig. 7-1. The results shown that when both of external force more than 0.4 kN, the fatigue life was not extended. In order to further understand the occurrence of the effect of plastic deformation. It is interest to evaluate the fatigue damage under repeated two-step force amplitude condition with the both of external force level.

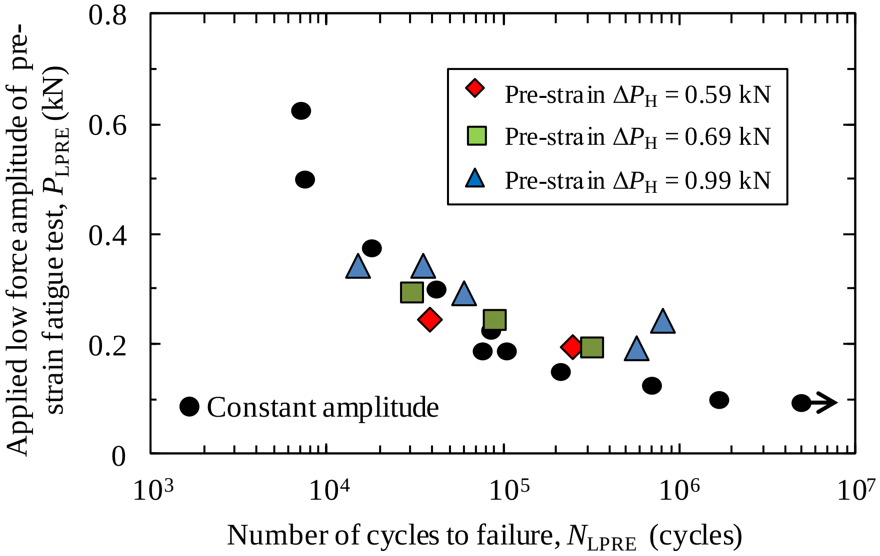

Fig. 7-1 Results of fatigue3 test under pre-strain and constant force amplitude.

Also the experiment had already determined the fatigue damage under random force amplitude condition with the force range of 0.4 kN (0 to 0.4 kN) which is the plastic deformation not occurred. Since the plastics deformation was occurred and affects to extend the fatigue life, then it is important to study the effect of the plastic deformation resulting to the fatigue damage and including to the strain behavior during the fatigue tests.

With the complex crack propagation, FEM was simulated to calculate the strain behavior in the welded joint. This approach is benefit to practically predict the fatigue crack behavior. In future studies, in order to further understand the initiation and propagation of fatigue crack in FSSW specimen, especially in cross-tension specimen, the FEM approach should be improved to predict crack behavior.

Finally, in practical application, a lot of joints are applied not only shear loading but also tension, bending, and torsion loading. For example, FSSW has been applied to the rear door panel in automobile body. Therefore, it is important to consider the fatigue properties on each mode of loading. And, this method is benefit to compare the fatigue damage evaluation with other welding method.

REFERENCES

[1] O. Humlum, K. Stordahl, and J. E. Solheim, The phase relation between atmospheric carbon dioxide and global temperature, *Glob. Planet. Change*, vol. 100, pp. 51–69, 2013.

[2] C. Gu, J. Crane, G. Hornberger, and A. Carrico, The effects of household management practices on the global warming potential of urban lawns, *J. Environ. Manage.*, vol. 151, pp. 233–242, 2015.

[3] E. Ahmadi Moghaddam, S. Ahlgren, C. Hulteberg, and Å. Nordberg, Energy balance and global warming potential of biogas-based fuels from a life cycle perspective, *Fuel Process. Technol.*, vol. 132, pp. 74–82, 2015.

[4] S. L. D. Paiva, M. a. Savi, F. M. Viola, and A. J. K. Leiroz, Global warming description using Daisyworld model with greenhouse gases, *Biosystems*, vol. 125, pp. 1–15, 2014.

[5] L. Meier, R. Pérez, L. Azócar, M. Rivas, and D. Jeison, Photosynthetic CO2 uptake by microalgae: An attractive tool for biogas upgrading, *Biomass and Bioenergy*, vol. 73, pp. 102–109, 2015.

[6] E. Bayraktar, Introduction to welding and bonding technologies, in Comprehensive materials processing, Elsevier, pp. 1–2, 2014.

[7] M. Vural, Welding processes and technologies, in Comprehensive materials processing,

Elsevier, pp. 3–48, 2014.

[8] E. Tempelman, H. Shercliff, and B. N. Van Eyben, Joining and assembly, in Manufacturing and design, Elsevier, pp. 201–226, 2014.

[9] K. G. Swift and J. D. Booker, Joining processes, in Manufacturing process selection handbook, Elsevier, pp. 291–349, 2013.

[10] M. Ashby and K. Johnson, Manufacturing: Shaping, joining, and surfaces, in materials and design, Elsevier, pp. 100–109, 2014.

[11] M. Shome and M. Tumuluru, Introduction to welding and joining of advanced high-strength steels (AHSS), in Welding and Joining of Advanced High Strength Steels (AHSS), Elsevier, pp. 1–8, 2015.

[12] P. Heurtier, M. J. Jones, C. Desrayaud, J. H. Driver, F. Montheillet, and D. Allehaux, Mechanical and thermal modelling of Friction Stir Welding, *J. Mater. Process. Technol.*, vol. 171, no. 3, pp. 348–357, 2006.

[13] Y. F. Sun and H. Fujii, Investigation of the welding parameter dependent microstructure and mechanical properties of friction stir welded pure copper, *Mater. Sci. Eng. A*, vol. 527, no. 26, pp. 6879–6886, 2010.

[14] H. T. Hsieh and J. L. Chen, Using TRIZ methods in friction stir welding design, *Int. J. Adv. Manuf. Technol.*, vol. 46, no. 9–12, pp. 1085–1102, 2009.

[15] R. John, K. V Jata, and K. Sadananda, Residual stress effects on near-threshold fatigue crack growth in friction stir welds in aerospace alloys, *Int. J. Fatigue*, vol. 25, no. 9–11, pp. 939–948, 2003.

[16] S. Vijayan, R. Raju, K. Subbaiah, N. Sridhar, and S. R. K. Rao, Friction Stir Welding of Al-Mg Alloy Optimization of Process Parameters Using Taguchi Method, *Soc. Exp. Tech.*, vol. 34, no. 5, pp. 37–44, 2010.

[17] G. M. Xie, Z. Y. Ma, and L. Geng, Development of a fine-grained microstructure and the properties of a nugget zone in friction stir welded pure copper, *Scr. Mater.*, vol. 57, no. 2, pp. 73–76, 2007.

[18] Z. Zhang and H. W. Zhang, A fully coupled thermo-mechanical model of friction stir welding, *Int. J. Adv. Manuf. Technol.*, vol. 37, no. 3–4, pp. 279–293, 2007.

[19] J. D. Costa, J. A. M. Ferreira, and L. P. Borrego, Influence of spectrum loading on fatigue resistance of AA6082 friction stir welds, *Int. J. Struct. Integr.,* vol. 2, no. 2, pp. 122–134, 2011.

[20] S. J. Barnes, a. Steuwer, S. Mahawish, R. Johnson, and P. J. Withers, Residual strains and microstructure development in single and sequential double sided friction stir welds in RQT-701 steel, *Mater. Sci. Eng. A*, vol. 492, no. 1–2, pp. 35–44, 2008.

[21] S. H. Aldajah, O. O. Ajayi, G. R. Fenske, and S. David, Effect of friction stir processing on the tribological performance of high carbon steel, *Wear*, vol. 267, no. 1–4, pp. 350–355, 2009.

[22] P. L. Threadgill, A. J. Leonard, H. R. Shercliff, and P. J. Withers, Friction stir welding of aluminium alloys, *Int. Mater. Rev.*, vol. 54, no. 2, pp. 49–93, 2009.

[23] M. P. Miles, J. Pew, T. W. Nelson, and M. Li, Comparison of formability of friction stir welded and laser welded dual phase 590 steel sheets, *Sci. Technol. Weld. Join.*, vol. 11, no. 4, pp. 384–388, 2006.

[24] T. Li, Q. Y. Shi, and H.-K. Li, Residual stresses simulation for friction stir welded joint, *Sci. Technol. Weld. Join.,* vol. 12, no. 8, pp. 664–670, 2007.

[25] R. S. Mishra and Z. Y. Ma, Friction stir welding and processing, *Mater. Sci. Eng. R Report*s, vol. 50, no. 1–2, pp. 1–78, 2005.

[26] Y.-C. Chiou, C.-T. Liu, and R.-T. Lee, A pinless embedded tool used in FSSW and FSW

of aluminum alloy, *J. Mater. Process. Technol.*, vol. 213, no. 11, pp. 1818–1824, 2013.

[27] V. Malik, N. K. Sanjeev, H. S. Hebbar, and S. V. Kailas, Investigations on the effect of various tool pin profiles in friction stir welding using finite element simulations, *Procedia Eng.*, vol. 97, pp. 1060–1068, 2014.

[28] V. Malik, N. . Sanjeev, H. S. Hebbar, and S. V. Kailas, Time efficient simulations of plunge and dwell phase of FSW and its significance in FSSW, *Procedia Mater. Sci.*, vol. 5, pp. 630–639, 2014.

[29] G. Buffa, P. Fanelli, L. Fratini, and F. Vivio, Influence of joint geometry on micro and macro mechanical properties of friction stir spot welded joints, *Procedia Eng.*, vol. 81, pp. 2086–2091, 2014.

[30] M. K. Bilici and A. İ. Yükler, Influence of tool geometry and process parameters on macrostructure and static strength in friction stir spot welded polyethylene sheets, *Mater. Des.*, vol. 33, pp. 145–152, 2012.

[31] H.-S. Shin, Tool geometry effect on the characteristics of dissimilar friction stir spot welded bulk metallic glass to lightweight alloys, *J. Alloys Compd.*, vol. 586, pp. S50–S55, 2014.

[32] A. Meilinger and I. Torok, The importance of friction stir welding tool, *Prod. Process. Syst.*, vol. 6, no. 1, pp. 25–34, 2013.

[33] M. Shiraly, M. Shamanian, M. R. Toroghinejad, and M. Ahmadi Jazani, Effect of tool rotation rate on microstructure and mechanical behavior of friction stir spot-welded Al/Cu composite, *J. Mater. Eng. Perform.*, vol. 23, no. 2, pp. 413–420, 2014.

[34] Z. Y. Ma, Friction stir processing technology: A review, *Metall. Mater. Trans. A*, vol. 39, no. 3, pp. 642–658, 2008.

[35] C. Jonckheere, B. Meester, C. Cassiers, M. Delhaye, and A. Simar, Fracture and

mechanical properties of friction stir spot welds in 6063-T6 aluminum alloy, *Int. J. Adv. Manuf. Technol.*, vol. 62, no. 5–8, pp. 569–575, 2011.

[36] M. Ghosh, K. Kumar, and R. S. Mishra, Analysis of microstructural evolution during friction stir welding of ultrahigh-strength steel, *Scr. Mater.*, vol. 63, no. 8, pp. 851–854, 2010.

[37] D.-A. Wang and S.-C. Lee, Microstructures and failure mechanisms of friction stir spot welds of aluminum 6061-T6 sheets, *J. Mater. Process. Technol.*, vol. 186, no. 1–3, pp. 291–297, 2007.

[38] S. J. Maddox, Fatigue design rules for welded structures, *Prog. Struct. Engineering Mater.*, vol. 2, pp. 102–109, 2000.

[39] S. Lathabai, Joining of aluminium and its alloys, in Fundamentals of aluminium metallurgy: Production, processing and applications, Elsevier, pp. 607–654, 2011.

[40] R. Hancock, Friction welding of aluminum cuts energy costs by 99%, *Weld. J. (Miami, Fla)*, vol. 83, no. 2, pp. 40, 2004.

[41] M. Awang, V. H. Mucino, Z. Feng, and S. A. David, FSSW Process : Use of an Explicit Adaptive Meshing Scheme, *SAE International*, 2005–01–1251, 2005.

[42] Q. Yang, S. Mironov, Y. S. Sato, and K. Okamoto, Material flow during friction stir spot welding, *Mater. Sci. Eng. A*, vol. 527, no. 16–17, pp. 4389–4398, 2010.

[43] Y. Hovanski, M. L. Santella, and G. J. Grant, Friction stir spot welding of hot-stamped boron steel, *Scr. Mater.*, vol. 57, no. 9, pp. 873–876, 2007.

[44] S.-W. Baek, D.-H. Choi, C.-Y. Lee, B.-W. Ahn, Y.-M. Yeon, K. Song, and S.-B. Jung, Structure–properties relations in friction stir spot welded low carbon steel sheets for light weight automobile body, *Mater. Trans.*, vol. 51, no. 2, pp. 399–403, 2010.

[45] Y. W. Lee, M. A. M. Hossain, S. T. Hong, Y. J. Yum, and K. Y. Park, Characterization of

friction stir spot welding of aluminum alloys using acoustic emissions, in *Proceedings of the International Offshore and Polar Engineering Conference*, pp. 527–529, 2011.

[46] A. M. S. Malafaia, M. T. Milan, M. F. Oliveira, and D. Spinelli, Fatigue behavior of friction stir spot welding and riveted joints in an Al alloy, *Procedia Eng.*, vol. 2, pp. 1815–1821, 2010.

[47] H. Badarinarayan, Q. Yang, and S. Zhu, Effect of tool geometry on static strength of friction stir spot-welded aluminum alloy, *Int. J. Mach. Tools Manuf.*, vol. 49, no. 2, pp. 142–148, 2009.

[48] S. Bozzi, A. L. Helbert-Etter, T. Baudin, V. Klosek, J. G. Kerbiguet, and B. Criqui, Influence of FSSW parameters on fracture mechanisms of 5182 aluminium welds, *J. Mater. Process. Technol.*, vol. 210, no. 11, pp. 1429–1435, 2010.

[49] W. M. U. Thomas and E. D. Nicholas, Friction stir welding for the transportation industries, *Mater. Des.*, vol. 18, no. 4/6, pp. 269–273, 1997.

[50] R. Nandan, T. Debroy, and H. Bhadeshia, Recent advances in friction-stir welding - process, weldment structure and properties, *Prog. Mater. Sci.*, vol. 53, no. 6, pp. 980–1023, 2008.

[51] W.-B. Lee and S.-B. Jung, The joint properties of copper by friction stir welding, *Mater. Lett.*, vol. 58, no. 6, pp. 1041–1046, 2004.

[52] S. Venukumar, S. Muthukumaran, S. G. Yalagi, and S. V. Kailas, Failure modes and fatigue behavior of conventional and refilled friction stir spot welds in AA 6061-T6 sheets, *Int. J. Fatigue*, vol. 61, pp. 93–100, 2014.

[53] P. Lin, J. Pan, and T. Pan, Failure modes and fatigue life estimations of spot friction welds in lap-shear specimens of aluminum 6111-T4 sheets. Part 1: Welds made by a concave tool, *Int. J. Fatigue*, vol. 30, no. 1, pp. 74–89, 2008.

[54] P. Lin, J. Pan, and T. Pan, Failure modes and fatigue life estimations of spot friction welds in lap-shear specimens of aluminum 6111-T4 sheets. Part 2: Welds made by a flat tool, *Int. J. Fatigue*, vol. 30, pp. 90–105, 2008.

[55] S. Babu, V. S. Sankar, G. D. Janaki Ram, P. V. Venkitakrishnan, G. Madhusudhan Reddy, and K. Prasad Rao, Microstructures and mechanical properties of friction stir spot welded aluminum alloy AA2014, *J. Mater. Eng. Perform.*, vol. 22, no. 1, pp. 71–84, 2012.

[56] Z. Feng, M. L. Santella, S. A. David, R. J. Steel, S. M. Packer, T. Pan, M. Kuo, and R. S. Bhatnagar, Friction stir spot welding of advanced high-strength steels-A feasibility study, *SAE International*, pp. 2005–01–1248, 2005.

[57] Z. Shen, X. Yang, S. Yang, Z. Zhang, and Y. Yin, Microstructure and mechanical properties of friction spot welded 6061-T4 aluminum alloy, *Mater. Des.*, vol. 54, pp. 766–778, 2014.

[58] Y. Uematsu, K. Tokaji, Y. Tozaki, and Y. Nakashimac, Fatigue behaviour of dissimilar friction stir spot weld between A6061 and SPCC welded by a scrolled groove shoulder tool, *Procedia Eng.*, vol. 2, no. 1, pp. 193–201, 2010.

[59] S. G. Arul, S. F. Miller, G. H. Kruger, T.-Y. Pan, P. K. Mallick, and a. J. Shih, Experimental study of joint performance in spot friction welding of 6111-T4 aluminium alloy, *Sci. Technol. Weld. Join.*, vol. 13, no. 7, pp. 629–637, 2008.

[60] P. L. Moore and G. Booth, The Welding Engineer’s Guide to Fracture and Fatigue. Woodhead Publishing Limited, 2015.

[61] J. Schijve, Fatigue of Structures and Materials, 2nd ed. Springer, 2009.

[62] D. H. Kang, C. Jang, Y. S. Park, S. Y. Han, and J. H. Kim, Fatigue reliability assessment of steel member using probabilistic stress-life method, *Adv. Mech. Eng.*, vol. 2012, 2012.

[63] H. Fujii, Y. Sun, and H. Kato, Microstructure and mechanical properties of friction stir

welded pure Mo joints, *Scr. Mater.*, vol. 64, no. 7, pp. 657–660, 2011.

[64] M. S. Khorrami, M. Kazeminezhad, and a. H. Kokabi, Mechanical properties of severely plastic deformed aluminum sheets joined by friction stir welding, *Mater. Sci. Eng. A*, vol. 543, pp. 243–248, 2012.

[65] R. Sołtysiak, Local strain analysis in friction stir welded 2024-T3 aluminium joint under ciclic loading, *J. Polish Cimac*, vol. 5, no. 3, pp. 187–192, 2010.

[66] D. Boroński, R. Sołtysiak, and Z. Lutowski, Analysis of strain distribution in notch zone in aluminium FSW joints for irregular fatigue loading conditions, *Solid State Phenom.*, vol. 224, pp. 27–32, 2015.

[67] V. Tran, J. Pan, and T. Pan, Fatigue behavior of aluminum 5754-O and 6111-T4 spot friction welds in lap-shear specimens, *Int. J. Fatigue*, vol. 30, no. 12, pp. 2175–2190, 2008.

[68] Y. D. Chung, H. Fujii, R. Ueji, and N. Tsuji, Friction stir welding of high carbon steel with excellent toughness and ductility, *Scr. Mater.*, vol. 63, no. 2, pp. 223–226, 2010.

[69] Y. S. Sato, H. Yamanoi, H. Kokawa, and T. Furuhara, Microstructural evolution of ultrahigh carbon steel during friction stir welding, *Scr. Mater.*, vol. 57, no. 6, pp. 557–560, 2007.

[70] L. Cui, H. Fujii, N. Tsuji, and K. Nogi, Friction stir welding of a high carbon steel, *Scr. Mater.*, vol. 56, no. 7, pp. 637–640, 2007.

[71] J. D. Costa, J. A. M. Ferreira, L. P. Borrego, and L. P. Abreu, Fatigue behaviour of AA6082 friction stir welds under variable loadings, *Int. J. Fatigue*, vol. 37, pp. 8–16, 2012.

[72] H. M. Rao, W. Yuan, and H. Badarinarayan, Effect of process parameters on mechanical properties of friction stir spot welded magnesium to aluminum alloys, *Mater. Des.*, vol.

66, pp. 235–245, 2015.

[73] S. Hoseinlaghab, S. S. Mirjavadi, N. Sadeghian, I. Jalili, M. Azarbarmas, and M. K. Besharati Givi, Influences of welding parameters on the quality and creep properties of friction stir welded polyethylene plates,*Mater. Des.*, vol. 67, pp. 369–378, 2015.

[74] Y.-C. Lin, J.-J. Liu, B.-Y. Lin, C.-M. Lin, and H.-L. Tsai, Effects of process parameters on strength of Mg alloy AZ61 friction stir spot welds, *Mater. Des.*, vol. 35, pp. 350–357, 2012.

[75] Z. Zhang, X. Yang, J. Zhang, G. Zhou, X. Xu, and B. Zou, Effect of welding parameters on microstructure and mechanical properties of friction stir spot welded 5052 aluminum alloy, *Mater. Des.*, vol. 32, no. 8–9, pp. 4461–4470, 2011.

[76] W. Yuan, R. S. Mishra, S. Webb, Y. L. Chen, B. Carlson, D. R. Herling, and G. J. Grant, Effect of tool design and process parameters on properties of Al alloy 6016 friction stir spot welds, *J. Mater. Process. Technol.*, vol. 211, no. 6, pp. 972–977, 2011.

[77] M. K. Bilici and A. I. Yukler, Effects of welding parameters on friction stir spot welding of high density polyethylene sheets, *Mater. Des.*, vol. 33, pp. 545–550, 2012.

[78] K. Kumari, S. K. Pal, and S. B. Singh, Friction stir welding by using counter-rotating twin tool, *J. Mater. Process. Technol.*, vol. 215, pp. 132–141, 2015.

[79] A. Macwan, V. K. Patel, X. Q. Jiang, C. Li, S. D. Bhole, and D. L. Chen, Ultrasonic spot welding of Al/Mg/Al tri-layered clad sheets, *Mater. Des.*, vol. 62, pp. 344–351, 2014.

[80] H. Fujii, Y. G. Kim, T. Tsumura, T. Komazaki, and K. Nakata, Estimation of material flow in stir zone during friction stir welding by distribution measurement of Si particles, *Mater. Trans.*, vol. 47, no. 1, pp. 224–232, 2006.

[81] F. Simões and D. M. Rodrigues, Material flow and thermo-mechanical conditions during Friction Stir Welding of polymers: Literature review, experimental results and empirical

analysis, *Mater. Des.*, vol. 59, pp. 344–351, 2014.

[82] M. D. Tier, T. S. Rosendo, J. F. Dos Santos, N. Huber, J. a. Mazzaferro, C. P. Mazzaferro, and T. R. Strohaecker, The influence of refill FSSW parameters on the microstructure and shear strength of 5042 aluminium welds, *J. Mater. Process. Technol.*, vol. 213, no. 6, pp. 997–1005, 2013.

[83] S. Rajakumar, C. Muralidharan, and V. Balasubramanian, Influence of friction stir welding process and tool parameters on strength properties of AA7075-T6 aluminium alloy joints, *Mater. Des.*, vol. 32, no. 2, pp. 535–549, 2011.

[84] R. Nandan, G. G. Roy, T. J. Lienert, and T. Debroy, Three-dimensional heat and material flow during friction stir welding of mild steel, *Acta Mater.*, vol. 55, no. 3, pp. 883–895, 2007.

[85] P. Su, a. Gerlich, T. H. North, and G. J. Bendzsak, Material flow during friction stir spot welding, *Sci. Technol. Weld. Join.*, vol. 11, no. 1, pp. 61–71, 2006.

[86] K. N. Krishnan, On the formation of onion rings in friction stir welds, *Mater. Sci. Eng. A*, vol. 327, no. 2, pp. 246–251, 2002.

[87] Y. C. Chen, A. Gholinia, and P. B. Prangnell, Interface structure and bonding in abrasion circle friction stir spot welding: A novel approach for rapid welding aluminium alloy to steel automotive sheet, *Mater. Chem. Phys.*, vol. 134, no. 1, pp. 459–463, 2012.

[88] A. Suri, An Improved FSW Tool for Joining Commercial Aluminum Plates, *Procedia Mater. Sci.*, vol. 6, pp. 1857–1864, 2014.

[89] H. Lombard, D. G. Hattingh, A. Steuwer, and M. N. James, Optimising FSW process parameters to minimise defects and maximise fatigue life in 5083-H321 aluminium alloy, *Eng. Fract. Mech.*, vol. 75, no. 3–4, pp. 341–354, 2008.

[90] N. Nadammal, S. V. Kailas, and S. Suwas, A bottom-up approach for optimization of

friction stir processing parameters; a study on aluminium 2024-T3 alloy, *Mater. Des.*, vol. 65, pp. 127–138, 2015.

[91] J.-Q. Su, T. Nelson, R. Mishra, and M. Mahoney, Microstructural investigation of friction stir welded 7050-T651 aluminium, *Acta Mater.*, vol. 51, no. 3, pp. 713–729, 2003.

[92] Y. G. Kim, H. Fujii, T. Tsumura, T. Komazaki, and K. Nakata, Effect of welding parameters on microstructure in the stir zone of FSW joints of aluminum die casting alloy, *Mater. Lett.*, vol. 60, no. 29–30, pp. 3830–3837, 2006.

[93] P. Carlone and G. S. Palazzo, Characterization of TIG and FSW weldings in cast ZE41A magnesium alloy, *J. Mater. Process. Technol.*, vol. 215, pp. 87–94, 2015.

[94] S. Lu, D. L. Yang, S. Y. Xiao, and S. J. Chen, Three-dimensional investigation on temperature distribution and mechanical properties of AZ31 Mg alloy joint welded by FSW, in *Proceedings of the 1st International Joint Symposium on Joining and Welding*, pp. 67–72, 2013.

[95] G. Padmanaban and V. Balasubramanian, Selection of FSW tool pin profile, shoulder diameter and material for joining AZ31B magnesium alloy-An experimental approach, *Mater. Des.*, vol. 30, no. 7, pp. 2647–2656, 2009.

[96] C. Meran and V. Kovan, Microstructures and mechanical properties of friction stir welded dissimilar copper/brass joints, *Materwiss. Werksttech.*, vol. 39, no. 8, pp. 521–530, 2008.

[97] Y. F. Sun, J. M. Shen, Y. Morisada, and H. Fujii, Spot friction stir welding of low carbon steel plates preheated by high frequency induction, *Mater. Des.*, vol. 54, pp. 450–457, 2014.

[98] M. Jafarzadegan, A. Abdollah-zadeh, A. H. Feng, T. Saeid, J. Shen, and H. Assadi, Microstructure and Mechanical Properties of a Dissimilar Friction Stir Weld between Austenitic Stainless Steel and Low Carbon Steel, *J. Mater. Sci. Technol.*, vol. 29, no. 4, pp.

367–372, 2013.

[99] S. A. Khodir, Y. Morisada, R. Ueji, and H. Fujii, Microstructures and mechanical properties evolution during friction stir welding of SK4 high carbon steel alloy, *Mater. Sci. Eng. A*, vol. 558, pp. 572–578, 2012.

[100] P. Xue, B. L. Xiao, W. G. Wang, Q. Zhang, D. Wang, Q. Z. Wang, and Z. Y. Ma, Achieving ultrafine dual-phase structure with superior mechanical property in friction stir processed plain low carbon steel, *Mater. Sci. Eng. A*, vol. 575, pp. 30–34, 2013.

[101] T. Miura, R. Ueji, and H. Fujii, Enhanced tensile properties of Fe–Ni–C steel resulting from stabilization of austenite by friction stir welding, *J. Mater. Process. Technol.*, vol. 216, pp. 216–222, 2015.

[102] J. Jeon, S. Mironov, Y. S. Sato, H. Kokawa, S. H. C. Park, and S. Hirano, Friction stir spot welding of single-crystal austenitic stainless steel, *Acta Mater.*, vol. 59, no. 20, pp. 7439–7449, 2011.

[103] K. Ishida, Y. Gao, K. Nagatsuka, M. Takahashi, and K. Nakata, Microstructures and mechanical properties of friction stir welded lap joints of commercially pure titanium and 304 stainless steel, *J. Alloys Compd.*, vol. 630, pp. 172–177, 2015.

[104] D. Wang, D. R. Ni, B. L. Xiao, Z. Y. Ma, W. Wang, and K. Yang, Microstructural evolution and mechanical properties of friction stir welded joint of Fe–Cr–Mn–Mo–N austenite stainless steel, *Mater. Des.*, vol. 64, pp. 355–359, 2014.

[105] J. Han, H. Li, Z. Zhu, F. Barbaro, L. Jiang, H. Xu, and L. Ma, Microstructure and mechanical properties of friction stir welded 18Cr–2Mo ferritic stainless steel thick plate, *Mater. Des.*, vol. 63, pp. 238–246, 2014.

[106] M. Hajian, A. Abdollah-zadeh, S. S. Rezaei-Nejad, H. Assadi, S. M. M. Hadavi, K. Chung, and M. Shokouhimehr, Microstructure and mechanical properties of friction stir

processed AISI 316L stainless steel, *Mater. Des.*, vol. 67, pp. 82–94, 2015.

[107] P. Xue, H. Zhao, Y. Komizo, and Z. Y. Ma, Microstructure and mechanical properties of friction stir welded X80 pipeline steel joint under additional cooling, in *Proceedings of the 1st International Joint Symposium on Joining and Welding*, pp. 445–448, 2013.

[108] R. S. Coelho, A. Kostka, J. F. dos Santos, and A. Kaysser-Pyzalla, Friction-stir dissimilar welding of aluminium alloy to high strength steels: Mechanical properties and their relation to microstructure, *Mater. Sci. Eng. A*, vol. 556, pp. 175–183, 2012.

[109] H. Fujii, L. Cui, N. Tsuji, M. Maeda, K. Nakata, and K. Nogi, Friction stir welding of carbon steels, *Mater. Sci. Eng. A*, vol. 429, no. 1–2, pp. 50–57, 2006.

[110] C. Y. Dong, F. Hidetoshi, N. Kazuhiro, and N. Kiyoshi, Friction stir welding of high carbon tool steel (SK85) below eutectoid temperature, *Trans. JWRI*, vol. 38, no. 1, pp. 37–41, 2009.

[111] D.-H. Choi, C.-Y. Lee, B.-W. Ahn, J.-H. Choi, Y.-M. Yeon, K. Song, S.-G. Hong, W.-B. Lee, K.-B. Kang, and S.-B. Jung, Hybrid Friction Stir Welding of High-carbon Steel, *J. Mater. Sci. Technol.*, vol. 27, no. 2, pp. 127–130, 2011.

[112] H.-H. Cho, S. H. Kang, S.-H. Kim, K. H. Oh, H. J. Kim, W.-S. Chang, and H. N. Han, Microstructural evolution in friction stir welding of high-strength linepipe steel, *Mater. Des.*, vol. 34, pp. 258–267, 2012.

[113] M. Ghosh, K. Kumar, and R. S. Mishra, Friction stir lap welded advanced high strength steels: Microstructure and mechanical properties, *Mater. Sci. Eng. A*, vol. 528, no. 28, pp. 8111–8119, 2011.

[114] H. Aydin and T. W. Nelson, Microstructure and mechanical properties of hard zone in friction stir welded X80 pipeline steel relative to different heat input, *Mater. Sci. Eng. A*, vol. 586, pp. 313–322, 2013.

[115] M. Matsushita, Y. Kitani, R. Ikeda, K. Oi, and H. Fujii, Development of friction stir welding of high strength steel sheet, in *Proceedings of the 1st International Joint Symposium on Joining and Welding*, pp. 87–93, 2013.

[116] P. Asadi, G. Faraji, and M. K. Besharati, Producing of AZ91/SiC composite by friction stir processing (FSP), *Int. J. Adv. Manuf. Technol.*, vol. 51, no. 1–4, pp. 247–260, 2010.

[117] A. A. Zadpoor, J. Sinke, and R. Benedictus, Global and local mechanical properties and microstructure of friction stir welds with dissimilar materials and/or thicknesses, *Metall. Mater. Trans. A*, vol. 41, no. 13, pp. 3365–3378, 2010.

[118] A. Barcellona, G. Buffa, L. Fratini, and D. Palmeri, On microstructural phenomena occurring in friction stir welding of aluminium alloys, *J. Mater. Process. Technol.*, vol. 177, no. 1–3, pp. 340–343, 2006.

[119] D.-A. Wang and C.-H. Chen, Fatigue lives of friction stir spot welds in aluminum 6061-T6 sheets, *J. Mater. Process. Technol.*, vol. 209, pp. 367–375, 2009.

[120] S. Venukumar, S. Yalagi, and S. Muthukumaran, Comparison of microstructure and mechanical properties of conventional and refilled friction stir spot welds in AA 6061-T6 using filler plate, *Trans. Nonferrous Met. Soc. China*, vol. 23, no. 10, pp. 2833–2842, 2013.

[121] M. Peel, A. Steuwer, M. Preuss, and P. J. Withers, Microstructure, mechanical properties and residual stresses as a function of welding speed in aluminium AA5083 friction stir welds, *Acta Mater.*, vol. 51, no. 16, pp. 4791–4801, 2003.

[122] N. Pathak, K. Bandyopadhyay, M. Sarangi, and S. K. Panda, Microstructure and Mechanical Performance of Friction Stir Spot-Welded Aluminum-5754 Sheets, *J. Mater. Eng. Perform.*, vol. 22, no. 1, pp. 131–144, May 2012.

[123] L. Zhou, H. J. Liu, and Q. W. Liu, Effect of rotation speed on microstructure and

mechanical properties of Ti–6Al–4V friction stir welded joints, *Mater. Des.*, vol. 31, no. 5, pp. 2631–2636, 2010.

[124] A. L. Pilchak, D. M. Norfleet, M. C. Juhas, and J. C. Williams, Friction stir processing of investment-cast Ti-6Al-4V: Microstructure and properties, *Metall. Mater. Trans. A*, vol. 39, no. 7, pp. 1519–1524, 2007.

[125] G. M. Xie, Z. Y. Ma, Z. A. Luo, P. Xue, and G. D. Wang, Effect of Rotation Rate on Microstructures and Mechanical Properties of FSW Mg-Zn-Y-Zr Alloy Joints, *J. Mater. Sci. Technol.*, vol. 27, no. 12, pp. 1157–1164, 2011.

[126] G. Buffa, L. Fratini, and F. Micari, Mechanical and microstructural properties prediction by artificial neural networks in FSW processes of dual phase titanium alloys, *J. Manuf. Process.*, vol. 14, no. 3, pp. 289–296, 2012.

[127] I. Radisavljevic, A. Zivkovic, N. Radovic, and V. Grabulov, Influence of FSW parameters on formation quality and mechanical properties of Al 2024-T351 butt welded joints, *Trans. Nonferrous Met. Soc. China*, vol. 23, no. 12, pp. 3525–3539, 2013.

[128] M. Bahrami, M. Farahmand Nikoo, and M. K. Besharati Givi, Microstructural and mechanical behaviors of nano-SiC-reinforced AA7075-O FSW joints prepared through two passes, *Mater. Sci. Eng. A*, vol. 626, pp. 220–228, 2015.

[129] U. Suhuddin, L. Campanelli, M. Bissolatti, H. Wang, R. Verastegui, and J. F. dos Santos, A review on microstructural and mechanical properties of friction spot welds in Al-based similar and dissimilar joints, in *Proceedings of the 1st International Joint Symposium on Joining and Welding*, pp. 15–21, 2013.

[130] J. Shen, D. Min, and D. Wang, Effects of heating process on the microstructures and tensile properties of friction stir spot welded AZ31 magnesium alloy plates, *Mater. Des.*, vol. 32, no. 10, pp. 5033–5037, 2011.

[131] Z. Shen, X. Yang, Z. Zhang, L. Cui, and T. Li, Microstructure and failure mechanisms of refill friction stir spot welded 7075-T6 aluminum alloy joints, *Mater. Des.*, vol. 44, pp. 476–486, 2013.

[132] Z. Shen, X. Yang, Z. Zhang, L. Cui, and Y. Yin, Mechanical properties and failure mechanisms of friction stir spot welds of AA 6061-T4 sheets, *Mater. Des.*, vol. 49, pp. 181–191, 2013.

[133] A. K. Lakshminarayanan and V. Balasubramanian, An assessment of microstructure, hardness, tensile and impact strength of friction stir welded ferritic stainless steel joints, *Mater. Des.*, vol. 31, no. 10, pp. 4592–4600, 2010.

[134] L. P. Borrego, J. D. Costa, J. S. Jesus, A. R. Loureiro, and J. M. Ferreira, Fatigue life improvement by friction stir processing of 5083 aluminium alloy MIG butt welds, Theor. Appl. Fract. Mech., vol. 70, pp. 68–74, Apr. 2014.

[135] K.-T. Huang, T.-S. Lui, and L.-H. Chen, Effect of microstructural feature on the tensile properties and vibration fracture resistance of friction stirred 5083 Alloy, *J. Alloys Compd.*, vol. 509, no. 27, pp. 7466–7472, 2011.

[136] C. Vidal, V. Infante, and P. Vilaça, Characterisation of fatigue fracture surfaces of friction stir channelling specimens tested at different temperatures, *Eng. Fail. Anal.*, doi. 10.1016/j.engfailanal.2015.02.009, 2015.

[137] Z. Zhang, B. L. Xiao, and Z. Y. Ma, Hardness recovery mechanism in the heat-affected zone during long-term natural aging and its influence on the mechanical properties and fracture behavior of friction stir welded 2024Al–T351 joints, *Acta Mater.*, vol. 73, pp. 227–239, 2014.

[138] P. Edwards and M. Ramulu, Fatigue performance of Friction Stir Welded Ti–6Al–4V subjected to various post weld heat treatment temperatures, *Int. J. Fatigue*, vol. 75, pp.

19–27, 2015.

[139] M. Besel, Y. Besel, U. Alfaro Mercado, T. Kakiuchi, and Y. Uematsu, Fatigue behavior of friction stir welded Al–Mg–Sc alloy, *Int. J. Fatigue*, vol. 77, pp. 1–11, 2015.

[140] M. Kadlec, R. Růžek, and L. Nováková, Mechanical behaviour of AA 7475 friction stir welds with the kissing bond defect, *Int. J. Fatigue*, vol. 74, pp. 7–19, 2014.

[141] F. Cioffi, J. Ibáñez, R. Fernández, and G. González-Doncel, The effect of lateral off-set on the tensile strength and fracture of dissimilar friction stir welds, 2024Al alloy and 17%SiC/2124Al composite, *Mater. Des.*, vol. 65, pp. 438–446, 2015.

[142] G. Borino, L. Fratini, and F. Parrinello, Mode I failure modeling of friction stir welding joints, *Int. J. Adv. Manuf. Technol.*, vol. 41, no. 5–6, pp. 498–503, 2008.

[143] G. Bussu and P. Irving, The role of residual stress and heat affected zone properties on fatigue crack propagation in friction stir welded 2024-T351 aluminium joints, *Int. J. Fatigue*, vol. 25, no. 1, pp. 77–88, 2003.

[144] K. V Jata, K. K. Sankaran, and J. J. Ruschau, Friction-stir welding effects on microstructure and fatigue of aluminum alloy 7050-T7451, *Metall. Mater. Trans. A*, vol. 31A, pp. 2181–2192, 2000.

[145] A. M. S. Malafaia, M. T. Milan, M. F. Oliveira, and D. Spinelli, Evaluation of dynamic defect detection in FSSW welded joints under fatigue tests, *Procedia Eng.*, vol. 2, pp. 1823–1828, 2010.

[146] V.-X. Tran, J. Pan, and T. Pan, Effects of processing time on strengths and failure modes of dissimilar spot friction welds between aluminum 5754-O and 7075-T6 sheets, *J. Mater. Process. Technol.*, vol. 209, no. 8, pp. 3724–3739, 2009.

[147] V.-X. Tran, J. Pan, and T. Pan, Fatigue behavior of spot friction welds in lap-shear and cross-tension specimens of dissimilar aluminum sheets, *Int. J. Fatigue*, vol. 32, pp.

1022–1041, 2010.

[148] Y. Uematsu, K. Tokaji, Y. Tozaki, Y. Nakashima, and T. Shimizu, Fatigue behaviour of dissimilar friction stir spot welds between A6061-T6 and low carbon steel sheets welded by a scroll grooved tool without probe, *Fatigue Fract. Eng. Mater. Struct.*, vol. 34, no. 8, pp. 581–591, 2011.

[149] Y. Uematsu, K. Tokaji, Y. Tozaki, T. Kurita, and S. Murata, Effect of re-filling probe hole on tensile failure and fatigue behaviour of friction stir spot welded joints in Al–Mg–Si alloy, *Int. J. Fatigue*, vol. 30, no. 10–11, pp. 1956–1966, 2008.

[150] A. Palmgren, Die Lebensdauer von Kugellagern, *Vereinesdeutscher Ing.*, vol. 68, no. 14, pp. 339–341, 1924.

[151] B. F. Langer, Fatigue failure from stress cycles of varying amplitude, *J. Appl. Mech.*, vol. 59, pp. A160–A162, 1937.

[152] M. A. Miner, Cumulative damage in fatigue, *J. Appl. Mech.*, vol. 67, pp. A159–A164, 1945.

[153] L. F. Coffin, A study of the effect of cyclic thermal stresses on the ductile metal, *Trans. ASME*, vol. 76, pp. 931–950, 1954.

[154] S. M. Beden, S. Abdullah, and A. K. Ariffin, Fatigue life assessment of different steel-based shell materials under variable amplitude loading, *Eur. J.Sci. Res.*, vol. 29, no. 1, pp. 157–169, 2009.

[155] A. Fatemi and L. Yang, Cumulative fatigue damage and life prediction theories : a survey of the state of the art for homogeneous materials, *Int. J. Fatigue*, vol. 20, no. 1, pp. 9–34, 1998.

[156] K. Golos and F. Ellyin, Generalization of cumulative damage criterion to multilevel cyclic loading, *Theor. Appl. Fract. Mech.*, vol. 7, no. 3, pp. 169–176, 1987.

[157] R. Tanegashima, H. Akebono, M. Kato, and A. Sugeta, 3-Dimensional observation of the interior fracture mechanism and establishment of cumulative fatigue damage evaluation on spot welded joints using 590MPa-class steel, *Int. J. Fatigue*, vol. 51, pp. 121–131, 2013.

[158] Z. Xiulin and W. Rong, On the corrosion fatigue crack initiation model and expression of metallic notched elements, *Eng. Fract. Mech.*, vol. 57, no. 6, pp. 617–624, 1997.

[159] A. Savaidis, G. Savaidis, and C. Zhang, Elastic–plastic FE analysis of a notched cylinder under multiaxial nonproportional fatigue loading with variable amplitudes, *Comput. Struct.*, vol. 80, no. 25, pp. 1907–1918, 2002.

[160] P. Heuler and T. Seeger, A criterion for omission of variable amplitude loading histories, *Int. J. Fatigue*, vol. 8, no. 4, pp. 225–230, 1986.

[161] S. Stanzl, E. Tschegg, and H. Mayer, Lifetime measurements for random loading in the very high cycle fatigue range, *Int. J. Fatigue*, vol. 8, no. 4, pp. 195–200, 1986.

[162] L. C. Lim, Y. K. Tay, and H. S. Fong, Fatigue damage and crack nucleation mechanisms at intermediate strain amplitudes, *Acta Metall. Mater.*, vol. 38, no. 4, pp. 595–601, 1990.

[163] X. Yang, N. Li, Z. Jin, and T. Wang, A continuous low cycle fatigue damage model and its application in engineering materials, *Int. J. Fatigue*, vol. 19, no. 10, pp. 687–692, 1998.

[164] E. S. Palma and F. A. C. Vidal, Fatigue damage analysis on body shell of a passenger vehicle, *J. Mater. Eng. Perform.*, vol. 11, no. 4, pp. 450–460, 2002.

[165] Y. Murakami and K. Miller, What is fatigue damage? A view point from the observation of low cycle fatigue process, *Int. J. Fatigue*, vol. 27, no. 8, pp. 991–1005, 2005.

[166] L. Xue, A unified expression for low cycle fatigue and extremely low cycle fatigue and its implication for monotonic loading, *Int. J. Fatigue*, vol. 30, no. 10–11, pp. 1691–1698,

2008.

[167] Y. Shi and H. Guo, Fatigue performance and fatigue damage parameter estimation of spot welded joints of aluminium alloys 6111-T4 and 5754, *Fatigue Fract. Eng. Mater. Struct.*, vol. 36, no. 10, pp. 1081–1090, 2013.

[168] Y. F. Sun, H. Fujii, N. Takaki, and Y. Okitsu, Microstructure and mechanical properties of mild steel joints prepared by a flat friction stir spot welding technique, *Mater. Des.*, vol. 37, pp. 384–392, 2012.

[169] H. S. Park, T. Kimura, T. Murakami, Y. Nagano, K. Nakata, and M. Ushio, Microstructures and mechanical properties of friction stir welds of 60% Cu–40% Zn copper alloy, *Mater. Sci. Eng. A*, vol. 371, no. 1–2, pp. 160–169, 2004.

[170] E. Haibach, The allowable stresses under variable amplitude loading, in *Proceeding of the Conference on Fatigue of Welded Structures*, pp. 328–339, 1970.

[171] N. Takeda and T. Naruse, Accurate prediction of fatigue life under random loading, *J. Soc. Mater. Sci. Japan*, vol. 61, no. 10, pp. 853–859, 2012.

[172] B. Zuccarello and N. Adragna, A novel frequency domain method for predicting fatigue crack growth under wide band random loading, *Int. J. Fatigue*, vol. 29, no. 6, pp. 1065–1079, 2007.

[173] A. Niesłony, M. Růžička, J. Papuga, A. Hodr, M. Balda, and J. Svoboda, Fatigue life prediction for broad-band multiaxial loading with various PSD curve shapes, *Int. J. Fatigue*, vol. 44, pp. 74–88, 2012.

[174] W.-F. Wu and T.-H. Huang, Prediction of fatigue damage and fatigue life under random loading, *Int. J. Press. Vessel. Pip.*, vol. 53, no. 2, pp. 273–298, 1993.

[175] P. Colombi and K. Doliñski, Fatigue lifetime of welded joints under random loading: rainflow cycle vs. cycle sequence method, *Probabilistic Eng. Mech.*, vol. 16, no. 1, pp.

61–71, 2001.

[176] D. Benasciutti and R. Tovo, Spectral methods for lifetime prediction under wide-band stationary random processes, *Int. J. Fatigue*, vol. 27, no. 8, pp. 867–877, 2005.

[177] N.E. Dowling, Estimation and correlation of fatigue lives for random loading, *Int. J. Fatigue*, vol. 10, no. 3, pp. 179–185, 1988.

[178] A. Preumont, On the peak factor of stationary Gaussian process, *J. Sound Vib.*, vol. 100, pp. 15–34, 1985.

[179] B. M. Hillberry, Fatigue of 2024-T3 aluminum alloy due to broad- band and narrow-band random loading, Iowa State University, 1967.

[180] I. Rychlik, A new definition of the rainflow cycle counting method, Int. J. Fatigue, vol. 2, no. 2, pp. 119–121, 1987.

[181] M. Matsuishi, T. Endo, Fatigue of metals subjected to varying stress, Japan society of mechanical engineers, pp. 37–40, 1968.

[182] S. Jeelani and M. Musial, A study of cumulative fatigue damage in titanium 6AI-4V alloy, *Int. J. Fatigue*, vol. 1, no. 1, pp. 23–27, 1986.

[183] S. Zhu, H. Huang, Y. Liu, L. He, and Q. Liao, A practical method for determining the Corten–Dolan exponent and its application to fatigue life prediction, *Int. J. Turbo Jet-Engines*, vol. 29, pp. 79–87, 2012.

[184] S. S. Manson and G. R. Halford, Practical implementation of the double linear damage rule and damage curve approach for treating cumulative fatigue damage, *Int. J. Fract.*, vol. 17, no. 2, pp. 169–192, 1981.

[185] Y.-H. Kim, J.-H. Song, and J.-H. Park, An expert system for fatigue life prediction under variable loading, *Expert Syst. Appl.*, vol. 36, no. 3, pp. 4996–5008, 2009.

---

[186] A. Singh, Development and validation of an *S*-*N* based two phase bending fatigue life prediction model, *J. Mech. Des.*, vol. 125, no. 3, pp. 540–544, 2003.

ACKNOWLEDGEMENTS

This research has been performed at the laboratory of strength and fracture of materials, Department of Mechanical science and engineering, the Graduate School of Engineering, Hiroshima University, Higashi Hiroshima, Hiroshima JAPAN under the direction of Professor Atsushi Sugeta.

The author would like to express my deepest appreciation and gratitude to my supervisor, Professor Atsushi Sugeta, for his kind advice, continuous supporting, valuable suggestion and encouragement throughout the course of his work as well as critical reading of this thesis.

The author is profoundly grateful to Thailand Institute of Scientific and Technological Research (TISTR), Ministry of Science and Technology, Royal Thai Government for all the financially support during the author studying for master course at Osaka University and doctoral course at Hiroshima University. And, the author wishes to acknowledge all staff in Office of education affairs, Royal Thai Embassy, Tokyo, for their kind supports.

The author is sincerely acknowledges to Professor Hidetoshi Fujii and Associate Professor Yufeng Sun, Joining and welding research institute, Osaka University for their co-operative to prepared the specimens throughout the course of this study. This work would not have been accomplished without their supports.

ACKNOWLEDGEMENTS

The author would like to express my sincere thanks to Associate Professor Masahiko Kato, Assistant Professor Hiroyuki Akebono for their instructive and heartfelt advices throughout the course of this study. This work would not have been accomplished without his supports.

The author would like to express my thanks to my colleagues in the laboratory for their help, and thanks to all Thai students in Hiroshima University, Higashi Hiroshima campus, for their help and encouragement.

Finally, the author is deeply grateful to my parent, Mr. Bamrung-Mrs. Prayong JOY-A-KA, my family and my wife, Miss Mayuree JAISAI for their endless and warm support and encouragement.

LIST OF PUBLICATIONS, PROCEEDINGS AND INTERNATIONAL PRESENTATIONS

1. List of publications and proceedings

1. Sutep Joy-A-Ka, Yuki Ogawa, Atsushi Sugeta, Yufeng Sun and Hidetoshi Fujii, Fatigue Fracture Mechanism on Friction Stir Spot Welded Joints Using 300 MPa-Class Automobile Steel Sheets under Constant and Variable Force Amplitude, Procedia of Material Science, vol 3, pp. 537-543, 2014.
2. Sutep Joy-A-Ka, Yuki Ogawa, Hiroyuki Akebono, Masahiko Kato, Atsushi Sugeta, Yufeng Sun, and Hidetoshi Fujii, Fatigue Damage Evaluation of Friction Stir Spot Welded Cross-Tension Joints Under Repeated Two-Step Force Amplitudes, Journal of Materials Engineering and Performance, vol.24 no.24, pp. 2494-2502, 2015.
3. Sutep Joy-A-Ka, Tomoshi Hirano, Hiroyuki Akebono, Masahiko Kato and Atsushi Sugeta: Fatigue Properties and Crack Growth Behavior of Friction Stir Spot Welded 300 MPa-Class Automobile Steel Sheets, The proceeding of 9th International Conference on Fracture & Strength of Solids, Jeju Island, Korea, 2013.
4. Sutep Joy-A-Ka, Tomoshi Hirano, Hiroyuki Akebono, Masahiko Kato, Atsushi Sugeta Hidetoshi Fujii and Yufeng Sun: 3-Dimensional Observation of the Interior Fatigue Fracture Mechanism on Friction Stir Spot Welded Using 300 MPa-Class Automobile

Steel Sheets, The proceeding of the 1st International Joint Symposium on Joining and Welding, Osaka, Japan, Woodhead Publishing Limited, Cambridge, UK, pp.435-442, 2013.

5. Tomoshi Hirano, Sutep Joy-A-Ka, Hiroyuki Akebono, Masahiko Kato and Atsushi Sugeta, 3D Observation of Interior Fatigue Fracture Mechanism of the Friction Stir Spot Welding Joints in Cross Tension Type using 300 MPa-Class SPCC, The proceeding of 日本材料学会 第62期通常総会 学術講演会, Tokyo, Japan , pp. 115-116, 2013.
6. Yuki Ogawa, Tomoshi Hirano, Sutep Joy-A-Ka, Ryota Tanegashima, Hiroyuki Akebono, Masahiko Kato, Atsushi Sugeta, Yufeng Sun and Hidetoshi Fujii, Fatigue Characteristics under Constant and Variable Loading Conditions on Cross Tension Typed Friction Stir Spot Welded Joints using 300 MPa-Class SPCC, The proceeding of 27th Symposium on Reliability Engineering & the 16th Symposium on Fracture Mechanics, Kumamoto, Japan, pp. 294-299, 2013
7. Masato Ikeda, Sutep Joy-A-Ka, Hiroyuki. Akebono, Mashiko Kato, Atsushi Sugeta, Yufeng Sun and H. Fujii, Fatigue Characteristics under Constant and Variable Force Condition of 300 MPa Class Friction Stir Spot welded Cross Tension Joints, Proceeding of The 3rd Japan-China Joint Symposium on Fatigue of Engineering Materials and Structures. 32nd Symposium on Fatigue, Gifu, Japan, pp. 265-269, 2014.

2. List of international presentations

1. Sutep Joy-A-Ka, Tomoshi Hirano, Hiroyuki Akebono, Masahiko Kato and Atsushi Sugeta: Fatigue Properties and Crack Growth Behavior of Friction Stir Spot Welded 300 MPa-Class Automobile Steel Sheets, 9th International Conference on Fracture & Strength of Solids, Jeju Island, Korea, June 2013

2. Sutep Joy-A-Ka, Tomoshi Hirano, Hiroyuki Akebono, Masahiko Kato, Atsushi Sugeta, Hidetoshi Fujii and Yufeng Sun: 3-Dimensional Observation of the Interior Fatigue Fracture Mechanism on Friction Stir Spot Welded Using 300 MPa-Class Automobile Steel Sheets, 1st International Joint Symposium on Joining and Welding, Osaka, Japan, November 2013.
3. Sutep Joy-A-Ka, Yuki Ogawa, Atsushi Sugeta, Yufeng Sun, and Hidetoshi Fujii, Fatigue Damage Evaluation of Friction Stir Spot Welded Cross-Tension Joints Under Repeated Two-Step Force Amplitudes, 20th European Conference on Fracture, Fracture at all scales, Trondheim, Norway, July 2014